PARAMETRIC STUDY OF LOW-PRESSURE PREMIXED ETHYLENE/HYDROGEN/OXYGEN FLAME SYNTHESIS OF TITANIA NANOPARTICLES AND THEIR PHASES

By

HADI DHARMA HALIM

A thesis submitted to the

School of Graduate Studies

Rutgers, The State University of New Jersey

In partial fulfillment of the requirements

For the degree of Master of Science

Graduate Program in Mechanical and Aerospace Engineering

Written under the direction of

Professor Stephen D. Tse

And approved by

_____

_____

_____

New Brunswick, New Jersey

January 2018

ABSTRACT OF THE THESIS

PARAMETRIC STUDY OF LOW-PRESSURE PREMIXED ETHYLENE/HYDROGEN/OXYGEN FLAME SYNTHESIS OF TITANIA NANOPARTICLES AND THEIR PHASES

By HADI DHARMA HALIM

Thesis Director:

Professor Stephen D. Tse

Parametric study of operating conditions of low-pressure premixed flame (ethylene/hydrogen/oxygen) synthesis using titanium tetra-isopropoxide (TTIP) precursor is investigated, specifically examining as-synthesized nanopowder phase and properties. The Sandia SPIN code is used to simulate the synthesis flow field to guide and compare with experiments. Strategic dilution of inert gases is used to adjust the characteristic flame temperature. As-produced samples are thermally stable without any sign of phase change, as characterized using TGA and DSC, up to 500ºC. X-ray photoelectron spectroscopy (XPS) indicates Ti^{4+} valence and presence of carbon (13 – 30 atomic %), with absence of Ti^{3+}, Ti-C, and nitrogen. SEM and TEM confirm mixed micro- and nano-meter features. XRD and SAED divulge srilankite, rutile, and anatase phases produce under different experimental conditions.

Temperatures ranging from 1560K to 2650K, ambient pressures from 20 to 40 torr, and burner flow velocities from 150 to 300 cm/s are investigated, producing nanoparticles ranging from 3-10nm ± 3nm with mixed srilankite and rutile titania phases. Oxygen concentration effects are also studied from equivalence ratios of 1.08 to 0.37. Fuel-lean conditions produce anatase-rutile mixed nanopowders, while fuel-rich conditions yielded srilankite-rutile mixed nanopowders. By modifying the composition of the precursor (e.g. by adding ethylene), the phase of the product can be changed, likely because of carbon-doping stabilizing a specific phase.

Acknowledgment

This acknowledgement starts with many thanks to Professor Tse for his guidance and support at completing this thesis. Your intellectual and mental fortitude continue to inspire me. Special thanks to your patience for the past 10 years. This thesis would never been completed without your help. From the thesis inception to analysis tools used, those interactions had shaped this thesis to fruition. I appreciate Prof. Jaluria and Prof. Guo for being a part of this thesis committee, and appreciate their time in reviewing this works.

To my lab mates Prof. Jafar Al-Sharab, John Doyle, Dr. Bob Horvath, Dr. Zhizhong Dong, Dr. Gang Xiong, Dr. Hong Hua, and Ahmed Kamal; I thank you for all of your discussion and pointers at overcoming challenges that I faced in this thesis. To Prof. Kear, Prof. Emge, Prof. Cosandey, Prof. Uhrich, Prof. Birnie and Dr. Rangan; thank you for your diagnostic and material science expertise. Ashley Pennington, Jonathan Shi, Rachel A. Yang and Prof. Celik; I thank you for your flexibility and help at completing Ta200 and Tb100_N11 cases. Prof. Baruh, Dr. Sankha Banarjee, Dr. Udhay Sundar, and Dr. Vishu Vijayakumar; thank you for being kind souls to me during what feels like lonely journey. Anne Pera, Dr. Vukosi Marivate, Maxwell Hormilla, Roy Johnson, Barbara Sirman and Dean Bender; thank you very much for being guidepost that focused me to my next destination. To the undergraduate teams (Sameer Lalwani, Varum Sharma, Kartik Chopra, Jason Parmar, Liam Gilroy, Zachary Price, David Alejandro Benitez, Rahul Upadhay, Miilan Anand, Marc Perratore, Richard Schmitt, Samuel Hong, John Higgins, Jamie Mills, Nicholas Lobosco, Idin Jafari, Karan Purba, Paramjyot Bakshi, Sagar Patel and Zia Farooq); thank you for teaching me about operational excellence, planning for failure, importance of pursuing something in life, and about Mechanical

Engineering! Some time passed since this thesis was written, and I have lost contact with some people that have helped me. I am thankful to everybody, even though unmentioned here, that has helped me in completing this thesis.

I would also like to thanks Dr. Jokic for being a great doctor; your comments about that I should be in comma when I first become your patient will always be remembered. Thank you for reminding me that I have to keep pushing for the important thing in life. For fellow depressive and diabetic out there, don't give up. For my fellow co-workers, Hiren Patel, Ankit Rana, Joseph Dilauro, Pat Hafford, Tom Bukwich, Kevin O'Brien, Karan Jalundhwala, Gregory Grugnale, Joseph Hall, Michael Divincenzo, and Radu Oancea; thank you for being my accountability partner, especially Radu and Ankit.

To my family, Henny Salim and Nilawaty Salim; thank you for your help assimilating United States culture. To my Grandmother, thank you for raising me the way you did regardless of political and family circumstances. Dear my wife Sasha Halim, I don't know how this thesis can be completed without your helps and support. Despite all challenges that we faced in the past five years, thank you for always being there to support me regardless of the hurdle that was thrown at us.

Table of Contents

List of Figures

List of Tables

Preface

Much of the content in this thesis are verbatim from published or soon to be submitted papers with collaborators; and I have obtained permission from the co-authors to include them in this thesis. Also, other chapters have wording similar to or identical to that found in the paper and drafts referenced in this section.

References

1. Hadi Halim, Ashley M. Pennington, Jonathan Shi, Bernard H. Kear, Fuat E. Celik, Stephen D. Tse; Low Pressure Flame Synthesis of Carbon-Stabilized Srilankite Titania Nanoparticles; manuscript in preparation.

1 Introduction

The science of nanotechnology progressed with developments in quantum physics, spectroscopy, and electron microscope imaging technique. However, the utilization and application of such technology dates back to the Lycurgus cup or even the mythical Damascus blade.

It is possible to draw analogies of these old technologies to the current one. In the Lycurgus cup, the color change that was observed when one views the cup from a different angle stems from the difference between transmitted and reflected light. Recently Freestone discovered that this behavior arises from the usage of gold nanoparticles embedded in the cup[1]. Fascinating enough, the ancient Roman people already knew of the method to create nanoparticles and applied it in their daily life.

Another analogy is the mythical Damascus Blade. While no one can say for sure what exactly a Damascus Blade is, it is believed that the 300 B.C. Middle Eastern sword smith had a working understanding of the iron-carbon phase diagram and steel forging technique. Reibold pointed out that carbon nanotubes and cementite nanowires appear within the Damascus sword composition[2]. It is impressive considering the concept of thermodynamics first appeared in the 1600s. This concept eventually led to the awareness of the phase diagram. Modern scientists are using similar knowledge in attempts to create a high Young's modulus and fracture-resistant material through the understanding of phase diagrams and the manipulation of the composition of the nanostructure within the material of interest.

1.1 Titania usage

The focus of this study is the titanium-oxide system, specifically titanium dioxide (TiO_2). Also known as Titania, TiO_2 is a widely commercialized product commonly used as pigment. Industrially, the rutile phase with anatase in conjunction or as alternative is typically used. Titania can also be used as food colorant, and its micron and nanometer sized varieties are typically used for sunscreen. Scientists of the previous decades discovered that bulk titania behaves quite differently from its nanometer counterpart. This has led to the invention of the dye sensitized solar cell (DSSC) by Gratzel[3], as well as various photo-catalytic devices for titania. It has been reported to be able to decompose various dyes, which can be used to model organic-based pollutants[4]. Its photo-induced hydrophilic properties[5] have been utilized as a self-cleaning coating in various roof constructions such as those at the Cape Town, Durban and Nelson Mandela stadium[6].

Commonly recognized titania polymorphs that are photo-catalytically active are rutile and anatase. Various discrepancies on which phase (and/or combination of phases) has higher catalytic activity are present in the literature[7]. In fact, given the many of polymorphs available in titania, it is not surprising if the other Titania phases are also photo-catalytically active. Some scientists have started reporting on the photo-catalytically active brookite and srilankite[8,9] phases. Scientist and engineers are also interested in improving the visible absorption of titania. Scientists have demonstrated that by increasing the dopant quantity, it is possible to shift the absorption edge to the visible regime while retaining its photo-catalytic performance[10]. This forms the basis of various titania doping studies that are found in the literature[11].

With various emerging novel applications, and the market of its conventional bulk properties, titania has become a lucrative research area[12]. However, its unique properties also drive questions such as, which kind of titania (or mixture of) is the best for these various applications[8]? Have people explored the phase diagram, and have scientists figured out the various modifications that are possible within such a system? More importantly, how do such modifications alter the properties of the final product? These are the kind of questions that scientists are trying to answer currently. Before we begin to explore such options, it is beneficial to take a look at the Ti-O and Titania phase diagram, as published by Murray and Dachille [13,14].

1.2 Phases of Titania

Conventionally, the bulk Ti-O system follows the phase diagram delineated by Murray[13]. Various Magneli phases are found as the oxygen content is reduced in the Ti-O system. One can see that various Ti valences can exist and alter the chemical structure of Ti-O material. However, the titania material is usually stabilized with +4 valences.

Hanaor and Dachille have shown that if you start with anatase titania, and apply high pressure or high temperature, it will change phases[15]. One can deduce that rutile is the bulk-phase high-temperature, high-pressure stable phase. Anatase is a low-temperature, low-pressure metastable polymorph. On the other hand, srilankite is considered a high-pressure low-temperature metastable polymorph. One should keep in mind that the titania pressure-temperature phase diagram will look different depending on the starting material. The phase diagram that Hanaor and Dachille observed is what

scientists consider as a thermodynamically-stable phase diagram. However, often the question remains: during the synthesis process, which is often not thermodynamically stable, can one predict the phase that will nucleate in the system?

One fact that should not be forgotten is that the internal pressures of nanoparticles are relatively high. Following the classical Young – Laplace model for internal pressure as an inverse function of particle diameter, one can imagine that the internal pressure of nanoparticles must be higher than their bulk counterparts. How high are the internal pressures? Given the nanometer size nature of these particles, even the definition of surface tension, which is another important element in Young-Laplace model, starts to break down. Hawa performed molecular dynamic simulation on SiO_2 nanoparticles and showed that for 6nm particle size, their internal pressure is approximately 5kbar[16]. Ehrman also reported internal pressure of 2kbar for 10nm Titania[17]. Fitting this data into the Young Laplace model, one can calculate that the internal pressure of 6nm titania will be approximately 3.3kbar. Comparing this to the thermodynamic phase diagram, one can see that if the starting material is anatase, then a titania nanoparticle should stabilize as anatase under external low pressure and low temperature.

Rutile is believed to be the stable phase for titania [14]. However, it is important to take a closer look at the titania system. First, there are various metastable polymorphs of titania that exist in nature. Scientists have discovered various phases, such as anatase, brookite, srilankite, contunnite, baddeleyite , and holandite. [18-20]

1.3 Various names for Orthorombic, Pbcn (60) phase

Of interest to this study are the anatase, rutile, and srilankite metastable phases. In the literature, the Orthorombic, Pbcn (60) phase is often described as srilankite, columbite, TiO_2-II, TiO_2-PbO_2 alpha similar phases and TiO_2-Hp interchangeably. Srilankite and TiO_2-II have been referred to interchangeably[21,22], and the phase has also been called columbite[23,24].

The best way to resolve the issue is by comparing their space group and lattice parameters, as outlined in Tong Shu's paper[24]. after such an analysis, we can assert that ICDD PDF#97-001-5328 depicts the same crystal structure as columbite, srilankite, and TiO_2-II, despite the discrepancies in the literature.

1.3.1 Kinetic driven

Zhang and Gribb (Banfield's group) proposed that in the nanoparticles synthesis process, most of these phenomena are actually kinetically-driven instead of thermodynamically driven[25,26]. Banfield's group utilized the solution method by hydrolyzing titanium, inherently kinetically different from the gas phase method. Zhang noted the stabilities inversion of anatase and rutile phases for nanoparticles. Thus, even if the thermodynamically stable phase is rutile, anatase is the more commonly observed state. Zhang further hypothesized that particle sizes smaller than 11nm will most likely nucleate as anatase. In-between 11nm - 35nm is brookite, and finally larger than 35nm will be rutile. It is worth mentioning that Banfield's group did not report whether there were any other dopant in their samples.

Another example of kinetic driving force is compression or decompression history (hysteresis), which is dependent on the morphology of the titania nanosamples[23], which is in turn dependent on the initial oxygen concentration as precursor in plasma processes for both titania[27] and copper-oxide nanoparticles[28].

1.4 How it is typically synthesized?

Understanding that nanoparticle synthesis are not solely driven by thermodynamic aspect, unlike its bulk counterpart; it is important to recognize that depending on the method, one can obtain different phases of titania. Here are several synthesis methodologies that have been used to create Titania nanostructures.

1.4.1 Solid phase method - Pressure driven method

Investigating the effects of pressure on the titania phase has piqued scientists' interests[15]. With the advancement of analytical methods, there are ongoing interests to renew these studies and investigate the higher-pressure titania phases. Using pressure to transition from anatase, rutile, and brookite phases at ambient pressure to higher pressures, high-pressure phases, such as srilankite[29], can be examined. Another study investigated pressure-induced Nb-doped titania noting similar phase transition to the higher-pressure titania[23]. Although these methods can create nanometer sized features of high-pressure phase titania, in general they are not suitable for catalysis processes without further processing.

Another variant of the solid-phase method is ball milling. Several studies successfully synthesized srilankite phase[21,30,31]. Similar to the high-pressure method, this method induces partial sintering. Nevertheless, increases in photo-catalytic effects in the

visible wavelength are observed[31].

1.4.1.1 Liquid phase method

The liquid-based method aims to increase surface area by nucleating the titania particles using liquid precursor such as TTIP or $TiCl_4$. Various solution methods have produced ambient pressure phases such as brookite, rutile, and anatase. Primary control in this method lies in adding surfactant to avoid clustering. With the advancement of diagnostic methods and particle-size control, one may see the high-pressure phase being generated with this method in the future[32-35]. One challenge in this method is separating the nanoparticles from the liquid byproduct.

1.4.1.2 Gas Phase method

The gas-phase method aims at nucleating titania particles in the gas phase. The precursor is vaporized. This method uses more energy than other method; however does not suffer from other additional sintering or need for separation from byproduct. The methods includes plasma-driven method[27], plasma modification[36,37], chemical vapor deposition methods[38], flame spray pyrolysis[39], atmospheric flame[40], and low pressure method[41-44]. In this thesis, the low-pressure flame method, as described in Zhao Hong and Megan thesis[41,42], is employed.

In this thesis, carbon doping, accomplished through ethylene gas addition, and its effect on the generation of high-pressure-phase srilankite titania is investigated.

Parametric studies are conducted to isolate the primary mechanisms in the phase transition.

2 Experimental procedure

In this chapter, the experimental details are presented. The experimental setup is able to isolate ambient pressure, flame temperature, flame velocity, and precursor composition (e.g. oxygen concentration, ethylene concentration). Premix flame with stagnation point flow establishes the gas-phase synthesis geometry. The Sandia SPIN code is utilized to define the synthesis flow structure (i.e., temperature, species concentrations, flow velocities) for the experiments to aid in parametric study of the controlling mechanisms. Several techniques are employed to isolate one thermodynamic parameter, while fixing the others. Running these simulations help to establish the input parameters for the system.

2.1 Low-pressure premix flame in stagnation point flow

The procedure behind the flame synthesis method can be summarized in the following steps. First, a thermodynamically-stable premixed flame of fuel and oxidizer needs to be established. There are various parameters that can be controlled such as the pressure of the chamber, the composition of the fuel and oxidizer, and whether or not to add inert gasses to control the temperature profile of the flame. It is also possible to control the velocity of the flame by adjusting the type of inert to be used (denser inert such as nitrogen will slow down the overall velocity, while less dense inert such as helium will yield a faster flow velocity).

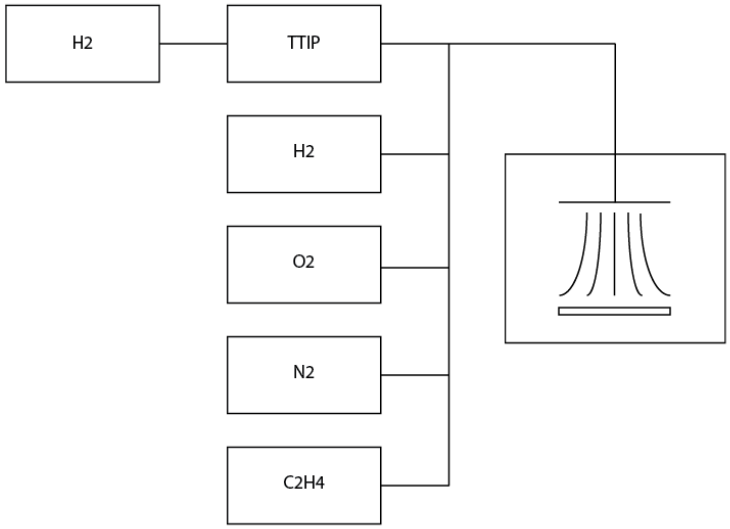

Figure 1. Simplified schematic of the low pressure, premix with stagnation point flow geometry flame synthesis process.

Once the flame condition is established, the next step is delivering the precursor. In this work, titanium tetraisopropoxide (TTIP) is utilized as the precursor for this flame. The precursor delivery technique that is used in this work is a bubbler based vapor delivery unit. The precursor is heated to a saturated vapor in the bubbler. The set point of this bubbler temperature is 85ºC, corresponding to a loading rate of 3.43 E^{-4} mol/min. Gases are then delivered through the bubbler to carry the precursor into the flame.

Finally, the precursor vapor encounters the flame, where it pyrolyzes/oxidizes. Homogeneous nucleation occurs in the presence of a steep temperature gradient. A relatively monodispersed particle distribution can be collected on the cold substrate. Details of the experimental setup and description of the bubbler setup are available from Megan's and Zhao Hong thesis [41,42].

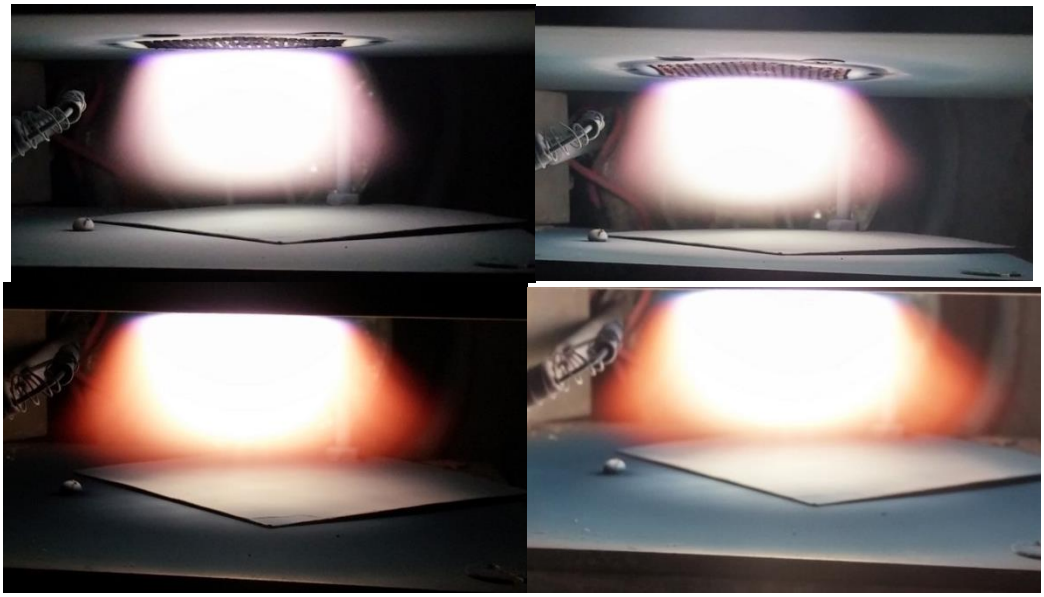

Figure 2 Pictures of Ti O2 9p5 (top- left low exposure, right – high exposure) and Ti O2 3p25 (bottom – left low exposure, right – high exposure)

2.2 Simulation

The flame structure can be modeled as a complex system. It encapsulates the fluid mechanics (stagnation flow geometry, Navier-Stokes Equation), heat transfer (Energy balance equation, heat release from the combustion reaction), and finally chemistry (kinetic rate of various collision and combustion species interaction). The Sandia Chemkin–Spin package can be used to model the flame structure, e.g., the temperature, species concentration, and velocity profiles of the flow field.

For the chemical reactions, GRI Mech 1.2 with modified C* reaction is used. This modification follows the proposed simulation by Megan and Zhao Hong [41,42].

2.3 Doping system

Depending on the type of fuel used, one can also control the dopant by adjusting either the combustible gas mixture, or the precursor composition. In this study, ethylene is utilized as a carbon dopant. An accompanying effect of adding such fuel is the increase in the temperature of the flame. It is important to be able to control the carbon dopant quantity, which can affect the crystallinity of the products. Here, the increase in temperature will be compensated by modifying the inert gas to lower back the temperature.

An additional mass flow controller is employed to deliver the ethylene. Special precaution needs to be taken to make sure that higher flow rate gas is introduced in the parallel part of the T junction, rather than the perpendicular section to prevent backflow.

2.4 Parametric Study design – Establishing input condition

Some of the interested input parameters are ambient pressure, temperature, velocity, and chemical composition. For ambient pressure, this is easily modified in the SPIN input parameters. Experimentally, this will be accomplished by controlling the valve between combustion chamber to the vacuum pump.

For temperature, the variable we choose to define this parameter is the highest temperature in the output of SPIN. Similarly, for velocity, we choose to define this parameter by the initial input velocity to the SPIN. The most common technique used to control temperature is by adjusting the inert gases. Experimentally these parameters are

driven by the SPIN code input chemical composition. SPIN code input can be translated to the appropriate mass flow rate to the mass flow controller.

2.4.1 Cases

2.4.1.1 Ta cases; Hydrogen only flame

The first case in this study (Ta150) uses hydrogen as base fuel. The hydrogen and oxygen flame have an equivalence ratio of 0.42, and 25% percent nitrogen is added as inert; this case is derived from the standard 20-torr condition from Megan and Zhao Hong studies[41,42]. This condition yields a maximum temperature flame of 1560K. The velocities of the gases are set at 150cm/s by using a mass flow controller. These are shown in Figure 3.

Ta200 will be discussed as a comparison case to the Tb case.

2.4.1.2 Tb cases; Hydrogen/Ethylene flame

The second set of cases consists of Tb100 to Tb300. In this set of cases, ethylene is added as the base carbon dopant. As mentioned earlier, the unintended effects of this fuel addition is the significant increase in the temperature. Hydrogen and ethylene are used as fuel in a 1:1 ratio. These fuels are then balanced stoichiometrically with oxygen (equivalence ratio of 1), and 47.6% of nitrogen added as inert. Finally, the velocities of the gases are varied from 100, 150, 200, 250, and 300 cm/s. These are shown in Figure 4.

2.4.1.2.1 Ta200 compare to Tb100_N11

Ta200 and Tb100_N11 are a special subset of the Ta and Tb series. The intent of this comparison is to make sure that the ambient pressure and maximum temperature are comparable. Ta is a hydrogen only flame, while Tb is a hydrogen/etheylene flame.

Ta200 is derived with the same equivalence ratio; however the velocity is increased to 200cm/s, keeping the pressure at 20 torr, with no inert. The goal of Ta200 is to increase the temperature of the hydrogen as high as possible, while maintaining the same temperature as Tb case, in this set: Tb100_N11. These are shown in Figure 5.

2.4.1.3 Tc; varying velocity

The third set of cases consists of T-c120 to T-c300. In this set, ethylene is added as the base carbon dopant. Hydrogen and ethylene are used as fuel in a 1:0.4 ratio. These fuels are balanced stoichiometrically with oxygen (equivalence ratio of 1). In these cases, the nitrogen concentration is adjusted such that the temperature of the flame is fixed at 2150K. The velocities of the gases range from 120, 160, 200, 240, 280, and 300 cm/s. The intention of the study is to understand the effect of flow velocity, with temperature constant. These conditions are shown in Figure 6.

2.4.1.4 Te; varying temperature

Te cases are conducted to explore the temperature effect. Starting from the Tb150 condition, nitrogen dilution is modified. By reducing the inert nitrogen concentration, the temperature is raised, with other parameters kept constant. These are shown in Figure 7.

2.4.1.5 Tg; varying ambient pressure

The Tg series is produced by starting from the Tb150 case, and then changing the pressure to 40 torr. The result is plotted below. These are shown in Figure 8.

2.4.1.6 Th; varying oxygen concentration – fuel lean

The Th series is produced by starting from Tb150, and then modifying the oxygen concentration. The nitrogen concentration is adjusted with the intent of keeping the temperature constant. The corresponding plots are shown in Figure 9.

2.4.1.7 Ti; varying oxygen concentration – fuel rich

Similar to Th, Ti is based on Tb150, with reduced oxygen concentration. The nitrogen concentration is adjusted to keep the maximum temperature the same. These are shown in Figure 10.

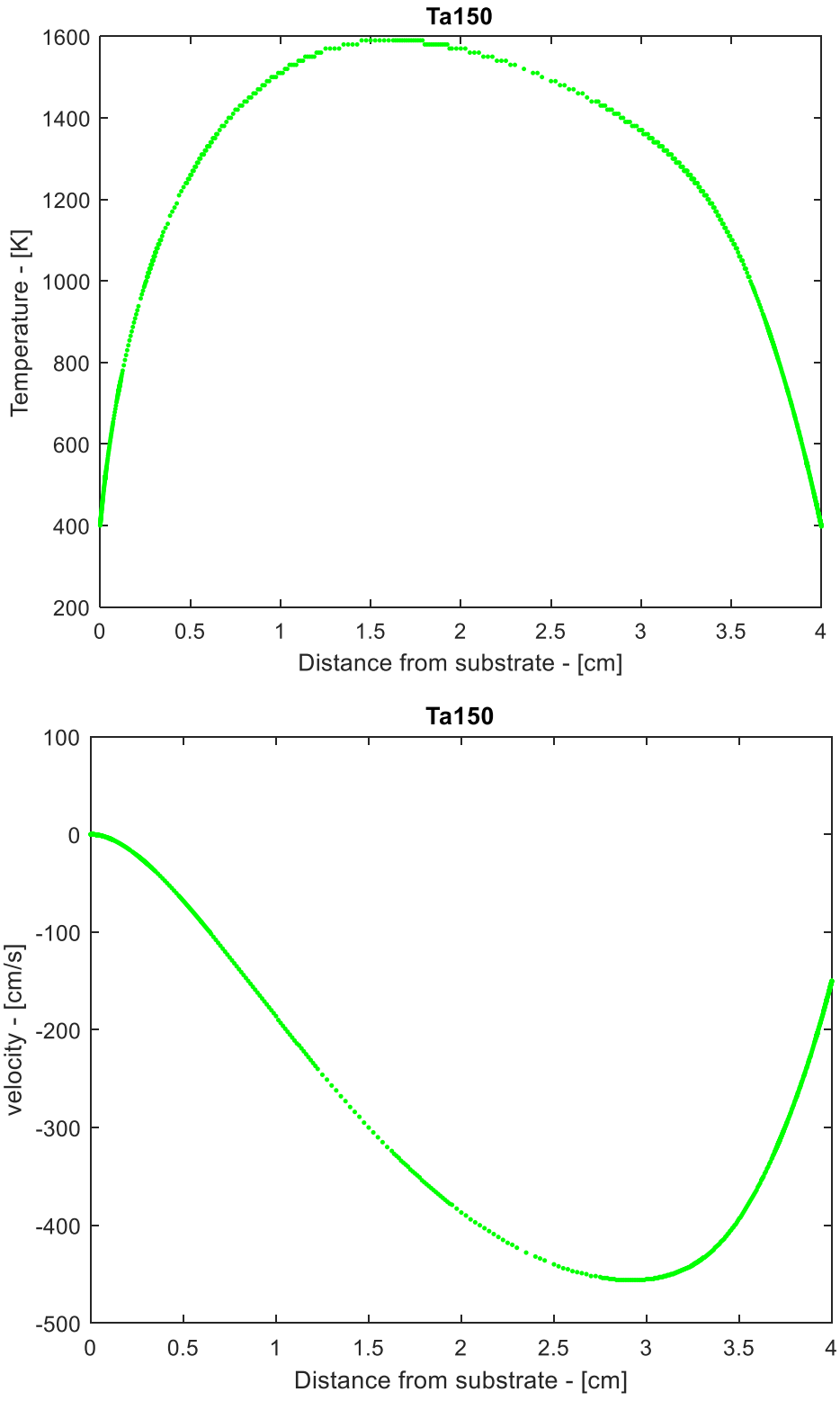

Figure 3. SPIN temperature and velocity output for standard 20 torr case. This case is renamed as Ta150 in this study to differentiate between Hydrogen/Oxygen and Ethylene/Hydrogen/Oxygen flame.

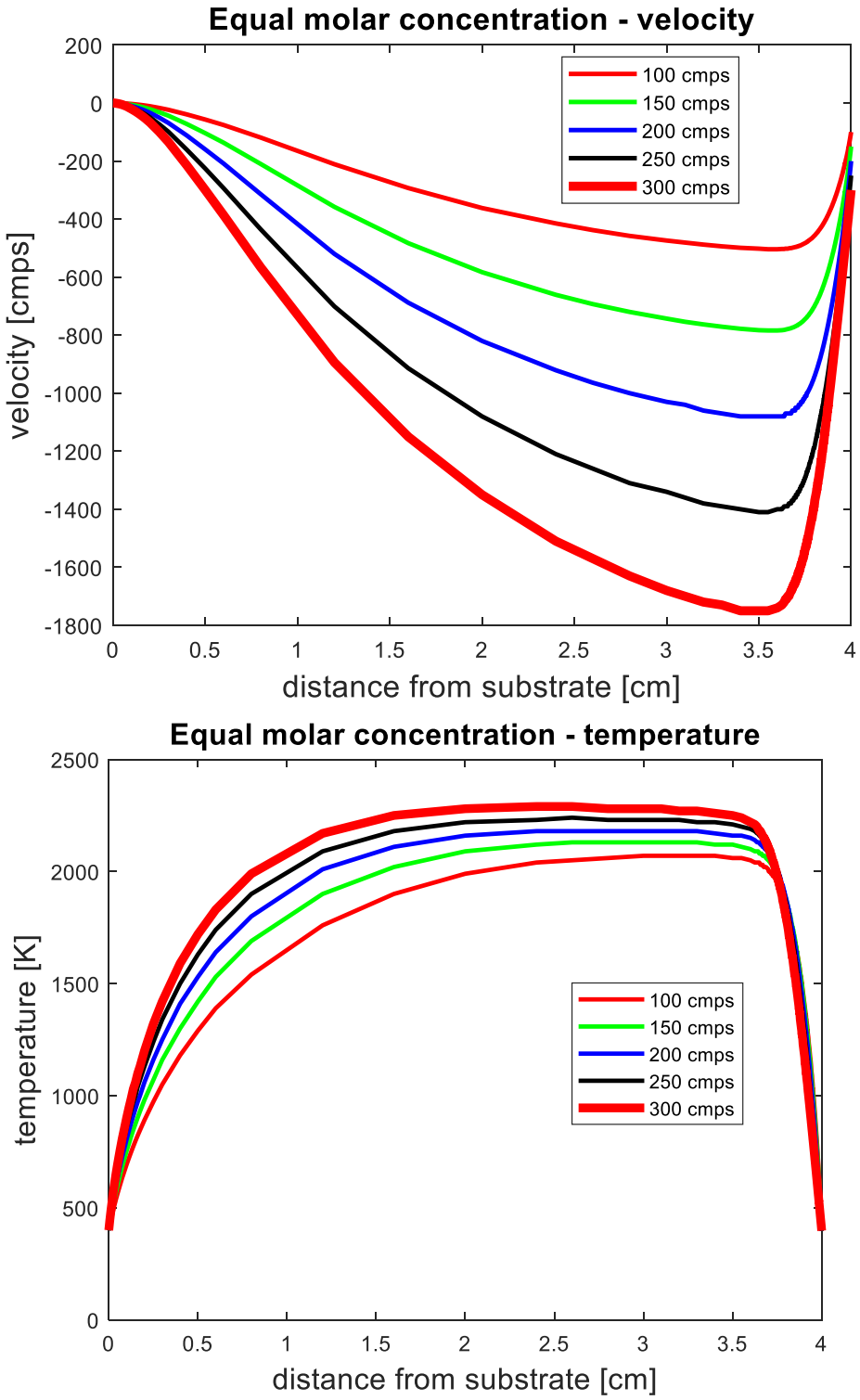

Figure 4. SPIN temperature and velocity output of Tb100, 150, 200, 250, 300.

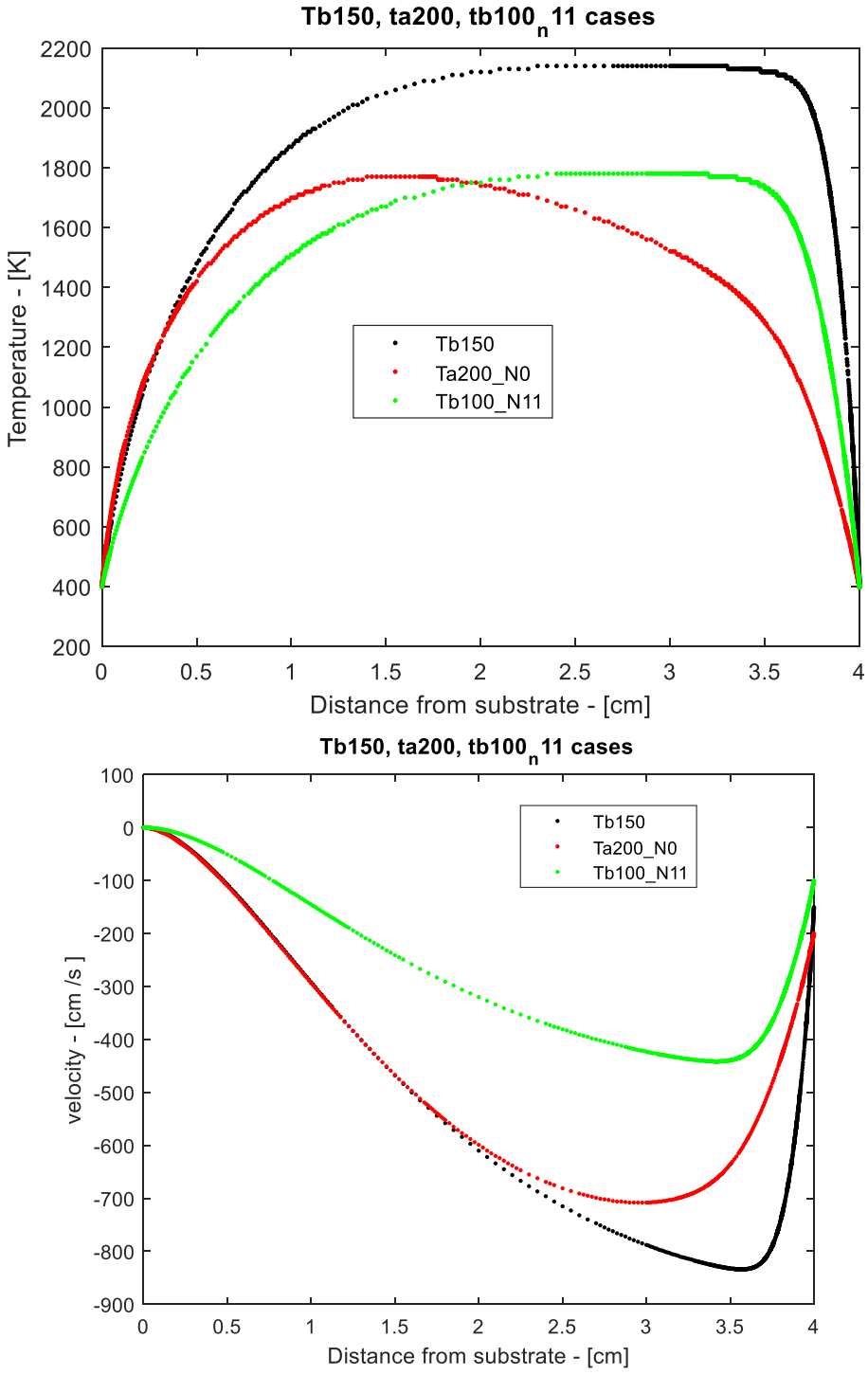

Figure 5. SPIN temperature and velocity ouput of Tb150, Tb100_N11 and Ta200. These simulated results show Tb100_N11 and Ta200 similar maximum temperature. Tb150 is plotted as a reference.

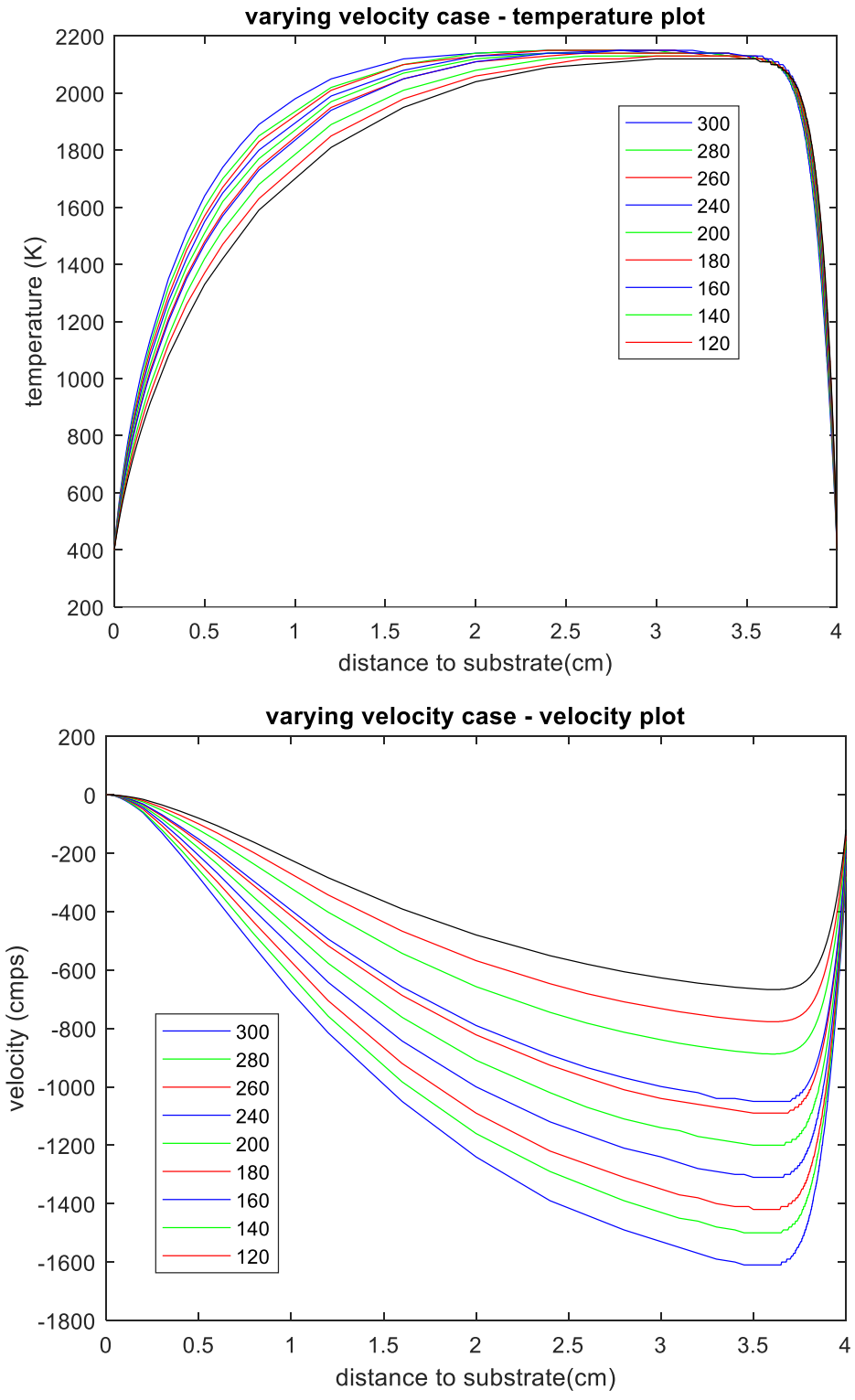

Figure 6 SPIN temperature and velocity output of Tc100, 120, 140, 160, 180, 200, 240, 260, 280, 300.

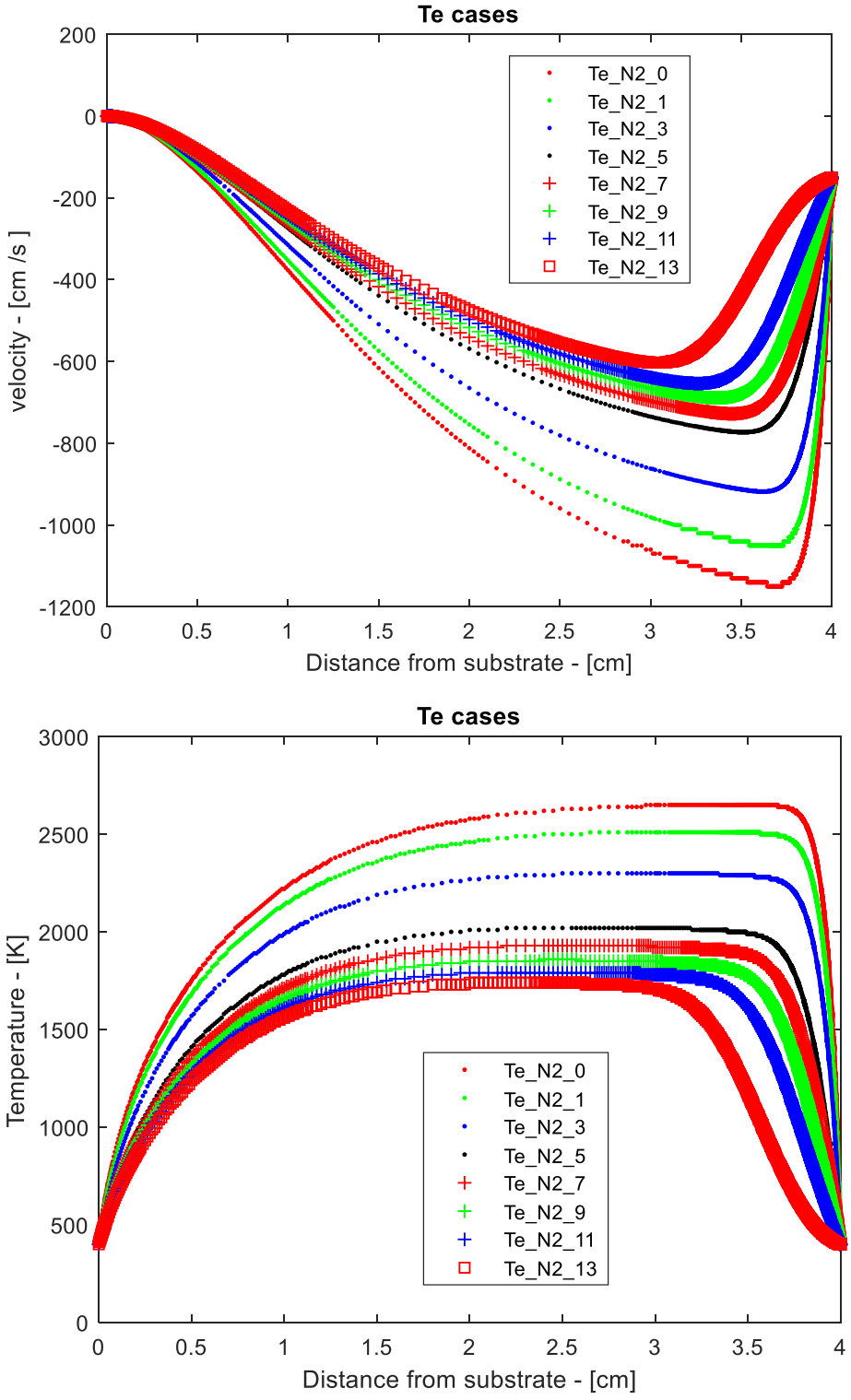

Figure 7 SPIN temperature and velocity output of Te_N2_0, 1, 3 , 5, 7, 9, 11, 13.

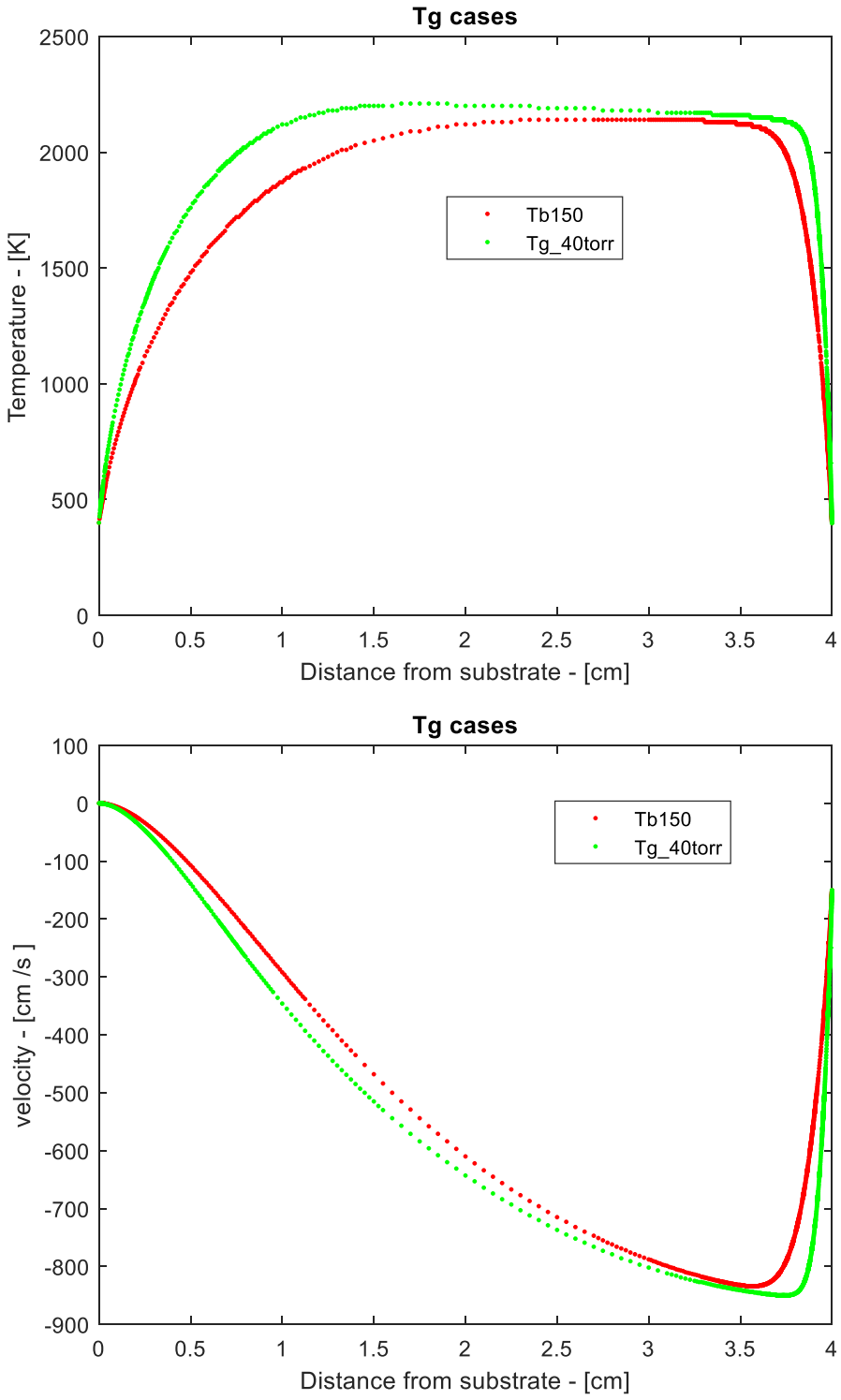

Figure 8 SPIN temperature and velocity output of Tg_40 torr compare to Tb150.

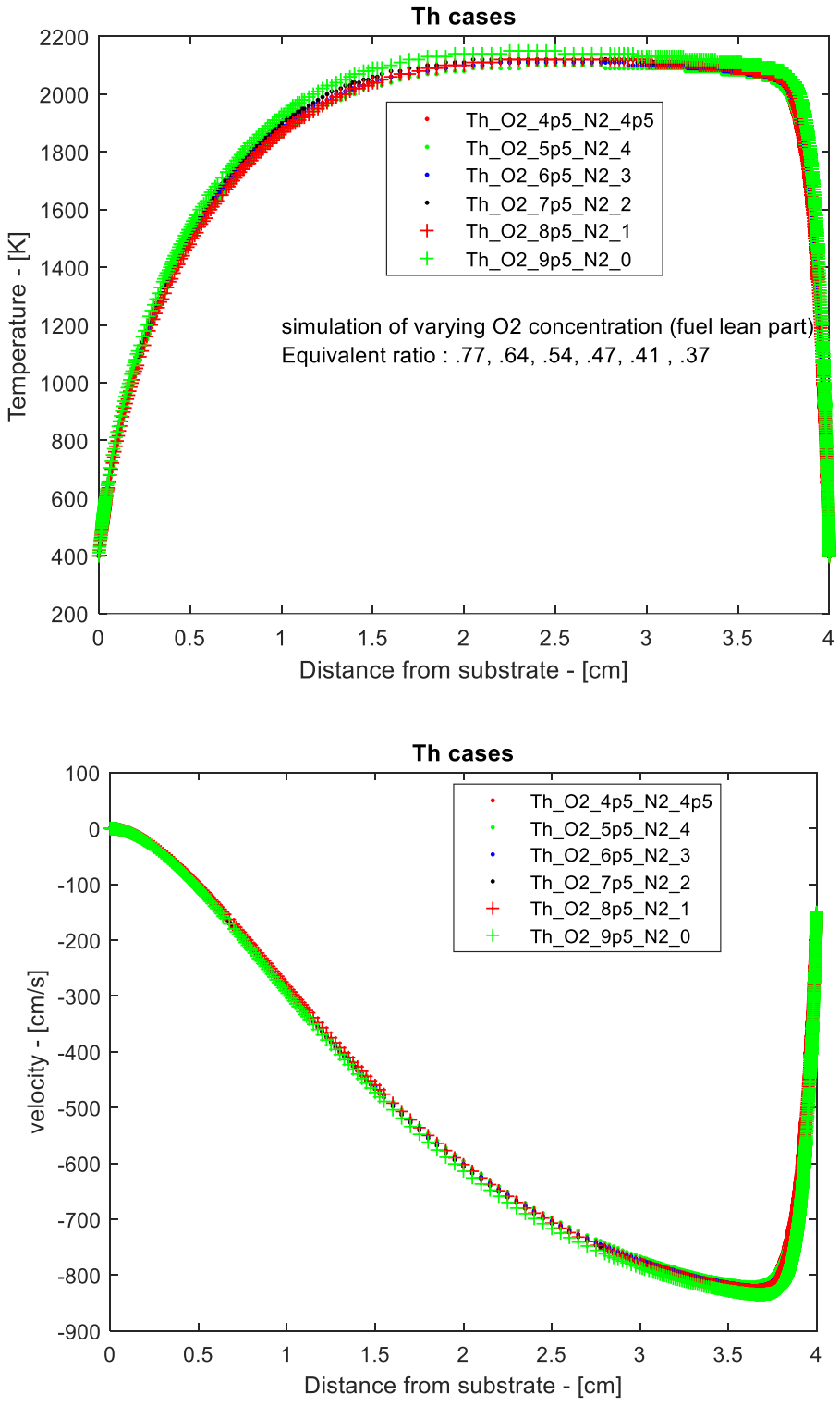

Figure 9 SPIN temperature and velocity output of Th_O2_4p5_N2_4p5, Th_O2_5p5_N2_4, Th_O2_6p5_N2_3, Th_O2_7p5_N2_2, Th_O2_8p5_N2_1, Th_O2_9p5_N2_0. Showing same temperature profile between the Th series.

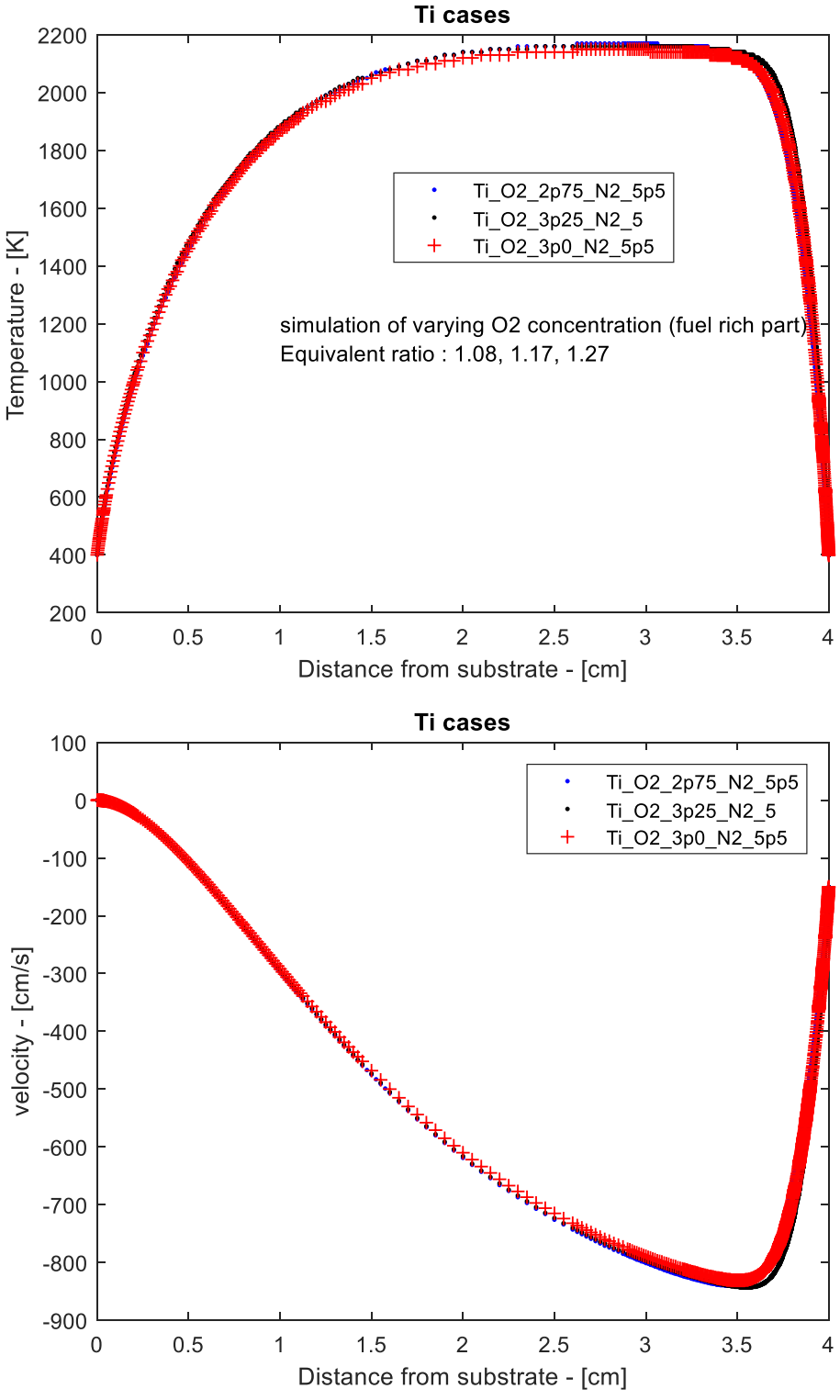

Figure 10 SPIN temperature and velocity output of Ti_O2_2p75_N2_5p5, Ti_O2_3p25_N2_5, Ti_O2_3p0_N2_5p5 showing same temperature profile between the Ti series.

2.5 Modifications to the experimental setup

Some modifications are made to the experimental setup to improve the repeatability of the experiments and to reduce operational errors:

1. Installed additional heating line to prevent vapor condensation.
2. Installed one-way valve to prevent upstream backflow (and liquid backflow).
3. Compartmentalized the pressure in different sections to make sure that pressure always flows downstream. This is especially helpful during ignition process.
4. Added baffle at precursor downstream tube.
5. Installed double LN2 trap to make sure that nanoparticle and vapor do not condense in the vacuum pump.
6. Implemented cleaning process using pressurized gas, and delivering of isopropanol into the system.
7. Added GFCI to the electrical circuit for troubleshooting and electrical safety.
8. Established maintenance schedule – igniter every 3 experiments, oil change every 10 experiments / months.

2.6 Collection Plate

The cover plate system is used to make sure that powder is collected only during the steady state condition. The collection plate is covered until the precursor is delivered, and steady state is reached. Then, the cover plate is knocked (thus the diamond shaped overlay). Powder is only collected within this diamond overlay. Note that there is the jet impinged area (center) and the remainder of the area within the diamond overlay. For this thesis, we analyze the center samples.

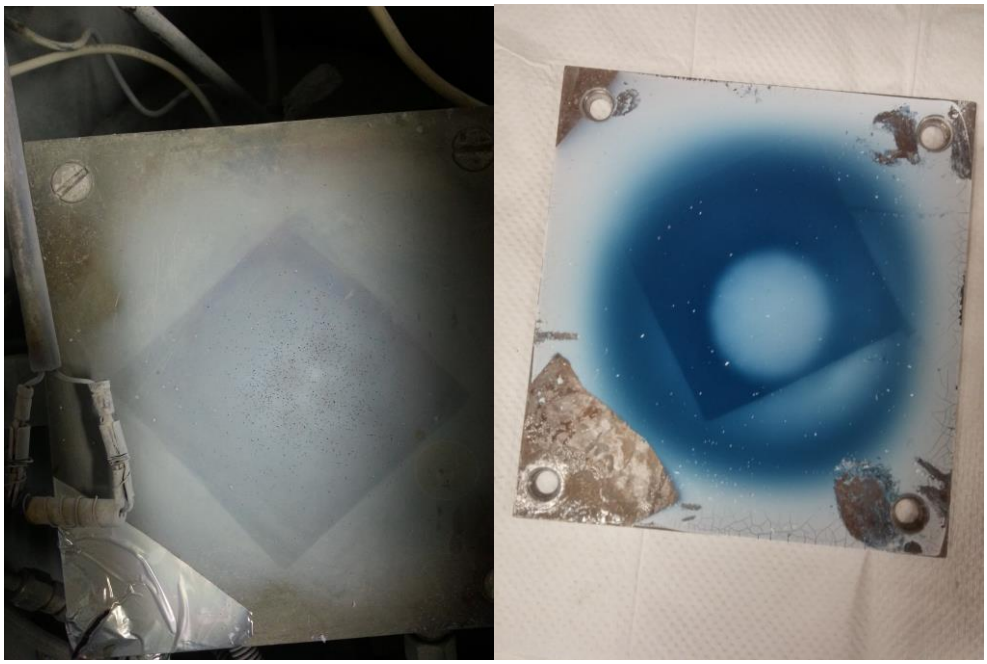

Figure 11 Collection plate of a typical TiO2 sample. Highlighting the separation between impingement area (Center), and rest of the area covered under cover plate

Figure 12 Collected powders indicating observed differences between the impinged area (bottom), and the rest of the covered plate. For this thesis, we focus on the center samples

3 Analysis tool used

Several analysis methods are used to analyze the nanopowders, including optical imaging, DSC, TGA, electron microscopy, and x-ray and electron diffraction.

3.1 Optical pictures

Physical appearances of the samples are collected using the built in camera from Samsung Galaxy Note 3 / LG G2 phone. For pictures of the flame, neutral-density filters with OD's of 0.4 and 1 are used to attenuate the intensity.

3.1.1 Tb150, Tb250, Ta150 – Investigating visible absorption and indication of dopant.

The industry standard for titania is Degussa P25, and they are normally white. This is also the color that is normally observed for the anatase samples synthesized in this study. The color starts shifting toward yellow (for rutile sample); and in general, shift toward blue for srilankite samples.This color change implies bandgap shift, exhibiting visible color absorption.

For example, Tb150 is light blue; and Tb250 is yellow. These colors are not commonly observed color for titania, which is white. From the chemical perspective, the color change corresponds to the absorption bandgap shift. For rutile, the bandgap is reported around 3eV. Anatase is typically observed to be approximately 3.3ev. To the best of the author's knowledge, the experimental bandgap measurement for pure srilankite is not available in the literature. This bandgap shift is also indicative of doping.

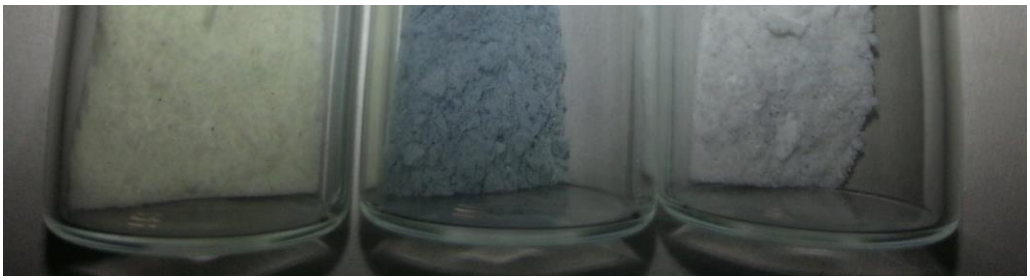

Figure 13 Optical image of Tb-250, Tb150 and Ta150 (left to right). Note not white appearance of Tb250 and Tb150, indicating visible color absorption and signs of doping.

3.2 Thermal stability

We are also interested in determining the stability of the phases that are created. In terms of temporal stability, the sample that has been kept for 1 year does not exhibit any visible color changes, nor phase changes under SAED. The analysis also indicates that the samples do not undergo phase changes up to 500ºC.

Two analysis tools that are used to evaluate thermal stability are digital scanning calorimetry (DSC) and thermal gravimetric analysis (TGA)[45].

3.2.1 DSC

Digital scanning calorimetry works by measuring the amount of heat added (or not added) to the samples while tracking its temperature. This will yield heat loss vs. temperature plot that can be used to analyze what type of heat signature exists. Another important aspect to note is that phase changes usually corresponds to a sharp change in the DSC spectra.

As references, DSC is run on two samples. One is DSC on Degussa P25, the industry standard titania. P25 has one endothermic peak around 100ºC, and another minor endothermic peak around 350ºC.

The second reference sample is alumina nanoparticles with TTIP drop added. Alumina is considered as thermally inert. From this experiment, the TTIP endothermic peak can be observed, noting undecomposed precursor thermal signature.

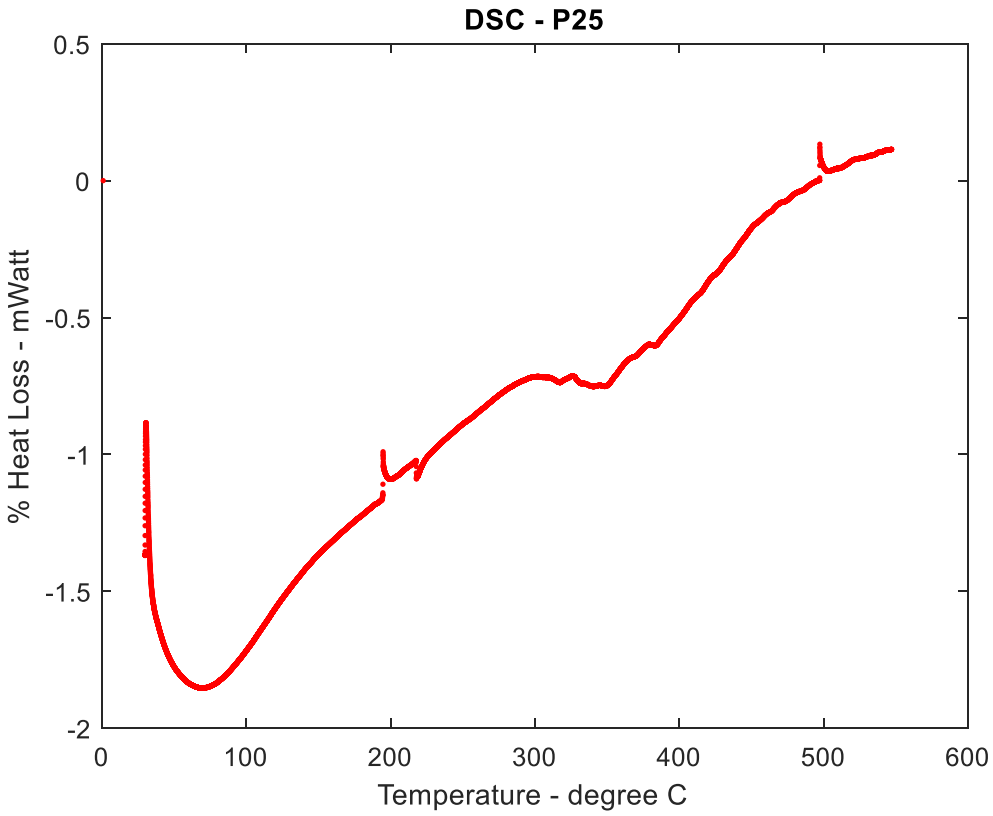

Figure 14 DSC of P25

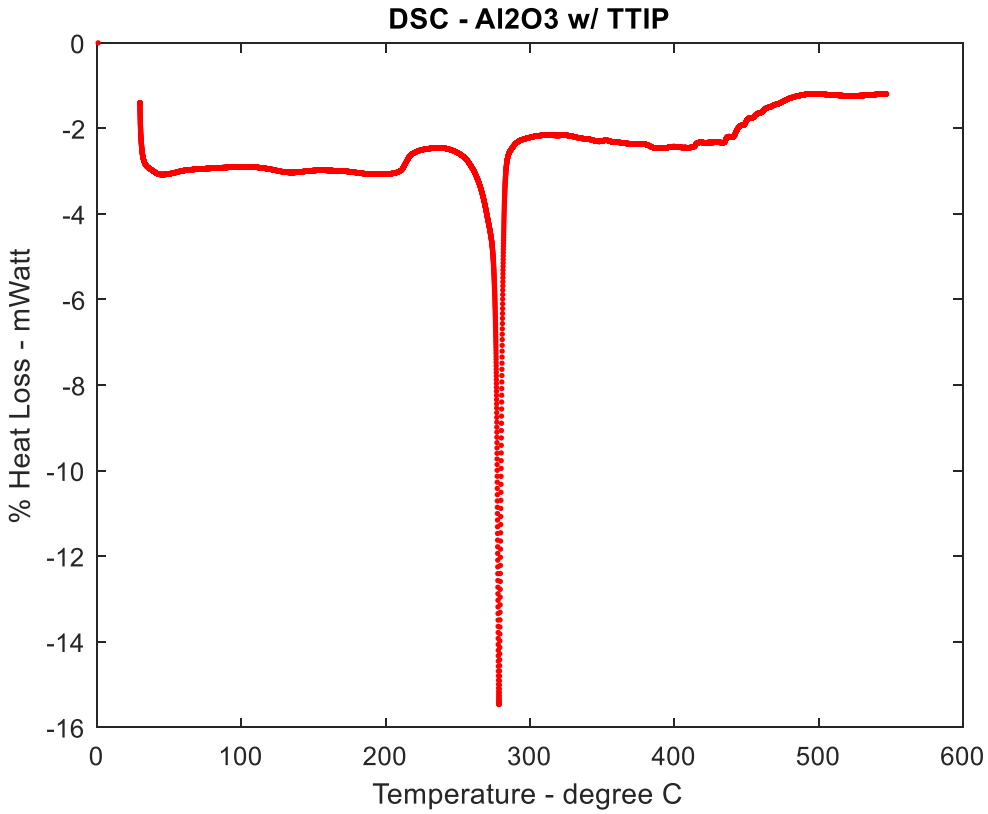

Figure 15 DSC Al2O3 with a drop of TTIP

Once a temperature signature of standard nanoparticle is established, samples are heated at 130ºC and 230ºC overnight at ambient air. Then these three samples are run under DSC. As-synthesized and 130ºC DSC powder show water adsorption around 100ºC, and undecomposed precursor at 250-270ºC. Post heating at 230ºC completely eliminates these endothermic peaks.

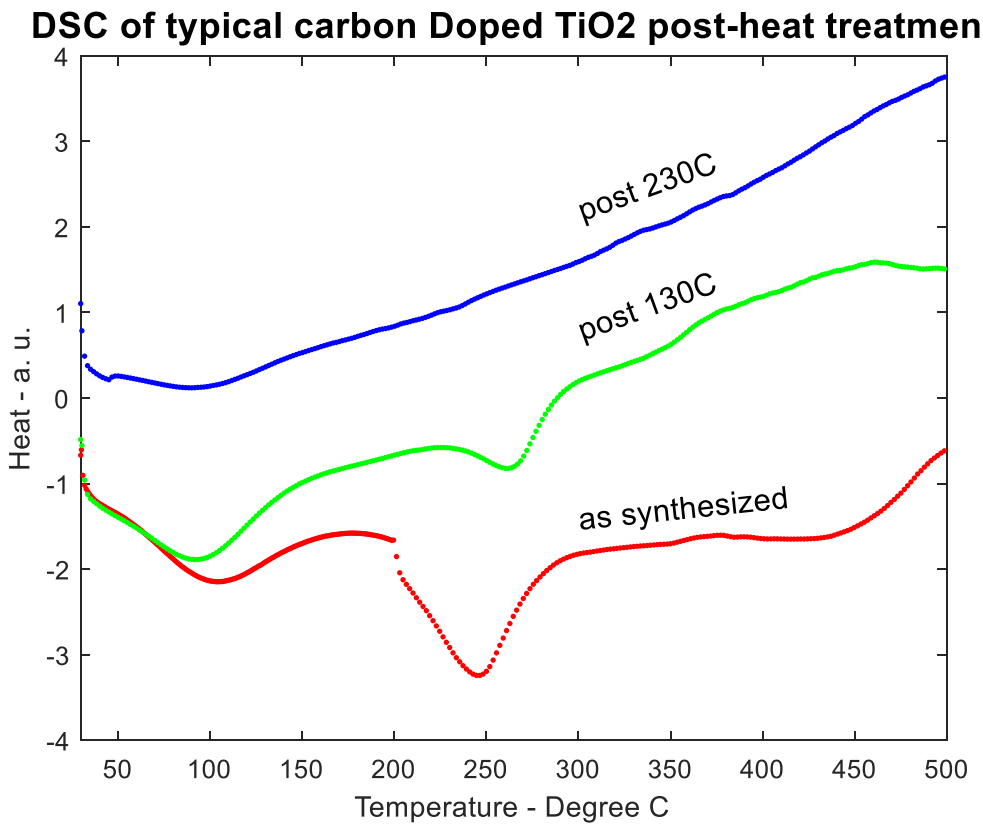

Figure 16 Typical DSC of carbon doped TiO2. We noted two heat loss peaks around 100 ^{0}C and 250 ^{0}C. After heating up to 230 ^{0}C, we no longer see any heat loss peak

The typical DSC curve can be observed for as-synthesized Ta150, Tb250, and Tb150, showing the same 100ºC and 250ºC endothermic peaks. From these spectra, up to 500ºC, phase changes are not observed.

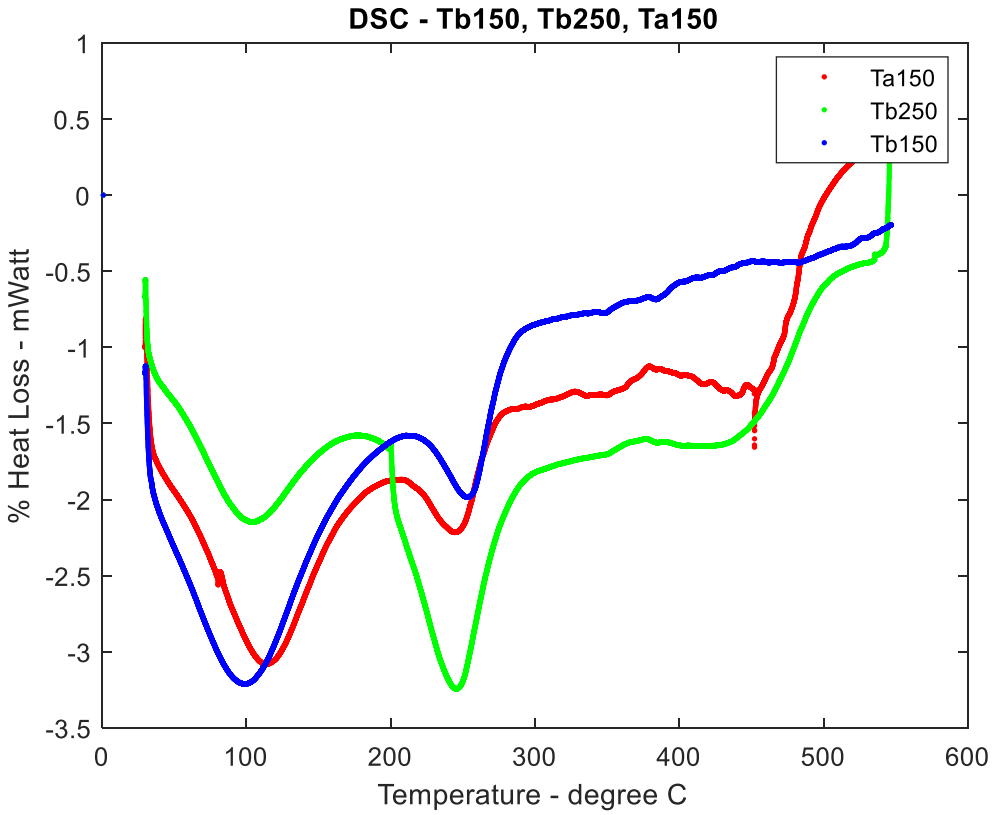

Figure 17 DSC of Ta150, Tb250, and Ta150

3.2.2 TGA

TGA works similarly to DSC, where the difference is instead of measuring caloric input, the weight (gravimetric) signature is tracked. TGA is useful when coupled with DSC. For example, sharp caloric signature change in DSC, when not accompanied with mass changes represents phase changes.

The same endothermic reaction in DSC is observed, with no evidence of phase changes. The rate of weight loss changes at approximately 100ºC and 300ºC can be seen. The reason the weight loss is finalized at 300ºC instead of 250ºC, which is predicted by the DSC curve, is due to the difference in the heating rate. In TGA, the heat rate was

50ºC/ min; and in the furnace, the heat rate was maintained at 230ºC over the period of 23 hours.

The P-25 TGA history stabilizes at 4% weight loss, while our samples stabilize at approximately 9-10% weight loss. Notice that these differences in the weight loss are indicative of surface area differences between P25 and this thesis' samples.

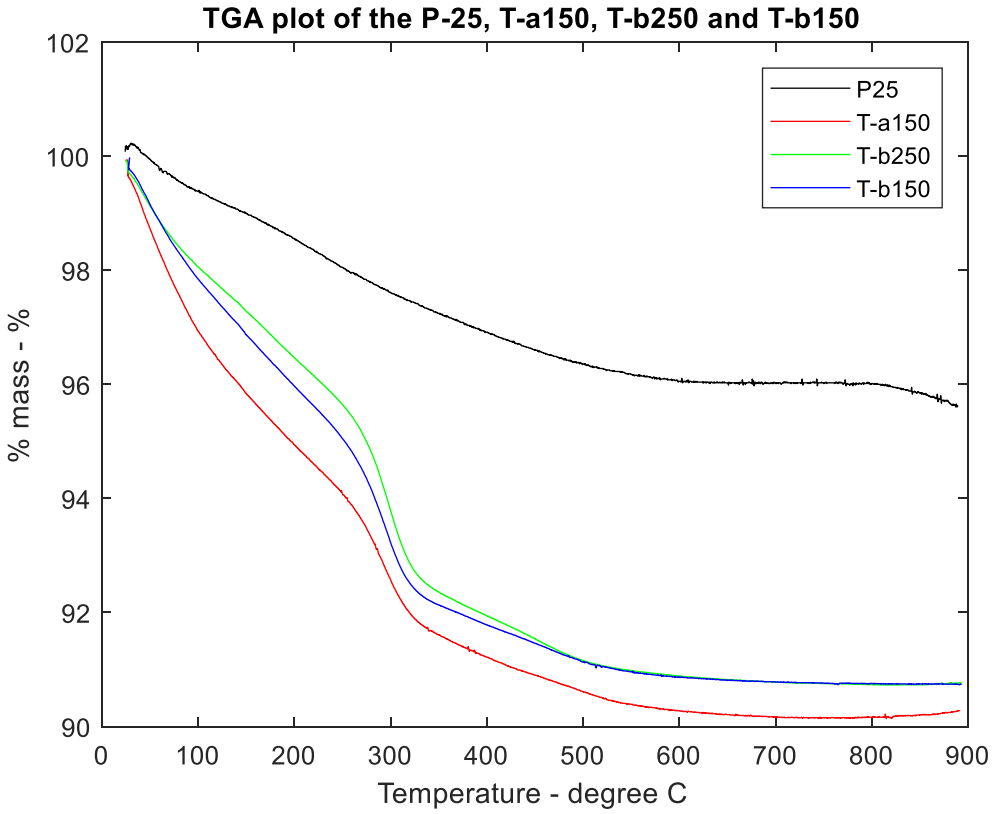

Figure 18 TGA of P25, Ta150, Tb150, Tb250

3.3 Microscopy Imaging

Other tools that are used include microscopy imaging, i.e. scanning electron microscopy (SEM) and transmission electron microscopy (TEM). These two techniques

use electron beam (instead of visible optical light), thus capable of resolving nm spatial resolution. Their differences lie in the mode of operation and scales involved.

3.3.1 SEM

While the SEM source of illumination is electron beam, the primary mode of operation is distinct from that of TEM. SEM operates in scanning mode, similar to cathode ray tube television. It deflects the beam using electron lens in a grid pattern. Differing sample topography produces differing secondary electron emission (or backscatter electron). By rasterizing the samples in this grid pattern, an image is formed with topographical information. Interesting consequence of this topography information is by tilting the sample (either induced by lens focus or physical tilt), one can create 3D-SEM, stereo vision[46,47].

SEM is typically used to observe material from millimeter to submicron scales. It does not resolve well at nanometer scale. One of the advantages of SEM is the wide range of scales that it can detect. For example, Figure 19 shows a picture of P25 samples observed under SEM. At micron level scale, the resolution has relatively good signal to noise ratio; however zooming in to the 100nm scale, the clarity of the picture diminishes, requiring use of different tools to assess morphology of the sample.

These SEM pictures reveal particle-like clustering at the micron level, along with dendritic-like aggregation of the nanoparticles. For example, less aggregation in the solution method may be achieved using surfactant during synthesis.

In this work, Zeiss Sigma Field Emission SEM with Oxford EDS LEO is used to image on micron scale morphology and to determine chemical composition using EDS phase analysis.

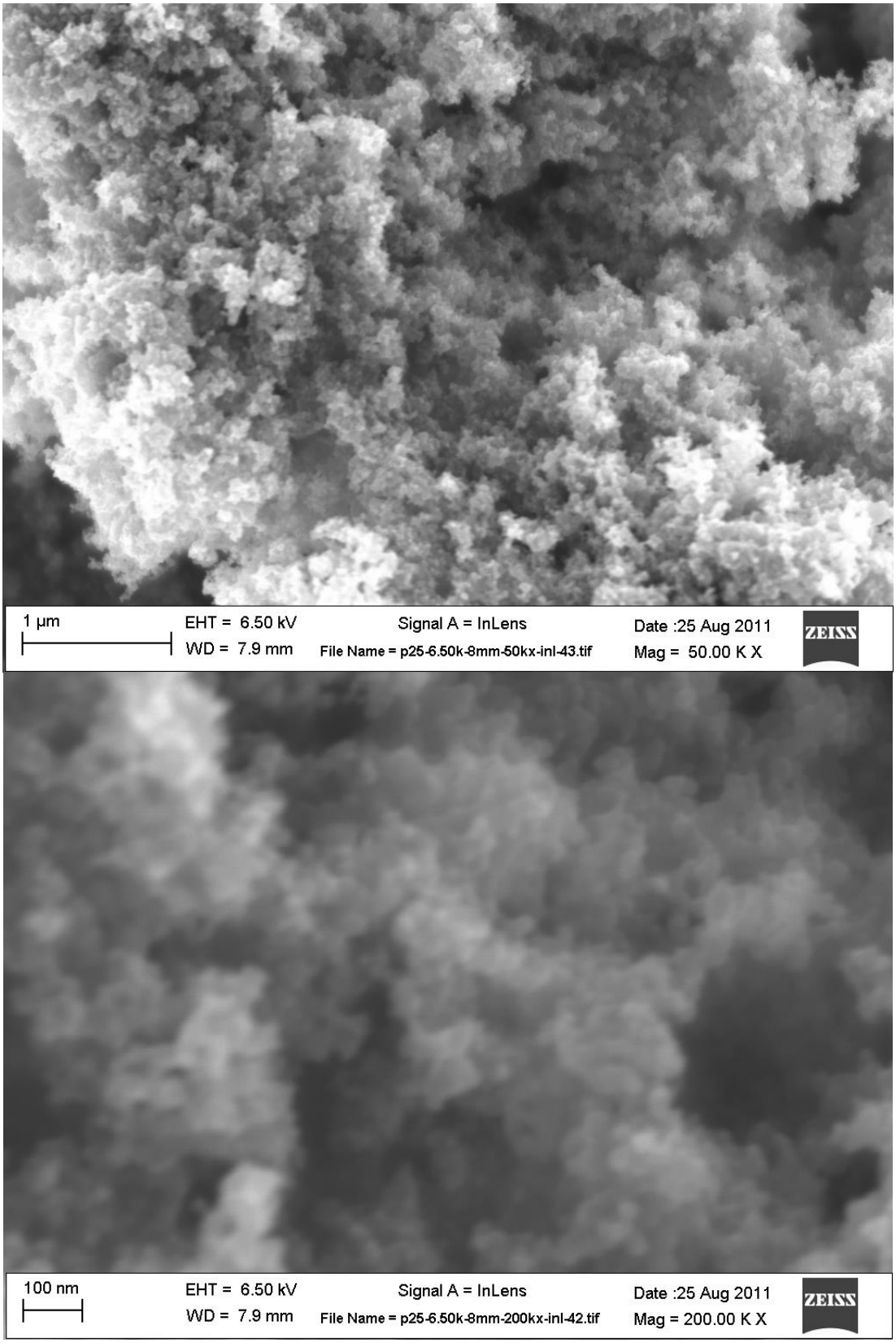

Figure 19 P25 SEM 50kx and 200kx

3.3.2 TEM

Given the limit of the SEM in resolution, the transmission electron microscope (TEM) becomes valuable. TEM is capable of very-high magnification images; however, the samples need to be dispersed in solution and dropped on lacey carbon grid. This process self-select particles that are able to attach themselves to the lacey carbon grid. However, by being able to resolve sub-nm features, this is the method of choice to analyze nanoparticles[46,48].

TEM operates similar to an optical microscope, bending the electron beam (light) using a magnetic field (lens) to generate the magnification necessary. The difference lies in the fact that the electron beam transmits through the sample in TEM, while in an optical microscope, the light is reflected off the object. Another interesting note for the TEM is that the electron beam passes through the samples in what is estimated to be a parallel beam. Unintended consequences of this is the TEM reflected depth by differing illumination because of electron absorption, where bright spots represent electrons passing freely; and dark spots represent electrons obstructed by the sample.

In a standard TEM mode, through interesting engineering and mathematical modeling, if this parallel beam passes through crystal-like structure, a diffraction pattern (similar to XRD) will be observed. This enables scientists to obtain crystallinity information at the nanometer scale.

Here, JEOL 2010F with EELS and EDX is used to determine nanometer scales morphology. JEOL2010F can be used in scanning mode, enabling compositional analysis.

3.3.2.1 STEM

Advancements in technology related to high voltage stability and magnetic lens have enabled engineers to run TEM in scanning mode. STEM operates similar to its SEM counterpart, by measuring the secondary electron emission. The primary advantage of STEM arises from determining the elemental composition enabled by the scanning mode.

3.4 Phase analysis

Another important characterization that is used for material science is phase analysis. The nanoparticles here are generally crystalline in structure. Crystallinity can be defined by the long-range-order arrangement of the atoms within the material. If the source of illumination is selected to be on the same order as these arrangement, diffraction phenomena arise. The interrogated sample can be determined to be single crystal or not based on the diffraction spectra[46,49,50].

3.4.1 XRD

Crystallinity analysis usually starts with XRD. Twelve point five percent of a 6nm nanoparticle atom is actually composed of short range order surface atoms[16]. This fact

inherently makes X-Ray diffraction (XRD) a non-optimal method to characterize nanoparticle phases. From the XRD spectra, a 24 hour scan of the nanoparticles yields a very-low signal count. Typically 10000 intensity counts are expected over minutes of scan. However, in spectra of our nanoparticles yielded 1000 counts for a 24 hour scan. While it is possible to distinguish the crystallinity, XRD is definitely not the method of choice to characterize these nanoparticles. In fact Schlabach, Brown, Choi, and Wu recommended against using XRD for crystallinity identification for nanoparticles smaller than 10nm[51-54]. Furthermore, Schlabach coined the term "onset of ordering", with 10nm as the limit of when the XRD technique starts to fail. Some studies also attribute quantum confinement as the reason why the spectra broaden as particle size falls from 14.2nm to 6.8 nm[55].

As shown in Figure 21 and Figure 22, one can observe that using a standard glass slide and scotch tape method yields background that can interfere with the sample. One can observed from Figure 22 that there is some sort of signal; however the signal-to-noise ratio is very low. To circumvent this high background signal, a zero background sample holder is used, along with a better tuned Expert Phillips. This setup yields the XRD spectra depicted in Figure 22.

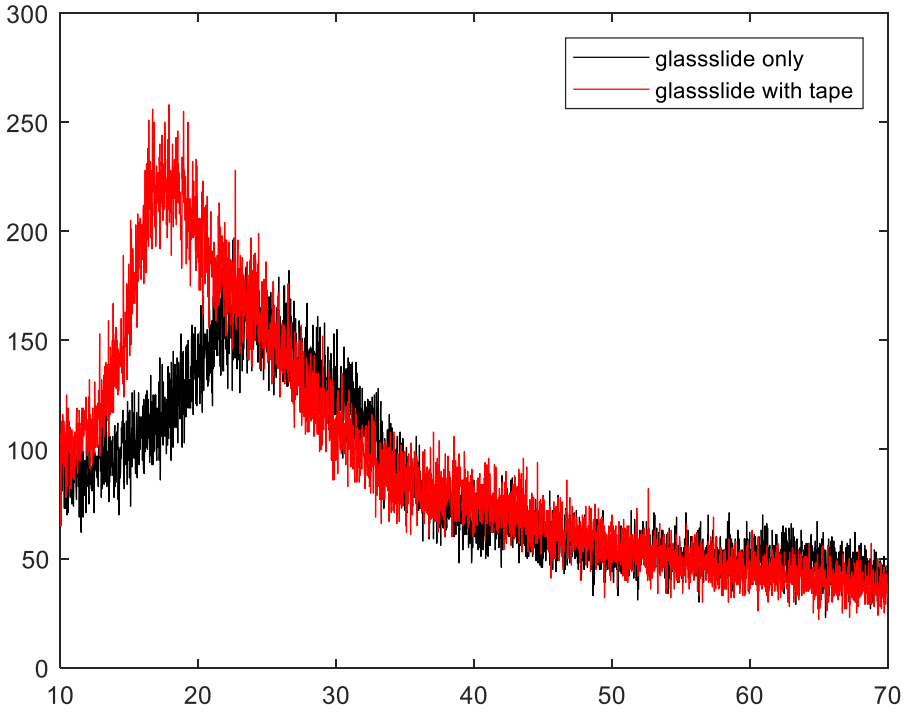

Figure 20 XRD - Low Resolution - background only

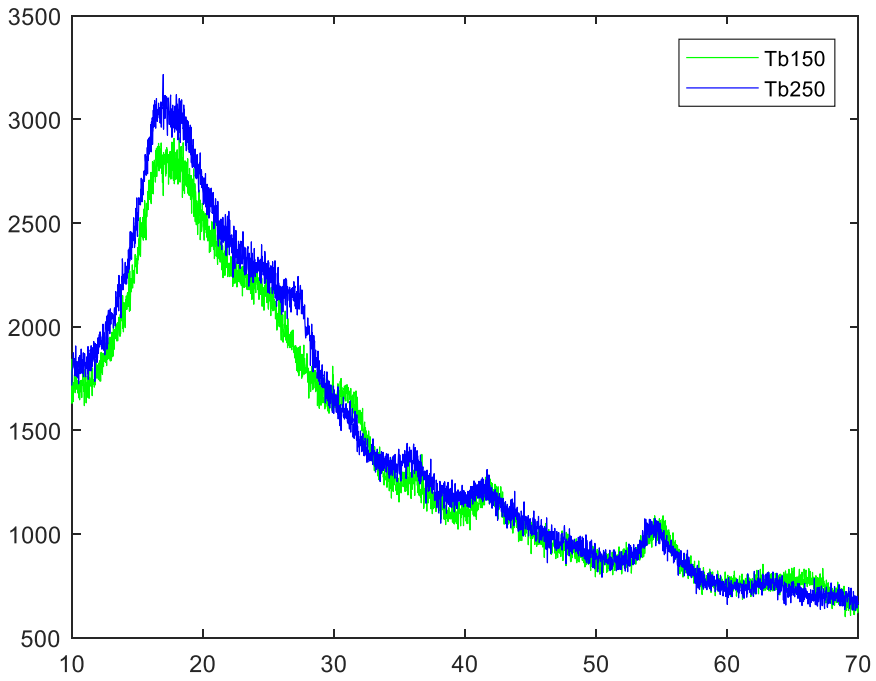

Figure 21 XRD low resolution - with samples, Tb150 and Tb250

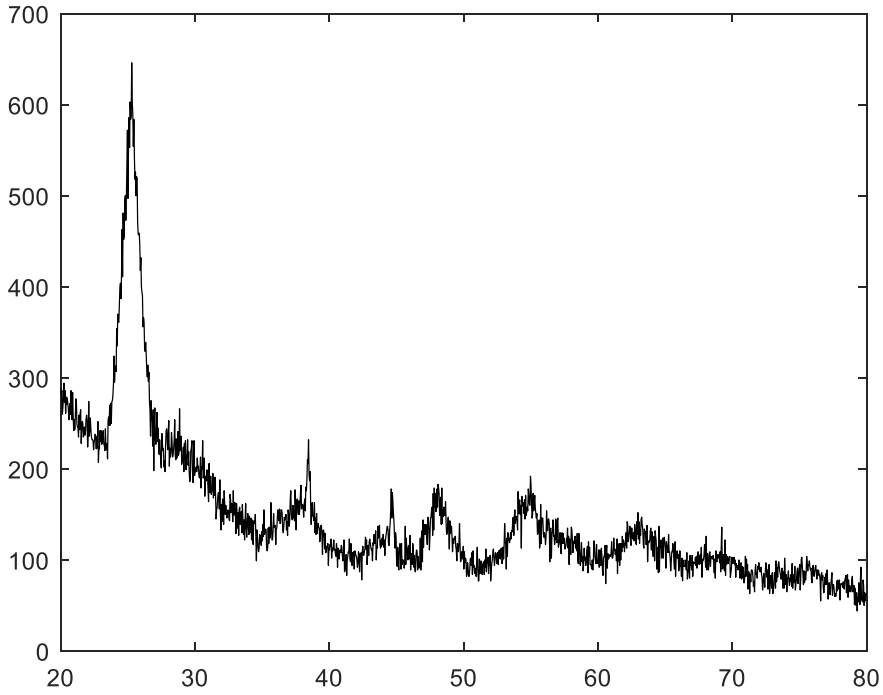

Figure 22 XRD of Ta150 with zero background sample holder

3.4.2 SAED

Using TEM, the parallel beam section can be diffracted by the atomic arrangement in the specimen. Using this effect as an analysis method is called selected area electron diffraction (SAED). This is another diffraction method that works in the same principle as XRD; but by using an electron beam. The electron beam has smaller wavelength, thus generating narrower band[46,48].

3.4.3 Determination of Srilankite, instead of Brookite

Orthorhombic Pbcn (Srilankite) and Pbca (Brookite) space groups have similar spectral signatures. Their main differences lie in their intensity, with similar peak location. This is partly due to these structures sharing orthorombic structure, which is why it is important to use two different phase analysis methods to confirm that the Srilankite phase and not Brookite.

3.4.3.1 SAED

SAED spectra of Tb300 and Tb100 serves as first evidence of srilankite presence. The blue sample (Tb100 and Tb150) SAED spectra indicate that they are composed primarily of Srilankite phase. Tb300 is overlaid with the PDF# 99-000-3236 to reveal that the peaks that are detected in the spectra come from rutile. The Tb100 spectra identifies with PDF# 97-000-5328, which corresponds to srilankite. Traces of rutile also exist in Tb100.

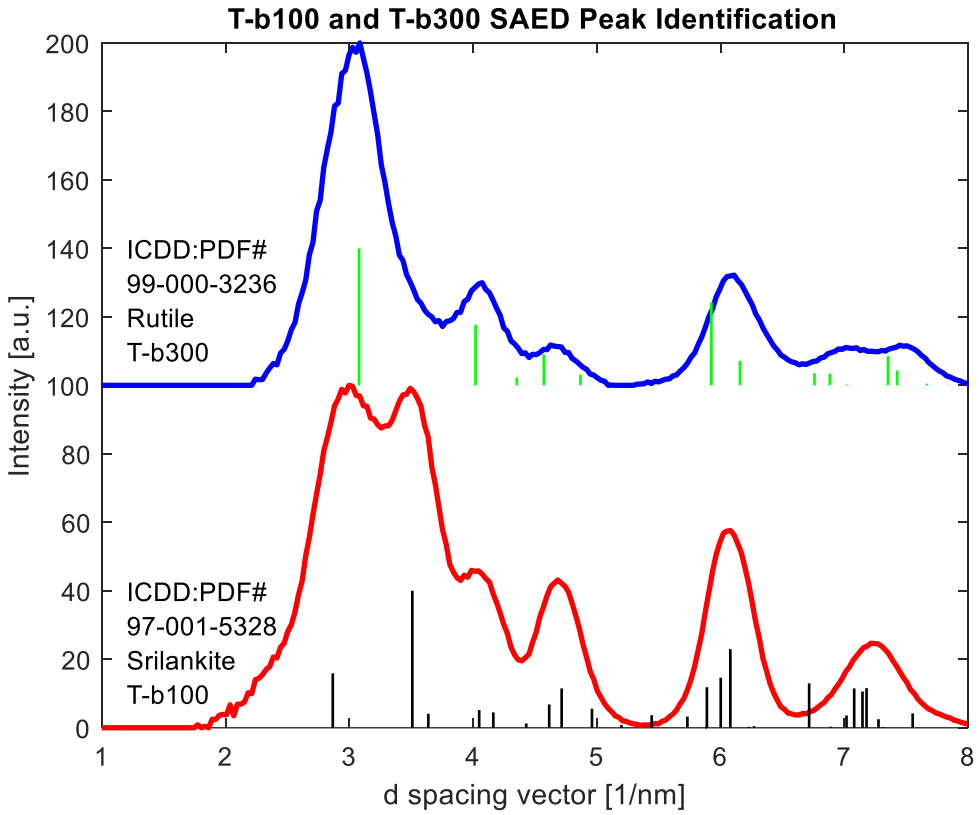

Figure 23 Tb100 and Tb300 comparison

To clarify these differences, the XRD database from the International Centre for Diffraction Data (ICDD) is consulted. These expected diffraction angles can be converted to the d-spacing vector. This way, the SAED data can be analyzed. In crystallographic diffraction, the peak location and the relative peak intensity should match the database. For rutile, the peak location and peak ratio are comparable to that found in the ICDD database. However, for the srilankite, while the peak locations match, the peak ratios are somewhat different for the 2.9 and 3.4 nm^{-1} peaks. Another key point here is the grouping of peaks in the Brookite phase at 5.3 nm^{-1} are not present in the Tb100 sample. This is how we come to the conclusion that these are Srilankite phases.

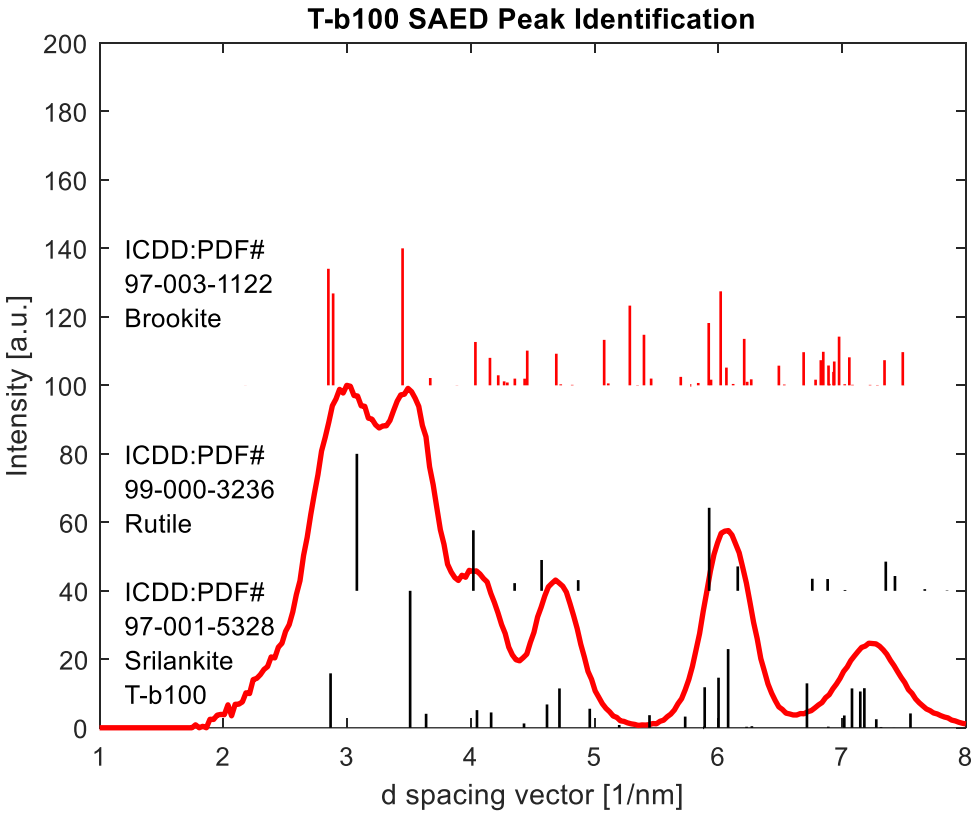

Figure 24 Tb100 SAED compared to Srilankite, Rutile and Brookite ICDD

3.4.3.2 XRD

The same conclusion can also be drawn by using XRD. Shown below is the Tb150 sample where the sample spectra is compared with the ICDD database. Combining this knowledge with SAED spectra, we confidently draw the conclusion that this is indeed Srilankite phase. Note t peaks are not observed in at 48 degrees, equivalent to the missing 5.3 nm^{-1}; consistent with the absence of the brookite phase.

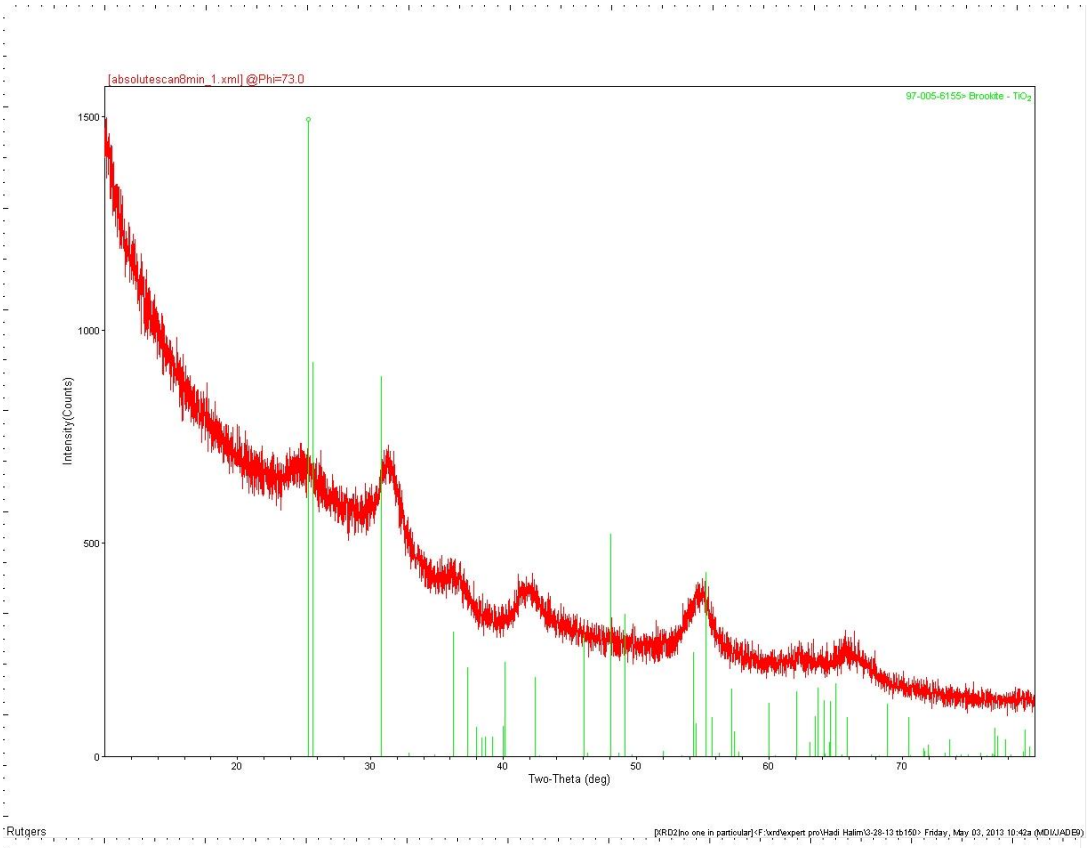
[absolutescan8min_1.xml] @Phi=73.0
97-005-6155> Brookite - TiO2
Intensity(Counts)
Two-Theta (deg)
Rutgers
[XRD2]no one in particular]<F:\xrd\expert pro\Hadi Halim\3-28-13 tb150> Friday, May 03, 2013 10:42a (MDI/JADE9)

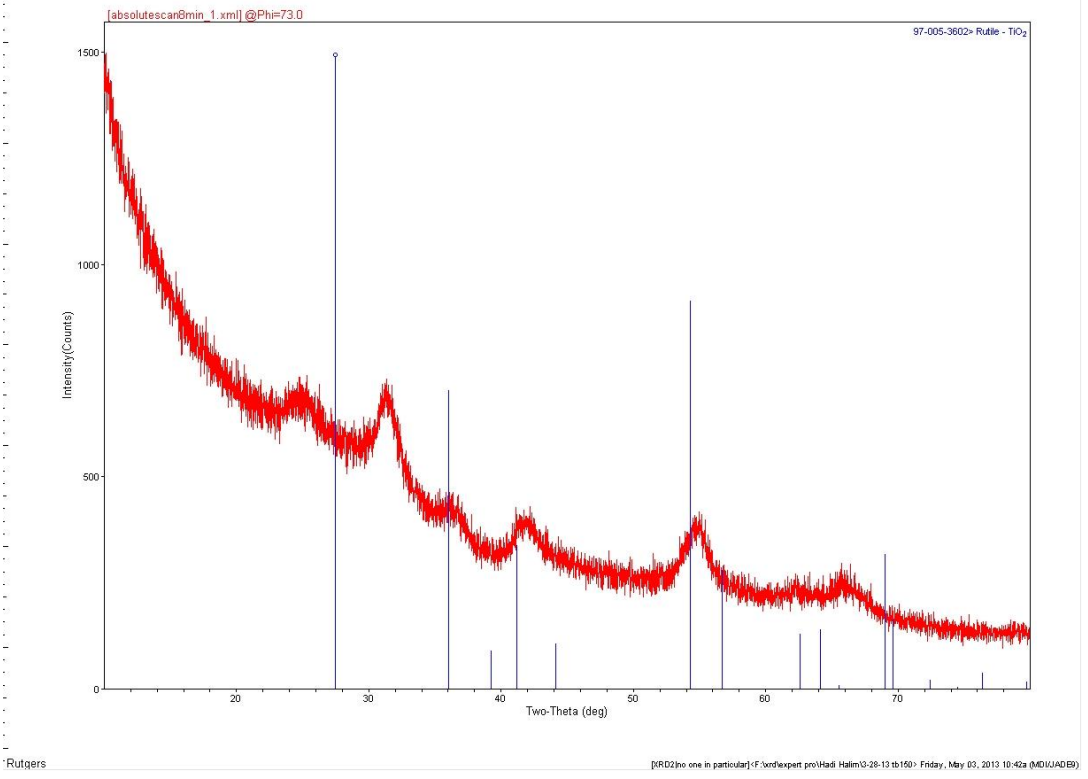
[absolutescan8min_1.xml] @Phi=73.0
97-005-3602> Rutile - TiO2
Intensity(Counts)
Two-Theta (deg)
Rutgers
[XRD2]no one in particular]<F:\xrd\expert pro\Hadi Halim\3-28-13 tb150> Friday, May 03, 2013 10:42a (MDI/JADE9)

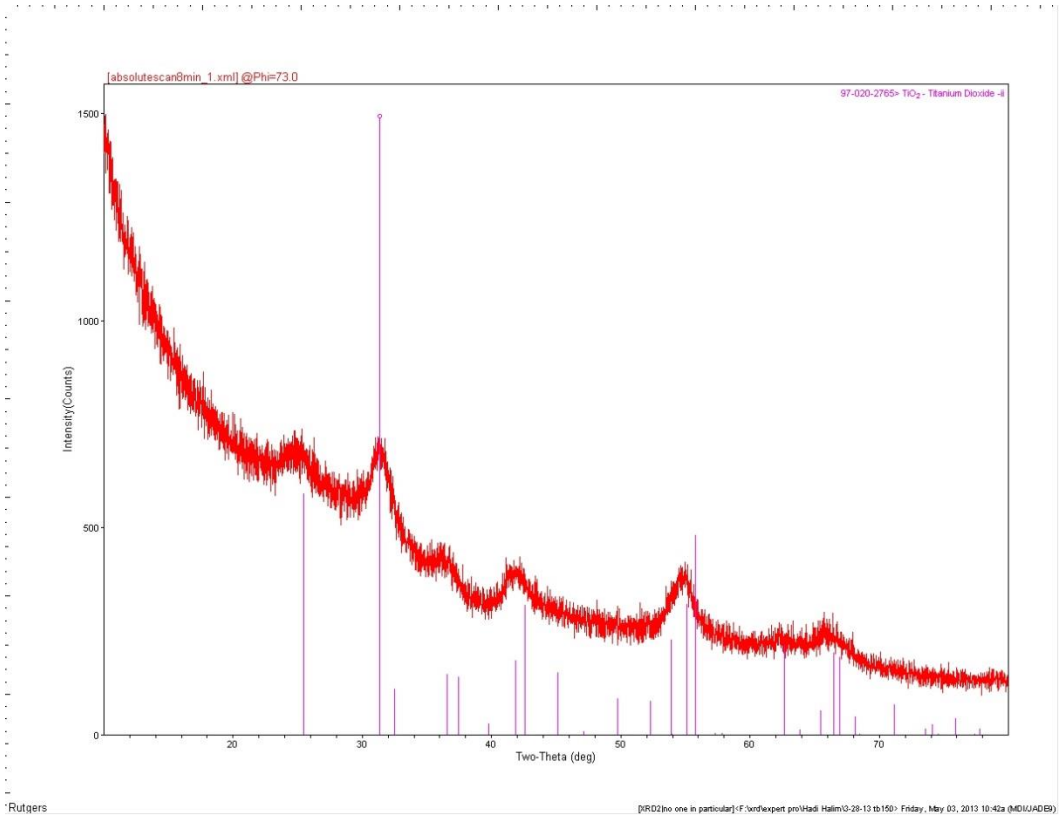

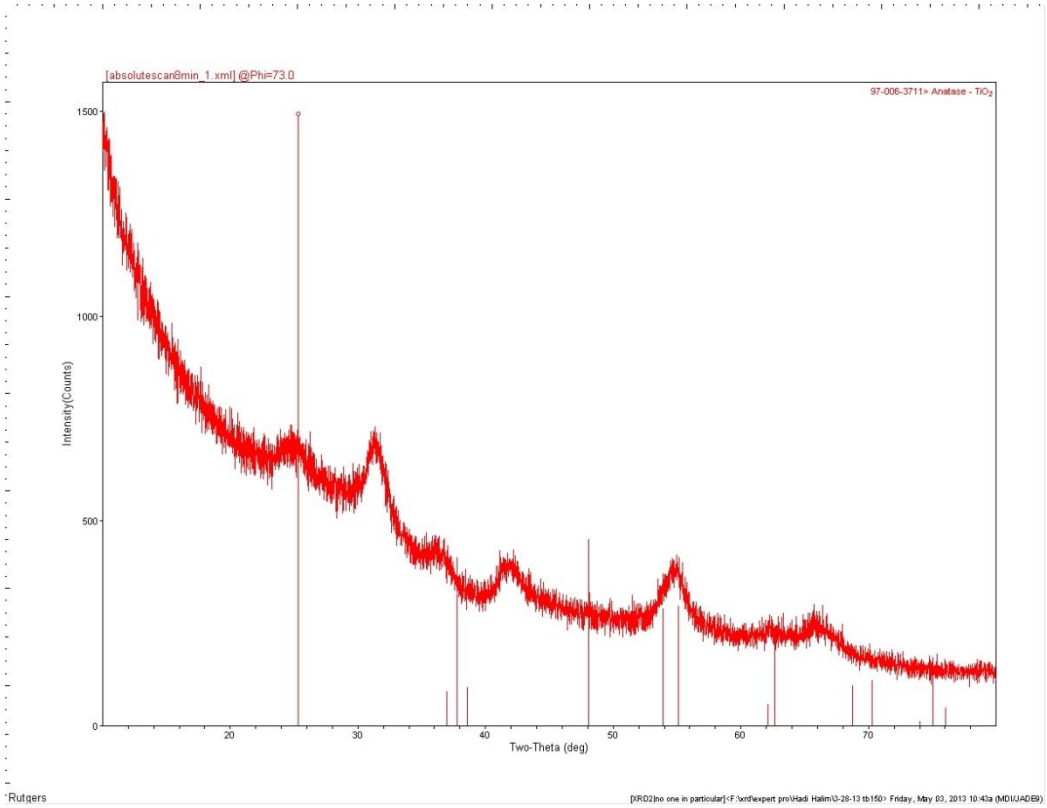

Figure 25 Tb150 compare to different ICDD database using Jade

3.5 Elemental composition

Material characterization is incomplete without analysis of the chemical composition. To do this, there are various methods that can be used, including from X-ray fluorescence – energy dispersive spectra (XRF-EDS), X-ray fluorescence – wave dispersive spectra (XRF-WDS), electron energy loss spectroscopy (EELS), and X-ray photo-electron spectroscopy (XPS). Together, chemical composition and phase composition, construct the cornerstone of material characterization.

In this work, XRF-EDS is used, administered by TEM and XPS. Together they provide not only elemental composition, but also binding energy information.

3.5.1 XRF–EDS

XRF is a phenomenon where samples re-emit a portion of the incident light with lower energy light. In this case, the incident light is X-Ray, typically by copper K-alpha. This chemical composition has enjoyed a wide range of interrogation window from millimeter range (standard non vacuum equipment); micron range (SEM attachment); to nanometer range (TEM attachment). The versatility and scale variation of this method has asserted this method as a standard elemental composition tool. Because of the X-Ray interaction with the material, in a tear drop shaped penetration region, XRF-EDS act as a volumetric composition method in our nanometer sample[48].

Here is an example of spectra generated by using TEM. As shown in the Figure 26, the composite survey scan shows different colors that are superimposed to generate an elemental mapping. Copper signal is present with low intensity, recognizing that lacey

carbon is on top of the copper grid, which serves as the sample holder. The carbon in the lacey forms are observed, indicating the supporting carbon layer. What is important to note is the fact that the carbon signal exists whenever titanium and oxygen signal exist.

Whenever there is titanium signal, oxygen and carbon signals (Titania nanoparticle) are present, in contrast to areas where there is no titanium signal but carbon (lacey support) can still be seen. Because of the volumetric interrogation volume of this method, the carbon distribution may not be uniform across the particles. One can only assert that carbon is distributed across the titania nanoparticles.

.

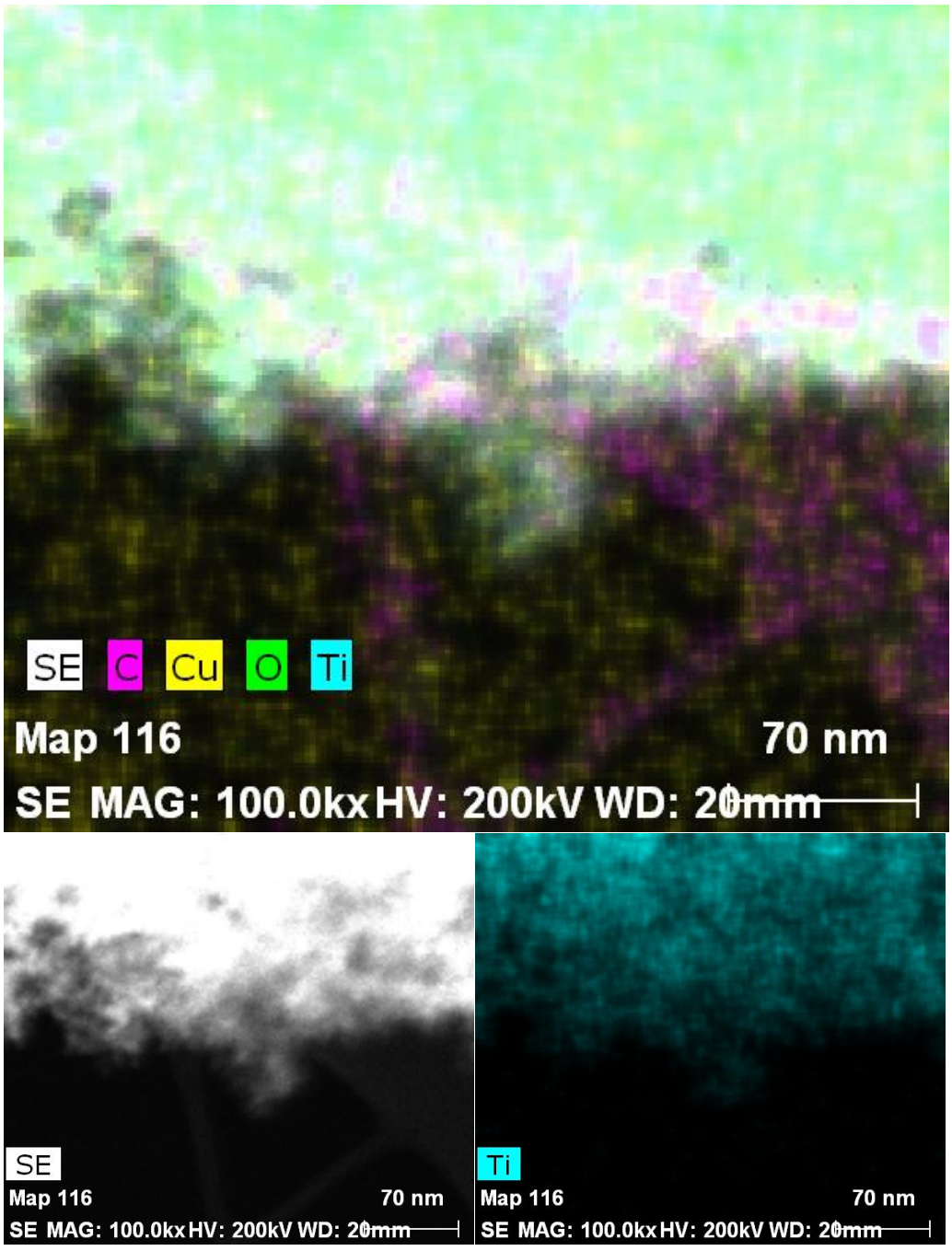
SE C Cu O Ti
Map 116
70 nm
SE MAG: 100.0kx HV: 200kV WD: 20mm
SE
Map 116
70 nm
SE MAG: 100.0kx HV: 200kV WD: 20mm
Ti
Map 116
70 nm
SE MAG: 100.0kx HV: 200kV WD: 20mm

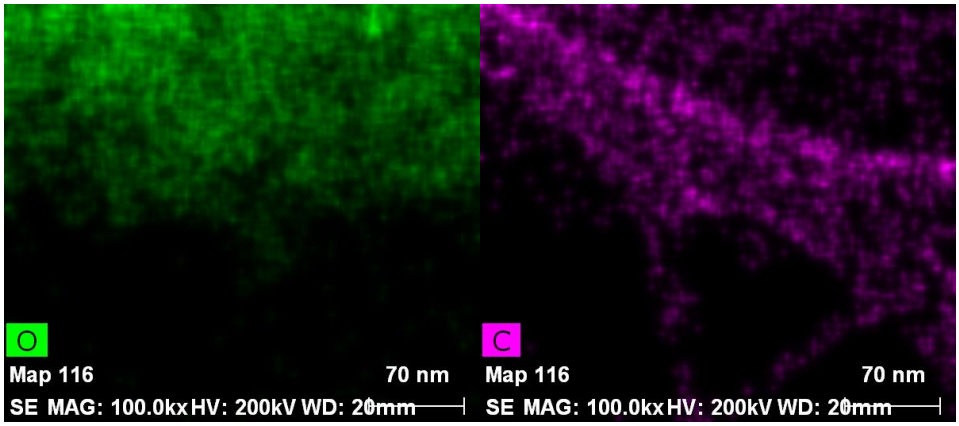

Figure 26 XRF-EDS spectra mapping of TEM on Tb150

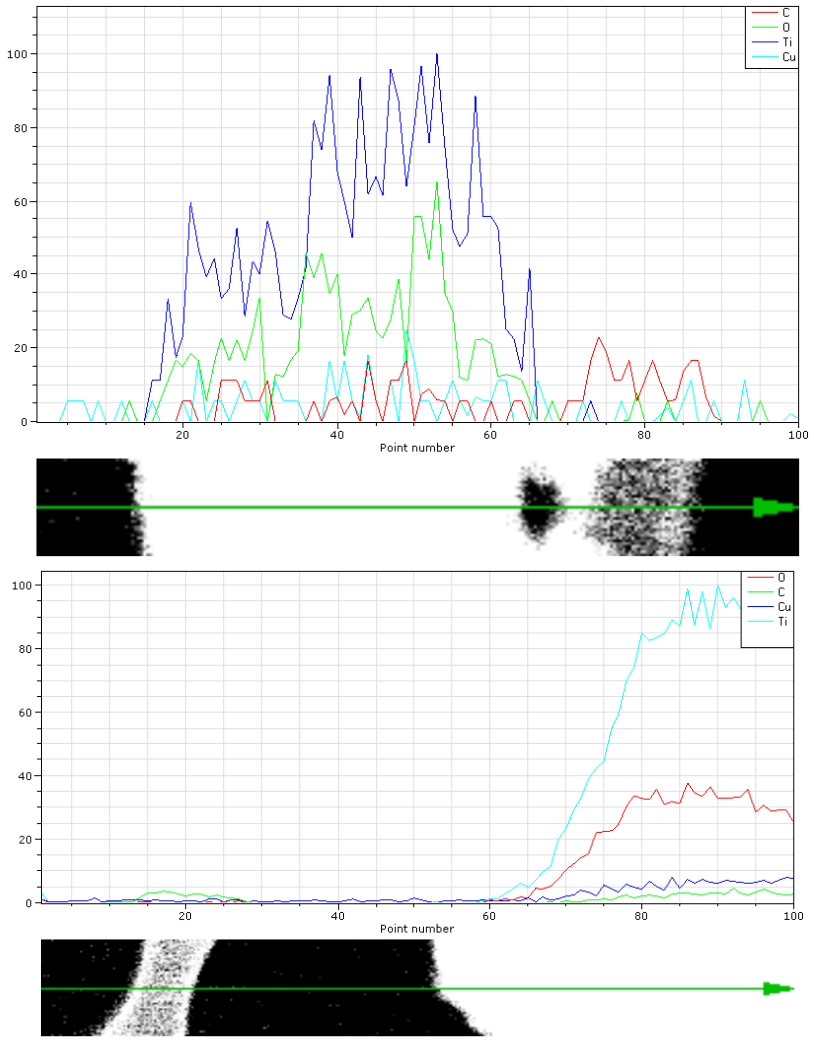

Figure 27 XRF-EDS line scan on TEM on Tb150 (left) and Tb250 (right)

3.5.2 XPS

Considering that ethylene and titanium tetra iso-propoxide (TTIP) are used as precursors, the samples may be carbon doped. Since nitrogen gas also present, we need to find a way to confirm that there is no Nitrogen doping. Another type of doping that maybe present is Ti-C. These bonds will be explored in the following analysis.

In order to show the dopant and the dopant state, X-ray photoelectron spectroscopy (XPS) is employed. XPS works in a similar fashion to XRF, but through a different mechanism, allowing identification of the binding energy, thus providing assessment of the type of chemical bond existing within the sample. From the XPS survey scan, no nitrogen doping is detected in our system. Conversely, the carbon peak is clearly visible in the spectrum scan.

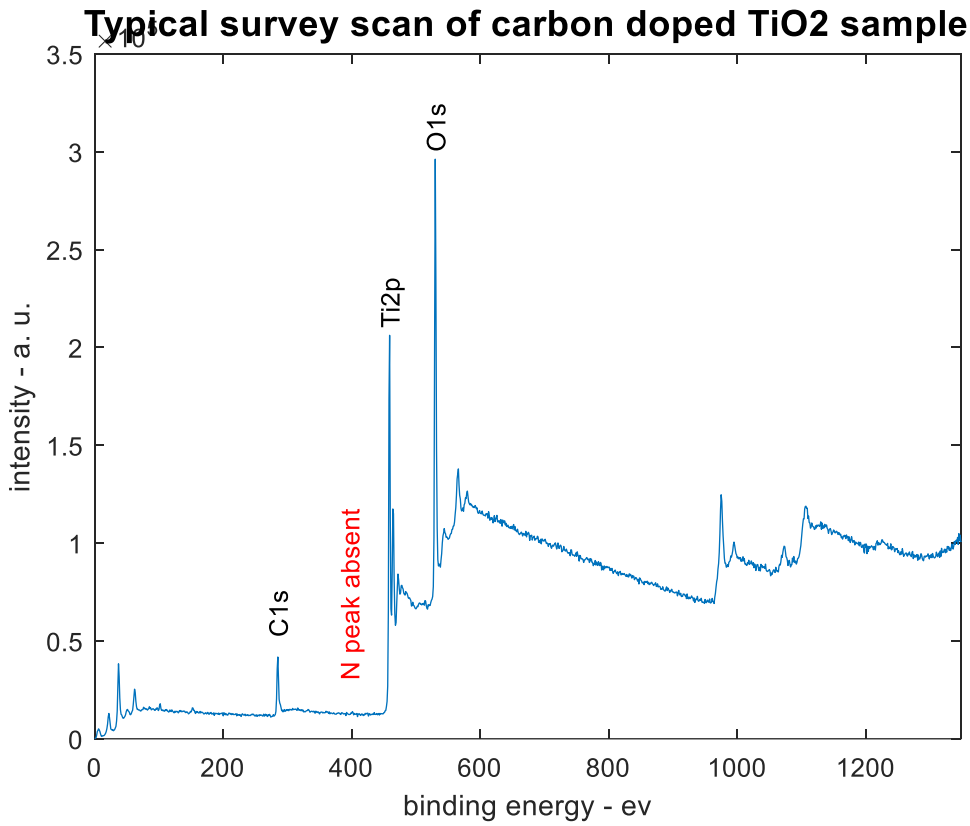

Figure 28 X-Ray Photoelectron Spectroscopy survey scan of doped TiO2 sample.

A more detailed look of the XPS spectra will provide much more information about the type of chemical bonding that exists. The first observation can be made from the long (exposure) scan in the titanium XPS peak. The Ti^{4+} peak (458 and 471 eV) is readily visible from the spectra[56]. The 464 and 477 eV are reportedly the satellite features from the Ti^{4+} peak. [57] From our XPS, Ti^{3+} is not visible, which would have existed at 455 and 461 eV. Neither are other lower valences Ti visible. [58] Thus, our samples are composed of titania (not Ti_2O_3 or other Ti-O Magneli phase) [57].

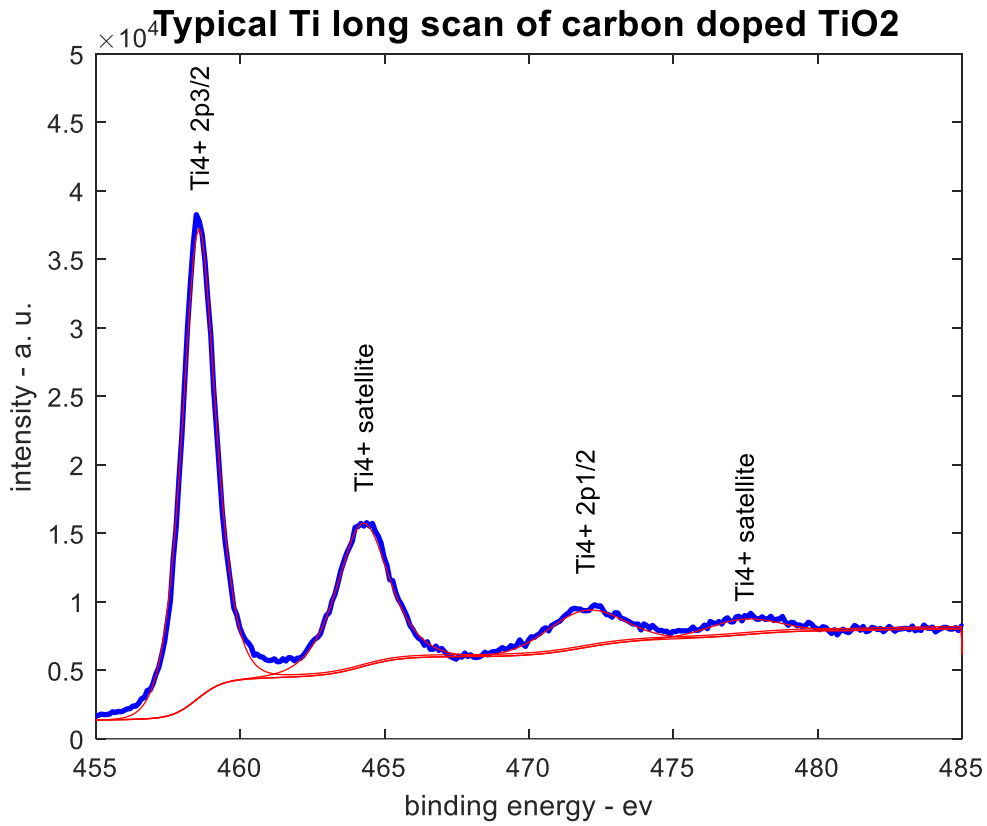
Typical Ti long scan of carbon doped TiO2
×10^4
5
4.5
4
3.5
3
2.5
2
1.5
1
0.5
0
intensity - a. u.
Ti4+ 2p3/2
Ti4+ satellite
Ti4+ 2p1/2
Ti4+ satellite
455
460
465
470
475
480
485
binding energy - ev

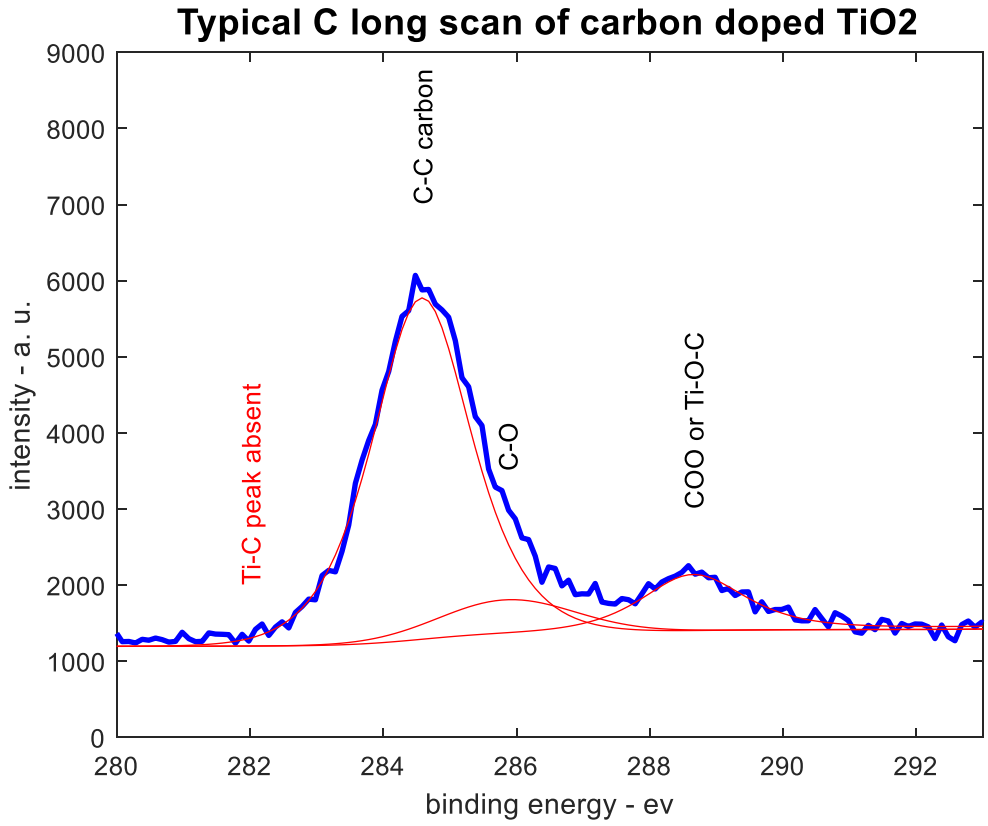
Typical C long scan of carbon doped TiO2
9000
8000
7000
6000
5000
4000
3000
2000
1000
0
intensity - a. u.
Ti-C peak absent
C-C carbon
C-O
COO or Ti-O-C
280
282
284
286
288
290
292
binding energy - ev

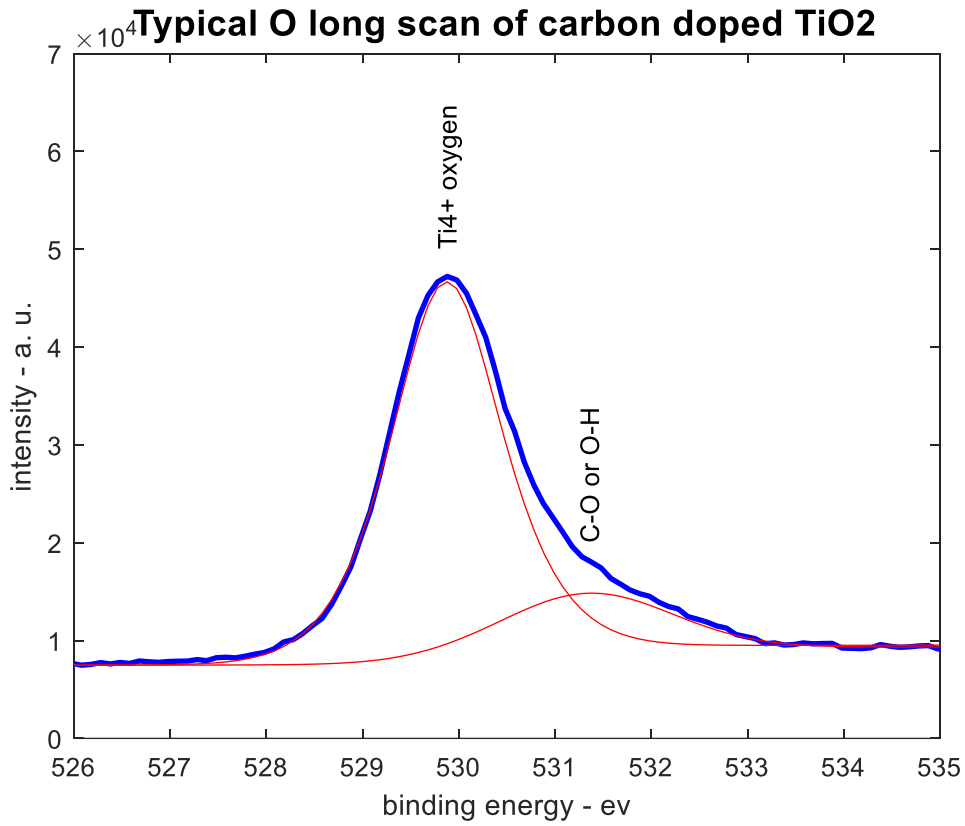

Figure 29 X-Ray Photoelectron Spectroscopy long scan of doped TiO2 sample.

Another important observation is in the C XPS peak. First, the Ti-C peak is absent. The typical carbon doping feature in the literature is the Ti-C type (oxygen substitution). The XPS carbon peaks at 284, 286, and 288 eV are usually denoted as adventitious carbon, i.e., C-O bond and COO bond. From here, one can hypothesize that the type of bonding that exists in our system must be interstitial (from the adventitious carbon) and Ti-O-C type bonding (titanium substitution). [58]

It was hypothesized that the Ti-O-C type bonding came from the incomplete composition of precursor. During the titania synthesis process, the rapid collision

between the precursor and the gases must have destroyed most of the bond. However, the bond energy of C-C is indeed weaker than the C-O bond, by 83 to 86.5 kcal/mole (3.60 to 3.75 eV/atom). [59,60] It is not significantly weaker, only differing by 3.5 kcal/mole (0.15 eV/atom). The Ti-C bond, which is 126kcal/mole, is stronger than C-C and C-O, thus is much harder to create[61]. We propose that the C-O bonds that do not break stay in the Ti-O matrix, thus trapping the dopant. On the other hand, the C-C bonds that break will be trapped and remain as interstitial carbon.

To rule out the effect of atmospheric contamination, P-25 industry standard and another titania synthesized using swirl flame (with methane and oxygen as the fuel, fuel lean condition, TTIP as precursor) are compared. The titania from the swirl flame actually exhibits 11.61% carbon, while P25 contains 14.96% carbon. T-a150, T-b150 and T-b250 contain 13.67, 28.5, and 22.0% carbon. In conclusion, ethylene addition definitely increases the carbon concentration in the titania matrix.

Hence, it is concluded that it is possible to synthesize various phases of titania nanoparticles with the low-pressure system. Furthermore, the titania nanoparticles samples are carbon doped, thus changing their color. On deeper analysis of the XPS, one can deduce that our system consists of Ti^{4+} valence, with no oxygen deficient state detected.

In this work, ThermoFisher K-Alpha instrument is used to obtain XPS spectra.

4 Effect of ethylene addition to the previous existing experiment yielding phase changes

In this thesis, the effect of ethylene gas addition to the low-pressure setup is investigated. Several parametric studies are designed to elucidate the transition:

- Ta150 & Tb series – hydrogen-only flame and addition of ethylene to hydrogen flame, respectively
- Tc series – controlled change in flow velocity
- Te series – controlled change in maximum gas-phase temperature
    - Ta200 & Tb100_N11 – similar temperature profiles to compare cases of hydrogen-only flame and hydrogen-ethylene flame
- Tg series – controlled change in ambient pressure
- Th series – controlled change of fuel lean case
- Ti series – Controlled change of fuel rich case

The results of these experiments are grouped into two sets:

1. Parametric study that influences the srilankite-rutile transition.
2. Parametric study that influences the anatase-rutile-srilankite transition.

4.1 Parametric study that influence Srilankite-Rutile transition

The following sets of studies are designed to explore the effect of adding ethylene to a hydrogen flame. The hydrogen-flame case Ta150 is discussed here as a reference to be compared to cases Tb, Tc, Te, and Tg. When ethylene is added, Tb150, srilankite

(with minor rutile) is produced instead of anatase, Ta150. In Tc, Te, and Tg series, the parameters are deviated strategically from Tb150, and no significant phase changes are observed from this srilankite and rutile mix.

4.1.1 Ta150 & Tb series – hydrogen-only flame and addition of ethylene to hydrogen flame

First observation is the change in color. Ta150 is white in color, while Tb100 is dark blue in appearance. Note that the color slowly shifts toward yellow as the cases shift from Tb150 to Tb300. The visible color can be correlated to different phases.

Ta150 samples have color that is usually white. A gradation of color from dark to lighter blue is seen for Tb100 and Tb150 cases, and yellow to lighter hues of yellow is seen going from Tb200 to Tb250 to Tb300 cases.

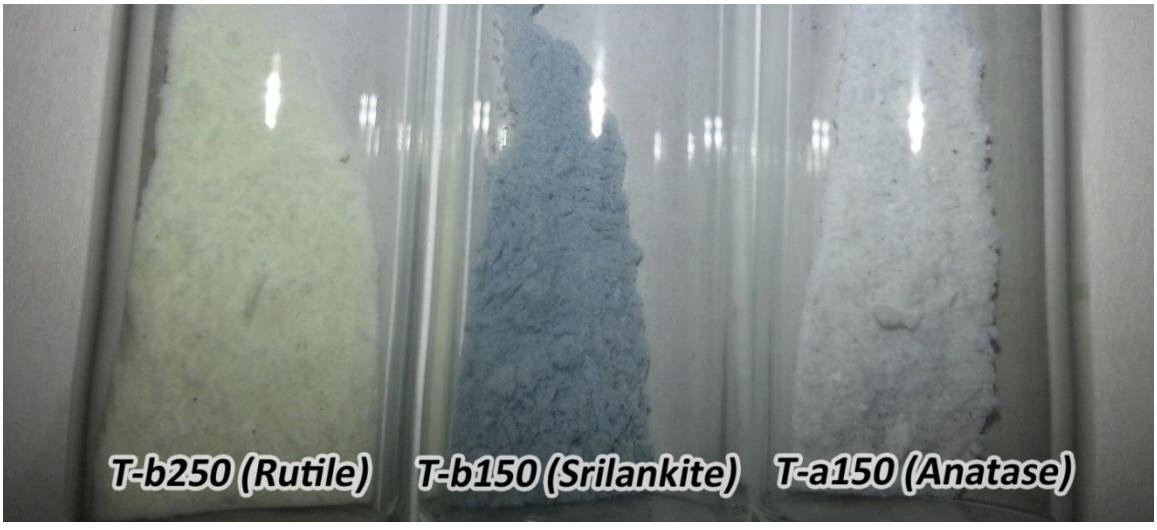

Figure 30 Physical appearances of Ta150 compared to Tb series.

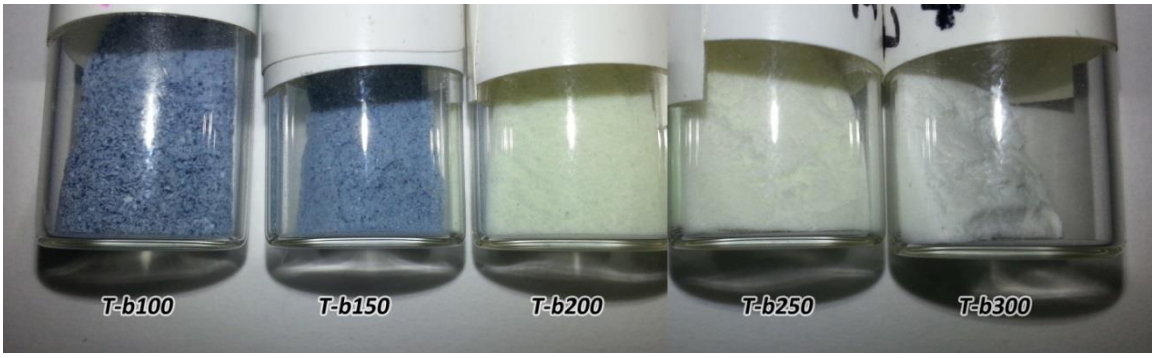

Figure 31 Physical appearances of Tb series (center collection plate).

Considering the crystallinity, Ta150 is anatase dominant with trace amounts of rutile. The main component of Tb150 can be identified as the srilankite phase with trace amounts of rutile. The last sample in this set, Tb250, is primarily composed of rutile phase, with traces of srilankite. The XRD results agree with the SAED results, confirming the phase identification of these samples.

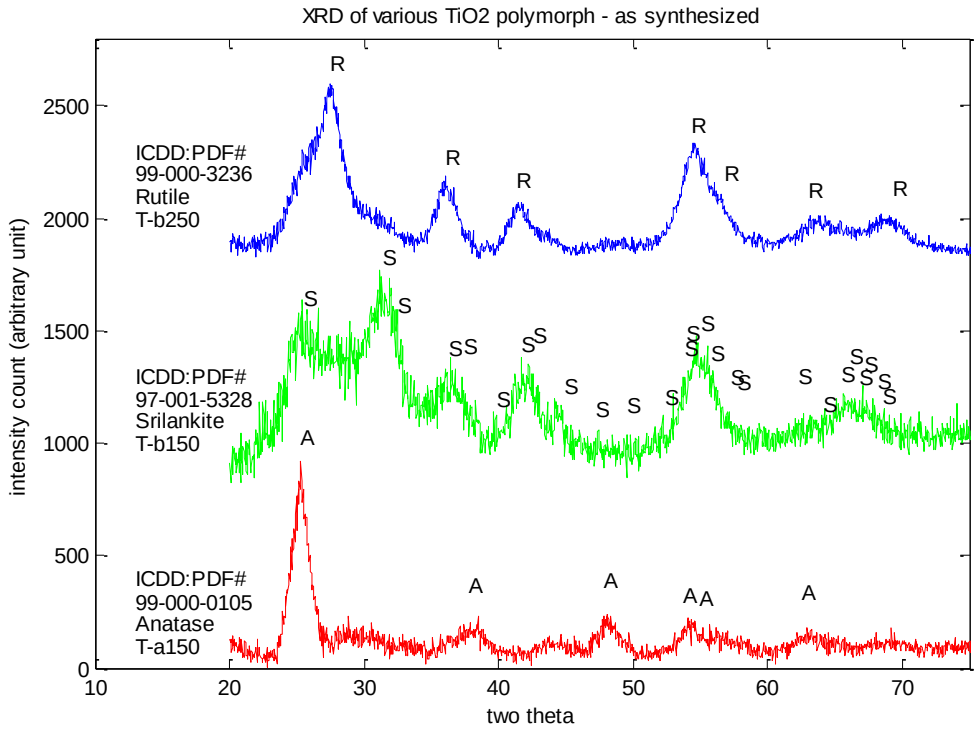

Figure 32 XRD of Tb150, Tb250, Ta150

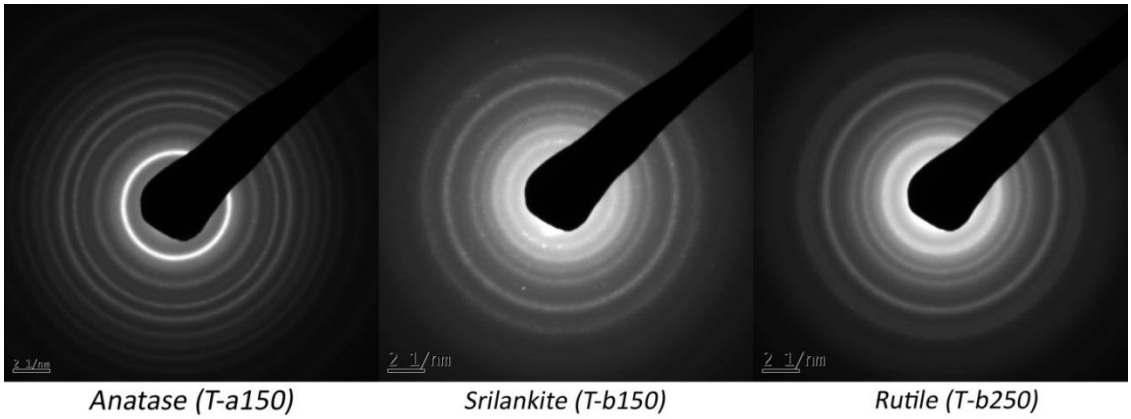

Figure 33 TEM-SAED of Ta150, Tb150, and Tb250

The SAED spectra from Tb100 to Tb300 cases are presented. From this transition, Tb100 is dominated with srilankite phase, with traces of rutile. There are diminishing amounts of srilankite with increasing amounts of rutile as cases move from Tb100 to Tb300, culminating at Tb300 being rutile dominant with traces of srilankite.

The color shift can be correlated to the srilankite composition in the sample. Though, it is unusual to see rutile phase that has yellow hint, which usually indicates the presence of dopant within the samples. Nevertheless, adding ethylene increase the flame temperature from 1560K to 2060K to 2280K. This ethylene addition also corresponds to changing phase from anatase to srilankite–rutile mix, as the color shifts from white to blue-yellow.

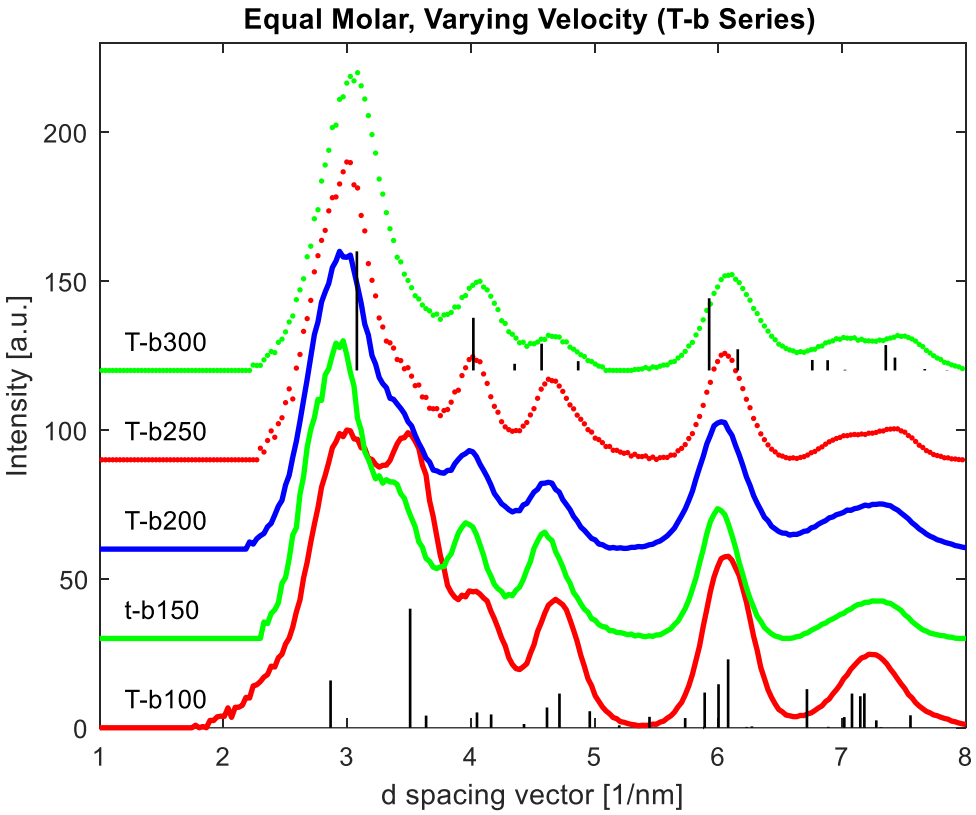

Figure 34 SAED intensity profile of Tb series, indicating the systemic transformation from Srilankite to Rutile as the flame velocity increase.

Morphology-wise, the expected agglomeration is shown in the SEM. The dendritic natures of this agglomeration can be seen, with a mix of micron and sub-micron features, ideal for catalytic processes. SEM is not the best tool to resolve the nanometer features that indicate the primary particle size. To resolve this primary particle size, TEM is used.

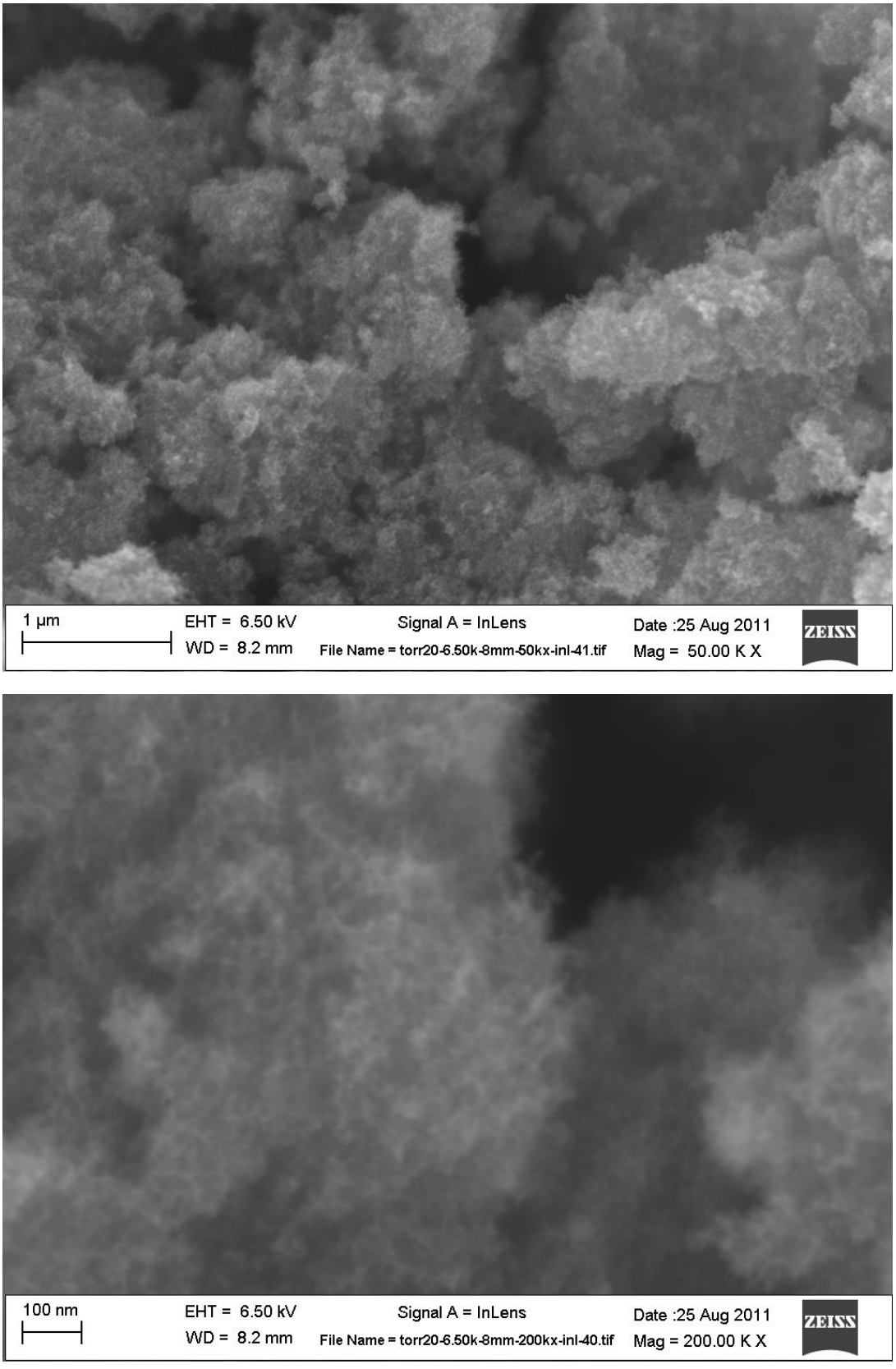

Figure 35 Ta150 SEM 50kx 200kx

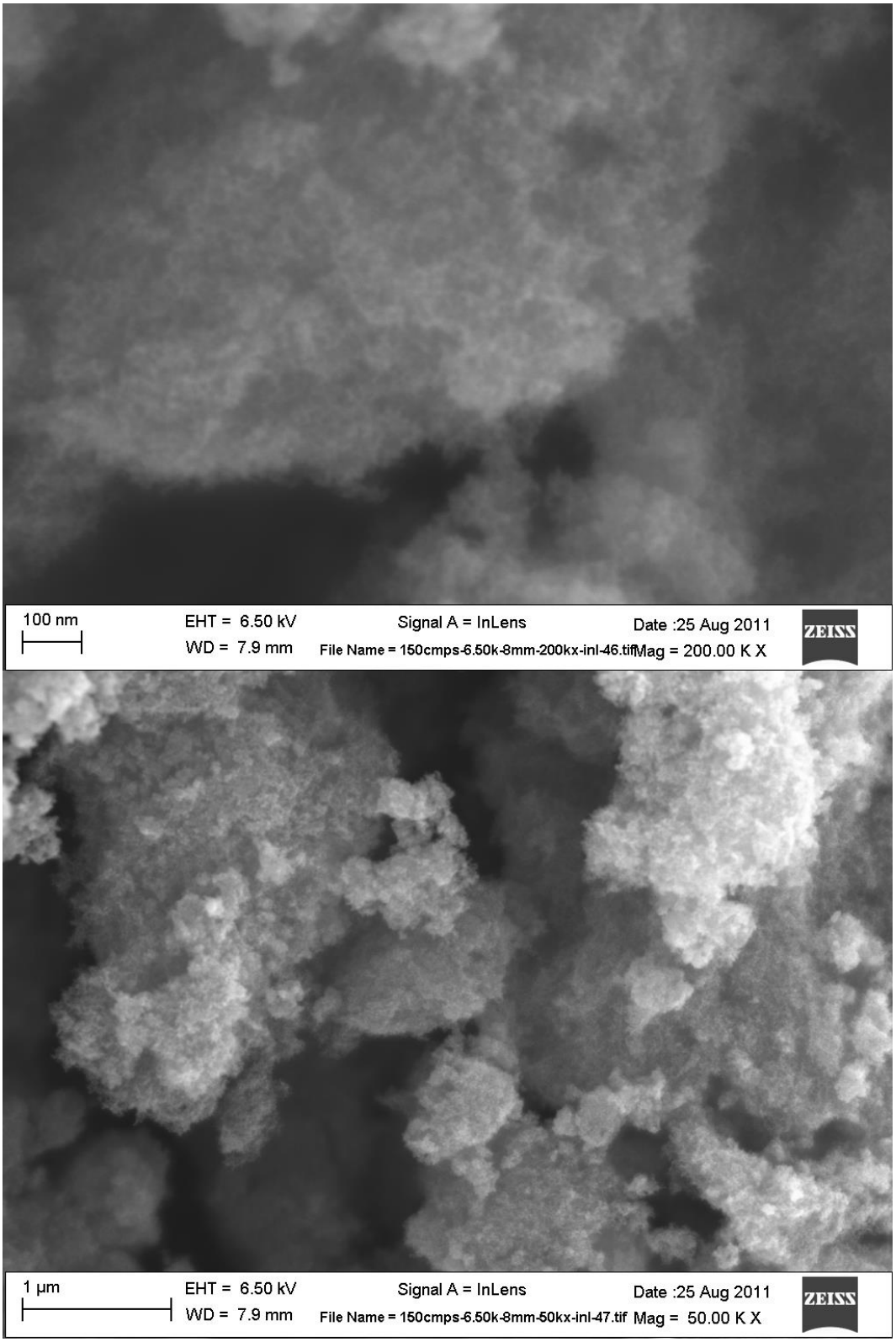

Figure 36 TB150 SEM image, 50kx and 200kx

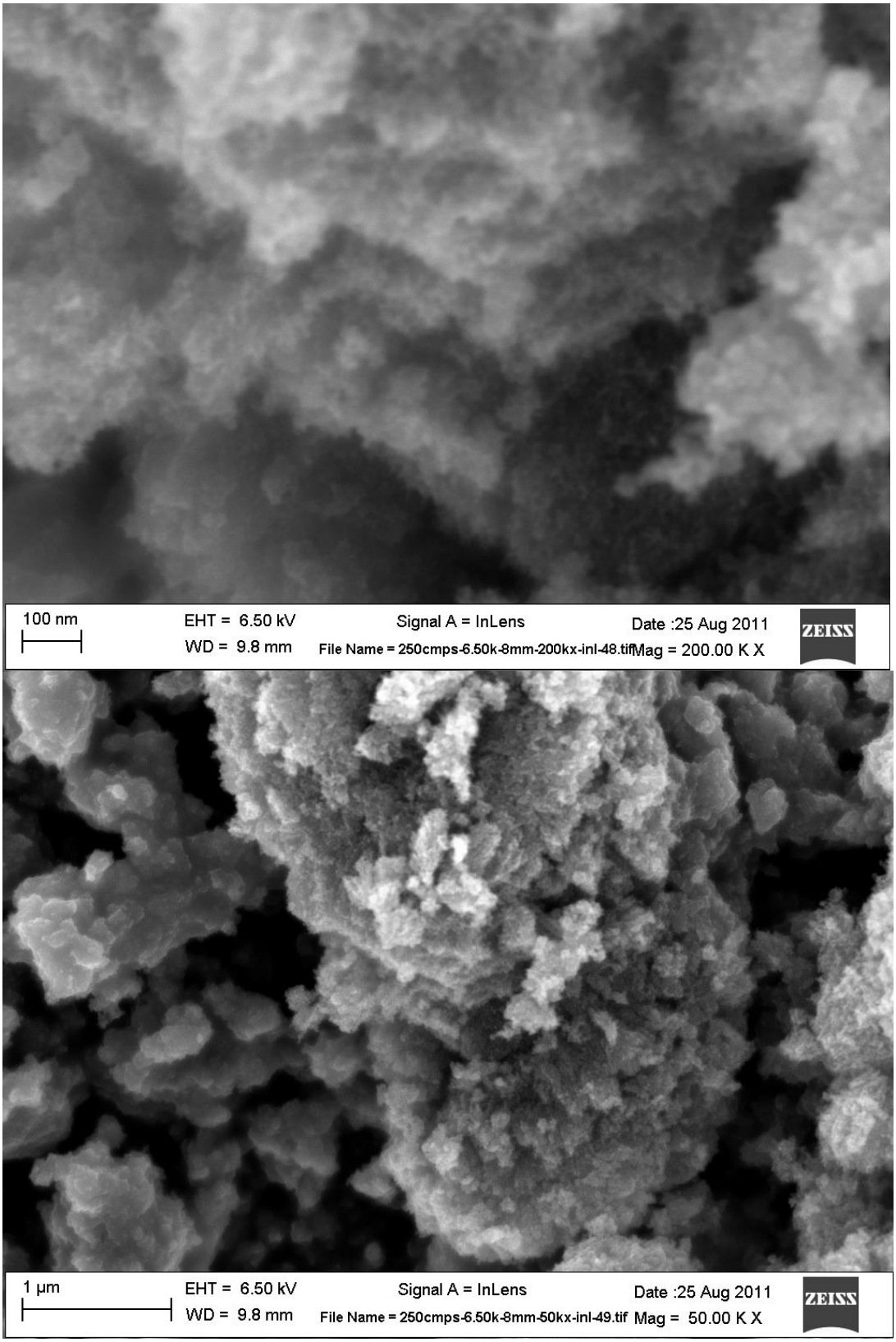

Figure 37 Tb250 SEM 50kx 200kx

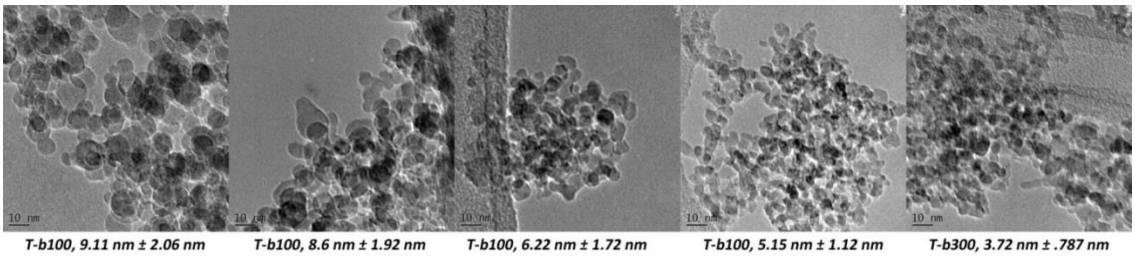

Figure 38 The TEM image of the T-b series, indicate smaller particle size as the flame velocity increase.

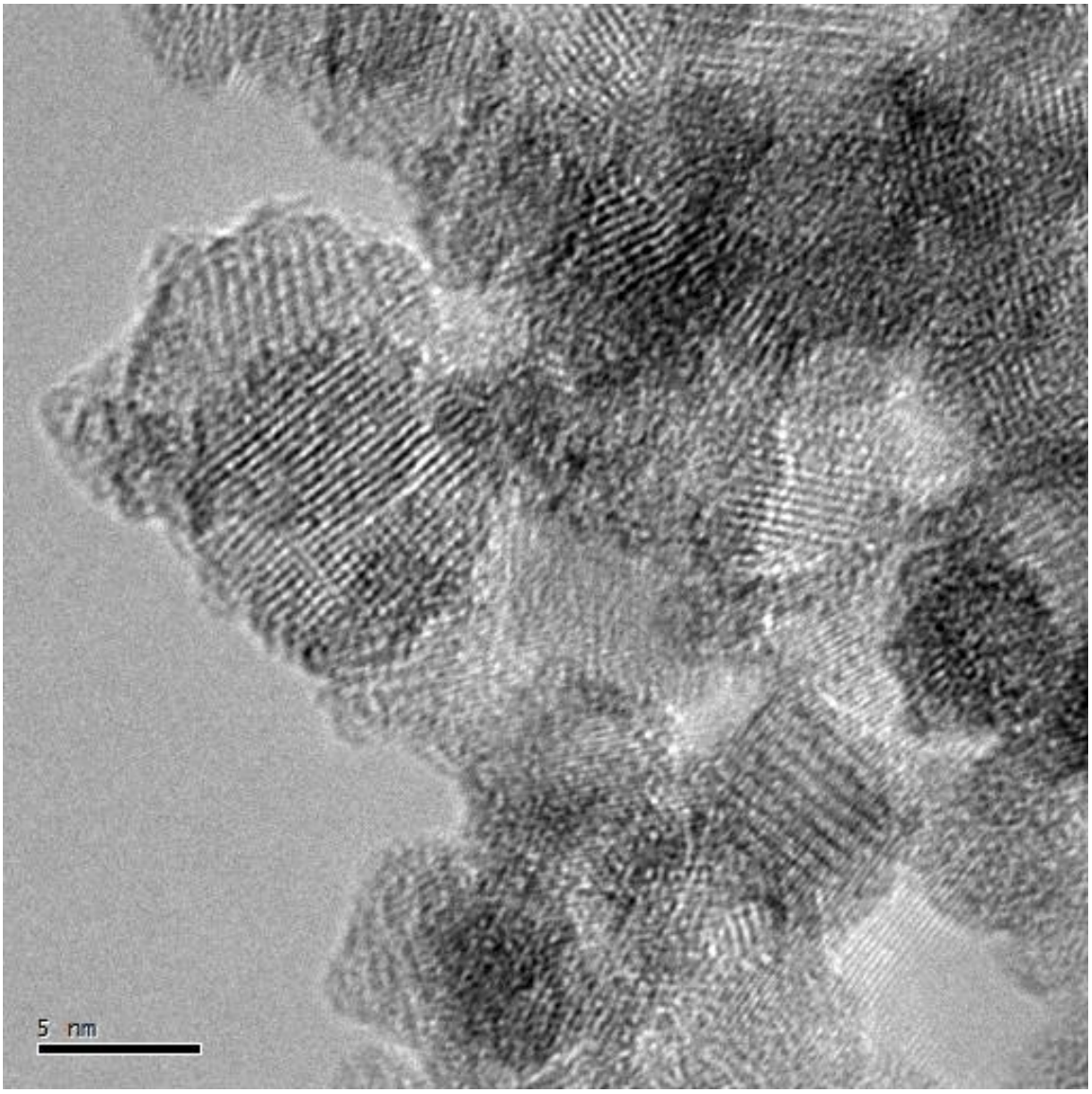

Figure 39 Ta150 HR TEM image

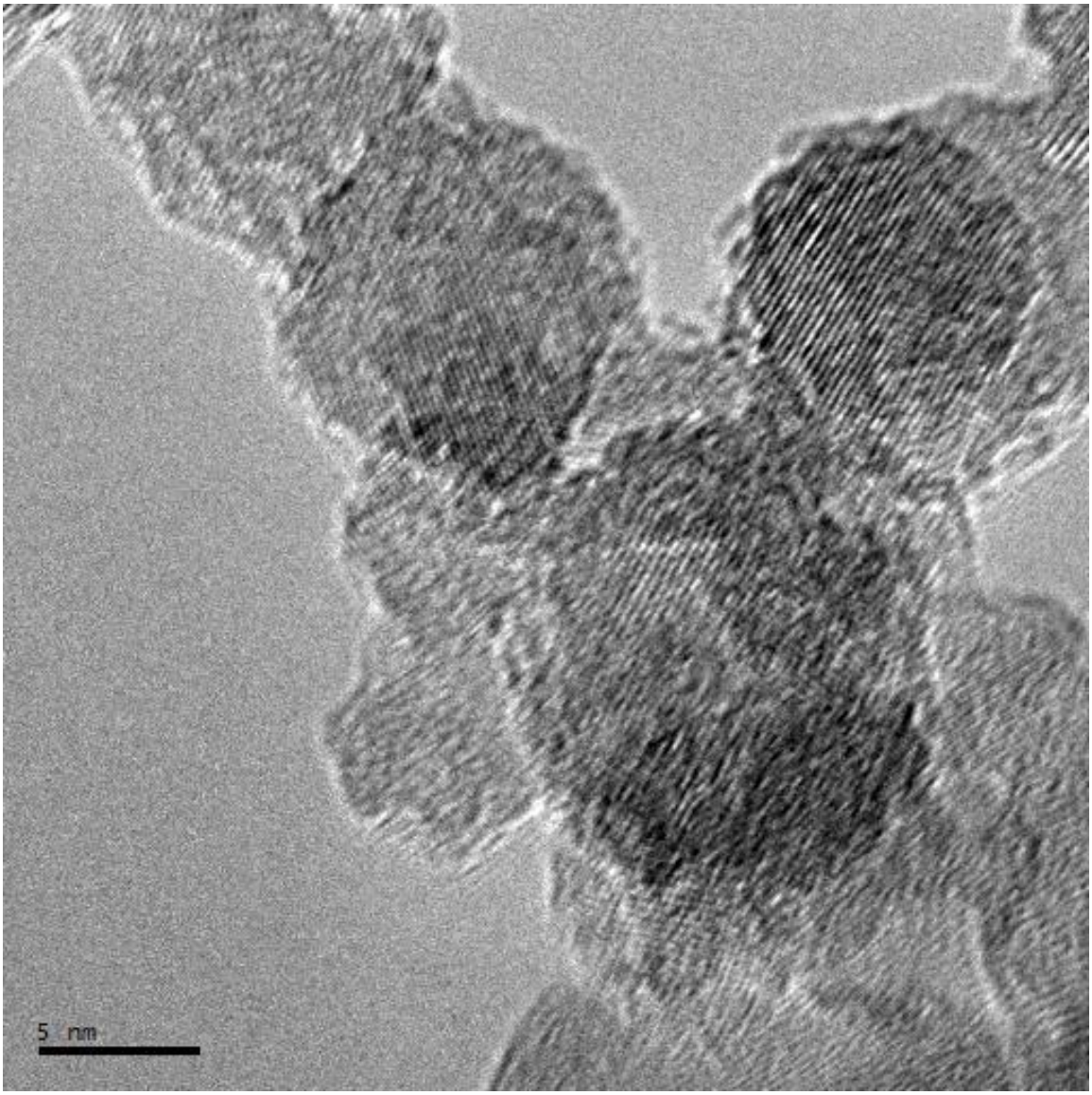

Figure 40 HRTEM of Tb100

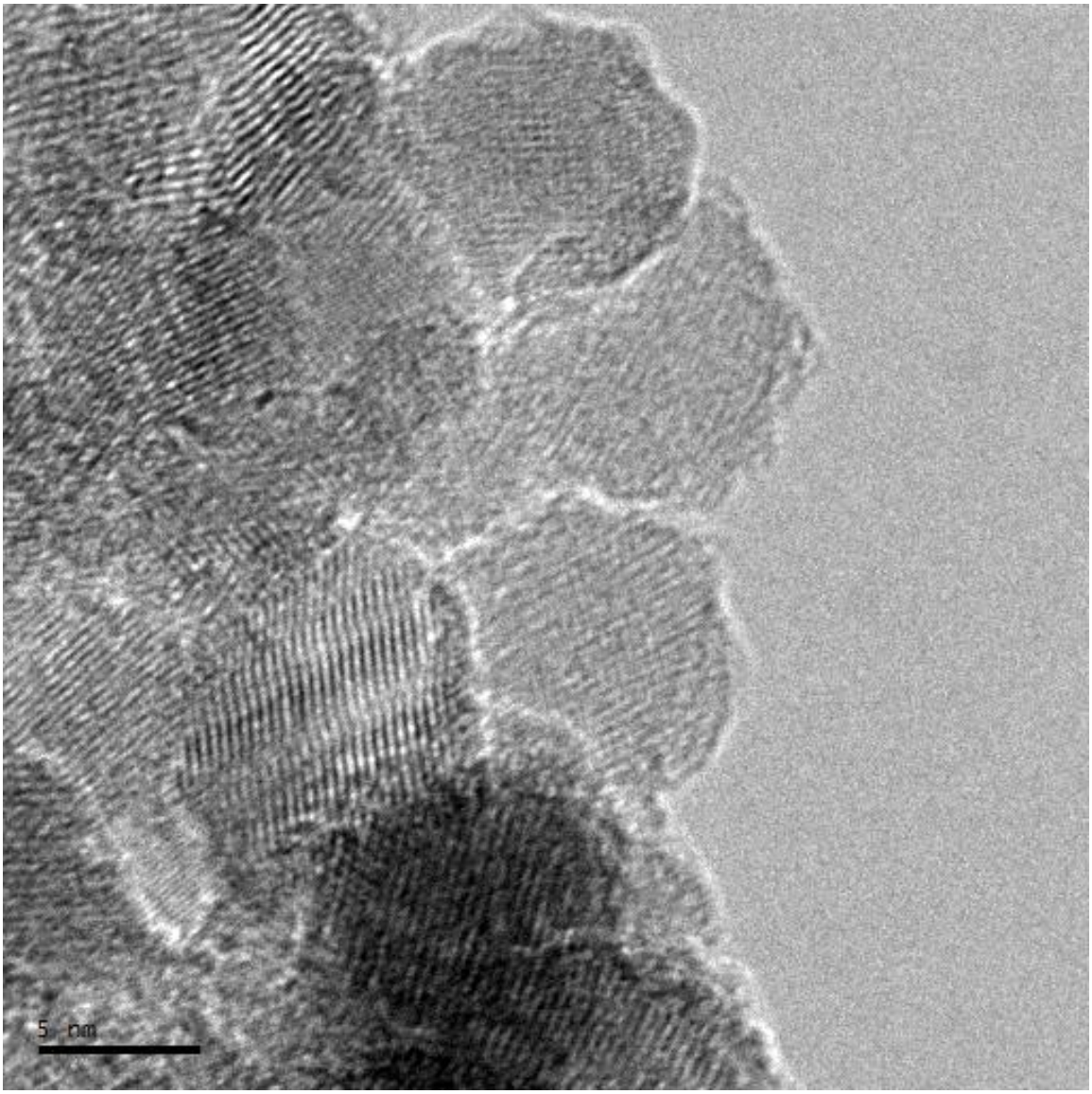

Figure 41 HRTEM of Tb150

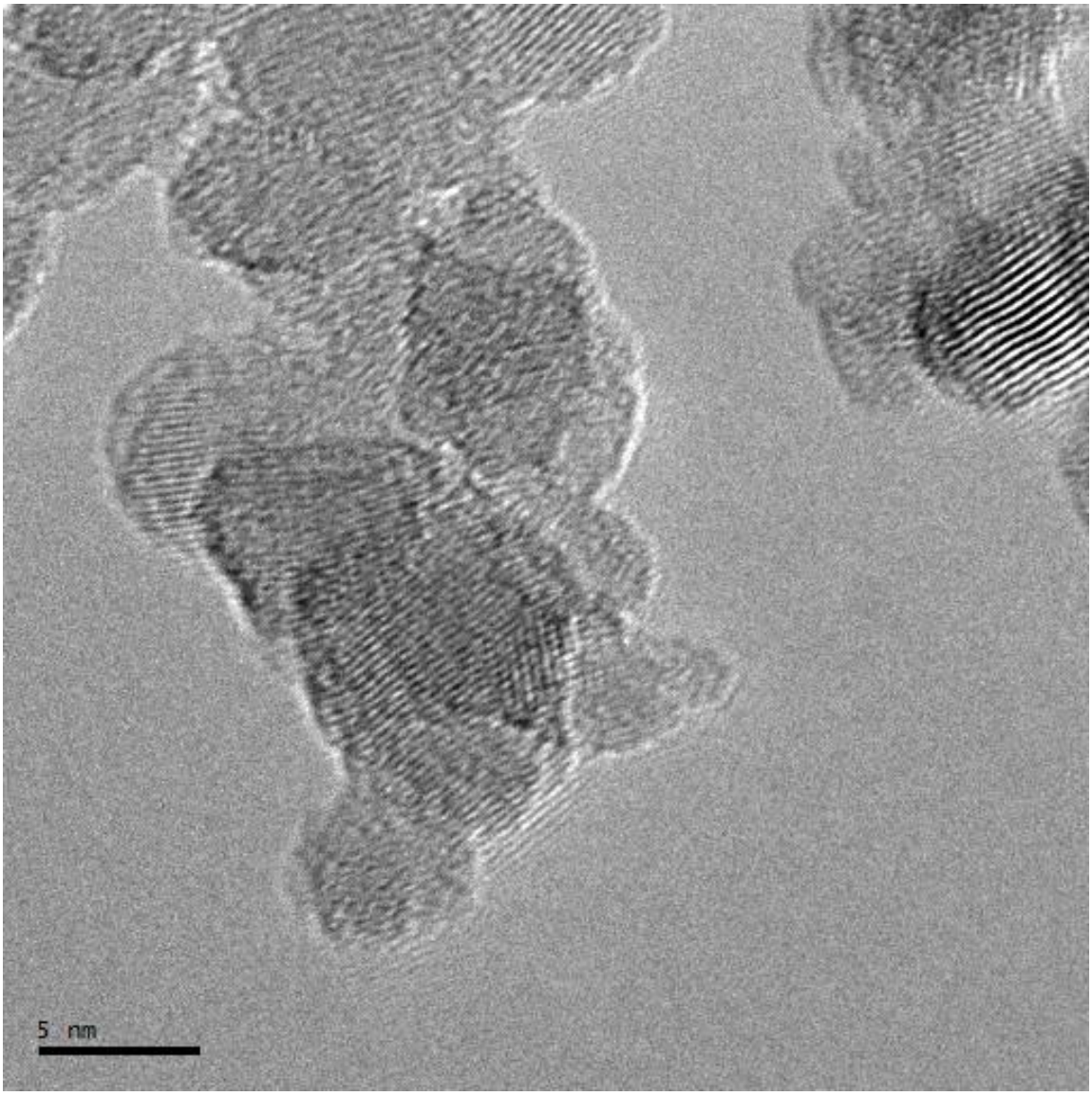

Figure 42 HRTEM of Tb250

Using TEM, the particle sizes can be seen to change from cases T-b300 to T-b100. The particle size increases from 3.72 to 9.11nm as the flow velocity issuing form the burner decreases. The particle size changes and the carbon concentration changes are summarized in the table below.

Sample Name	Average Particle Size [nm]	Standard Deviation [nm]	XPS Carbon Atomic % [C%]	Temperature [K]
T-b100	9.11	2.06		2060
T-b150	8.60	1.92	28.52%	2120
T-b200	6.22	1.72		2180
T-b250	5.15	1.12	22.05%	2230
T-b300	3.72	.787		2280

Table 1 Tb series average particle size, standard deviation, XPS carbon concentration and Spin maximum temperatures

Another characteristic of the as-produced powders that is studied is their thermal stability. Ta150, Tb150, and Tb250 are heated in a furnace at 230ºC for 24 hours. Samples become brown color upon heating.

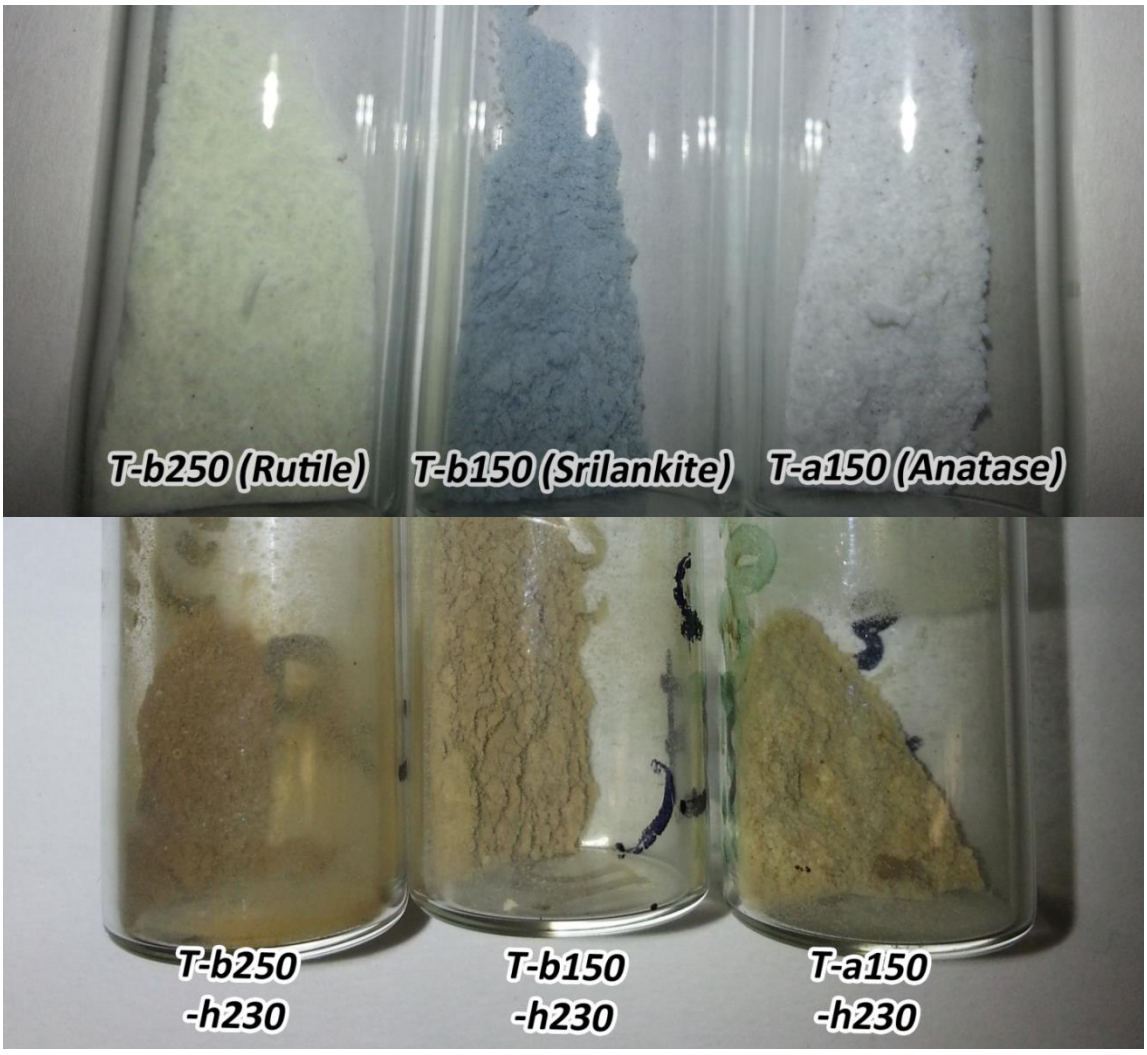

Figure 43 Optical image of non heated Tb250, Tb150, and Ta150 (top); compare to the heated at 230^{o}C (bottom)

Next, the samples' thermal stability are analyzed with thermal gravimetric analysis (TGA) and digital scanning calorimetry (DSC). As shown in the Figure 16, Figure 17, and Figure 18, the samples do not show any phase change peaks, indicating phase stability. Two endothermic peaks occur at approximately 100ºC and 250ºC. The 100ºC peak corresponds to the release of water absorbed from the product of combustion, while the 250ºC is hypothesized to be from un-decomposed precursor. This hypothesis stems from the endothermic peak from the DSC of TTIP decomposition at 278 ºC. From the

DSC curve, it makes sense to heat treat our sample at 230ºC, thus creating a thermally inert ceramic. Performing our heat treatment in the furnace for 24 hours at 230ºC indicates a thermally inert DSC thermal history.

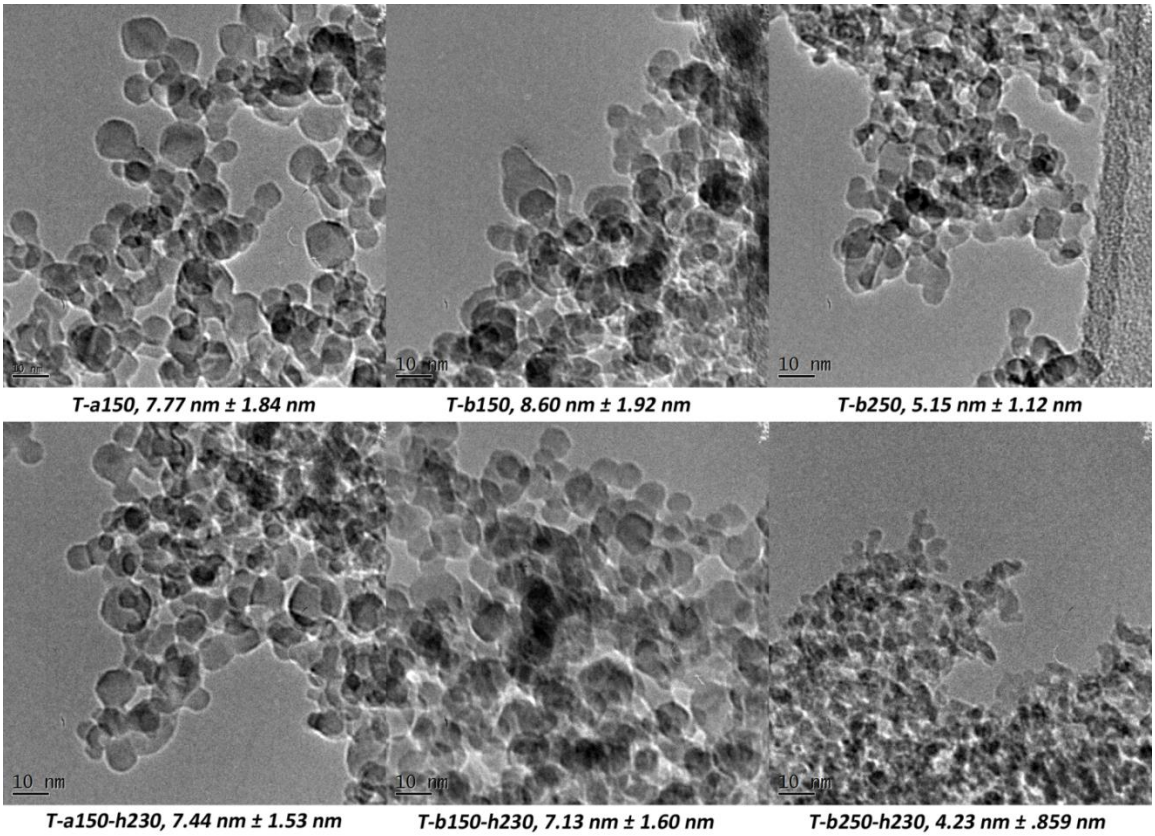

Figure 44 TEM pictures of Ta150, Tb150, Tb250 heated and non heated

From the TEM, particle size reduction can be observed upon heating. Consistent with the DSC & TGA signature, there are no phase changes upon heating. Conversely, looking at the XPS carbon concentration, a consistent reduction in the carbon concentration upon heating is observed. Meanwhile, from the SAED, the phase does not change upon heating, in agreement with the DSC.

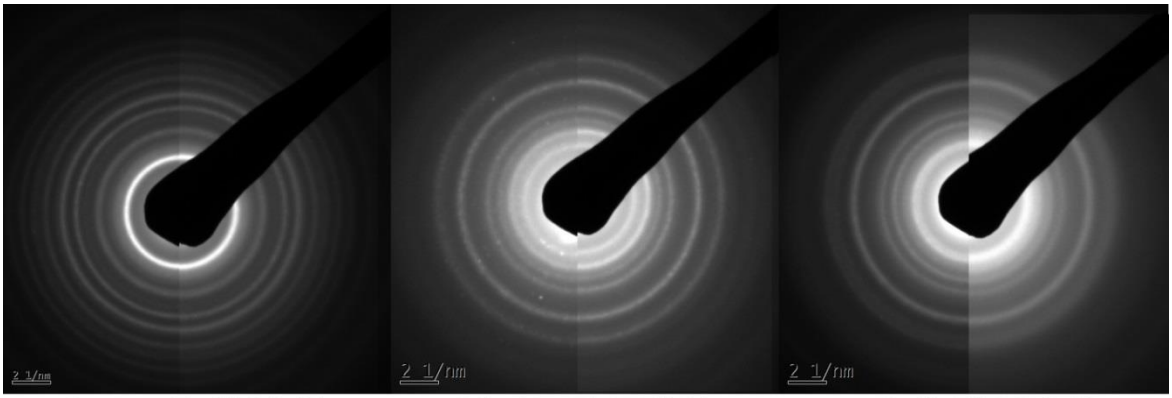

Figure 45 TEM SAED of heated and non heated couterpart - indicating no phase change detected post heated

Sample Name	Average Particle Size [nm]	Standard Deviation [nm]	XPS Carbon Atomic % [C%]	Temperature [K]
T-a150	7.77	1.84	28.04	1560
T-a150-h230	7.44	1.53	22.37	
T-b150	8.60	1.92	23.50	2120
T-b150-h230	7.13	1.60	19.47	
T-b250	5.15	1.12	28.66	2230
T-b250-h230	4.23	.859	24.26	

Table 2 Particle size, XPS carbon concentration and temperature of flame for heated and unheated sample.

From this set of studies, the addition of ethylene into the hydrogen flame induces phase transformation from anatase-rutile to srilankite-rutile for the nanopowders.

4.1.2 Tc series – change of velocity

Tb cases are designed to preserve the stoichiometry, while varying the flow velocity issuing from the burner. This, however, has the consequence of affecting the temperature and residence time. The intention of these cases is primarily to observe the phase changes between rutile to srilankite and the possibility to capture such phenomena by simply changing the velocity of the flow.

The Tc series is designed with the intention to introduce carbon dopant with lower hydrogen to ethylene ratio, while minimizing the temperature differences between the cases. The hydrogen to ethylene ratio is lowered from 1:1 to 1:0.4. Assuming that nitrogen is inert and does not contribute to the reaction, strategic-dilution with nitrogen can keep the temperature constant. For the T-c series, the temperatures are targeted at approximately 2050K.

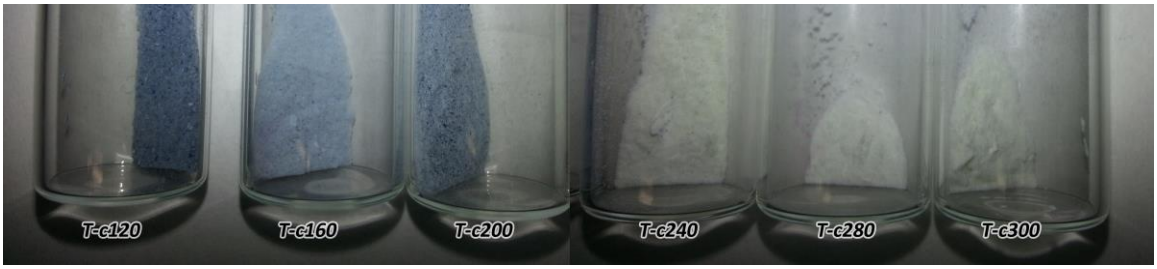

Figure 46 Physical Apearances of the Tc series

As evidenced from the physical appearances, visible absorption changes are noticeable, indicating successful carbon doping. From the XPS measurments, our system is able to control the carbon doping, along the 2050K isotherm. The trend is if the velocity of the flow is lower, the carbon doping will be higher. Thus, along an isotherm, the carbon dopant within the titania matrix can be controlled.

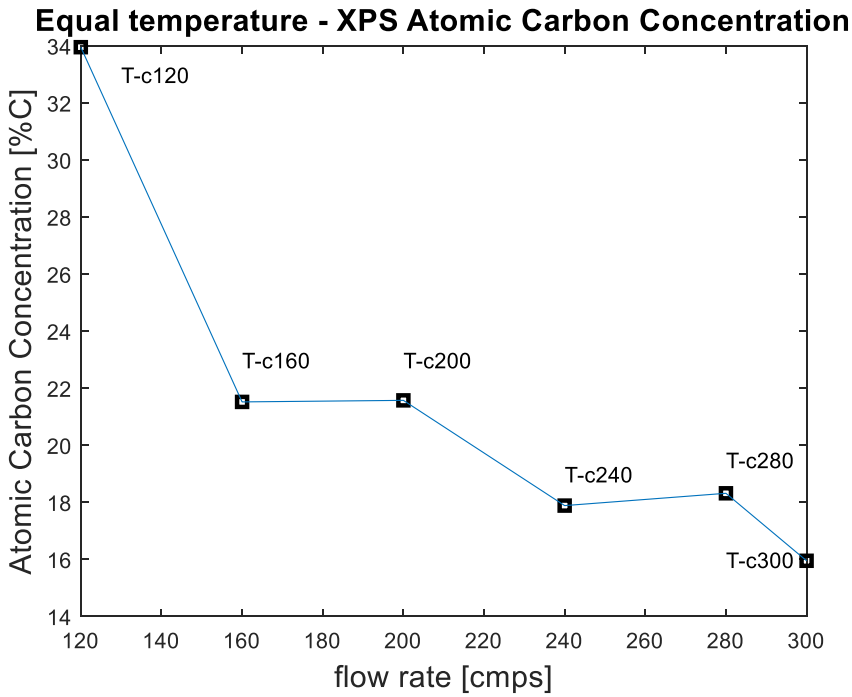

Figure 47 XPS carbon concentration plot of the T-c series, indicating lower carbon concentration as the velocity increase.

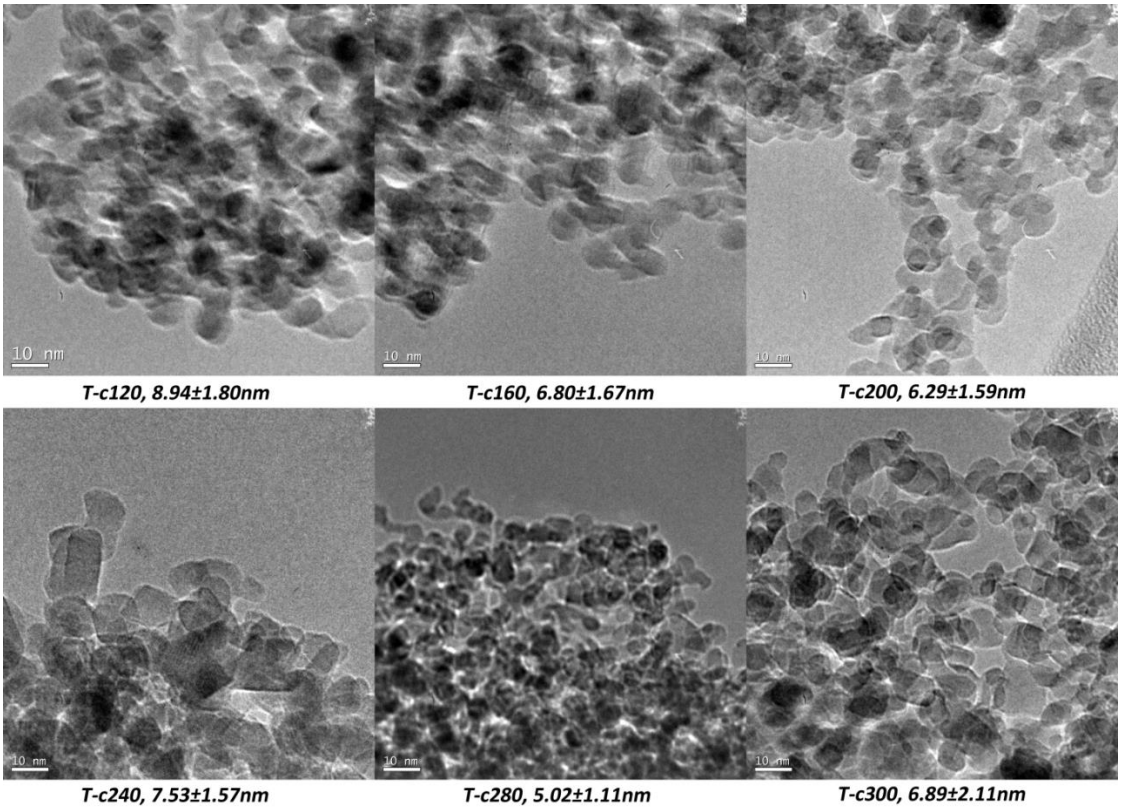

Figure 48 TEM pictures of Tc series, Tc120, 160, 200, 240, 280, 300

Sample Name	Average Particle Size [nm]	Standard Deviation [nm]	XPS Carbon Atomic % [C%]	Temperature [K]
T-c120	8.94	1.80	33.95	2150
T-c160	6.40	1.67	21.52	2150
T-c200	6.29	1.59	21.57	2150
T-c240	7.53	1.57	17.89	2150
T-c280	5.02	1.11	18.32	2150
T-c300	6.89	2.11	15.95	2150

Table 3 Particle size, XPS carbon concentration and Temperature of the flame of the T-c series.

From analyzing the crystallinity of the samples with SAED, the primary phases are dominated by rutile. The temperature in the Tc series is relatively close to that of the Tb150 and Tb200 cases. However, the srilankite phases are barely existent in these series. As evidenced from the SAED profile, at 1:0.4 ratio of H_2 to C_2H_4, the srilankite phases are not dominant in this situation.

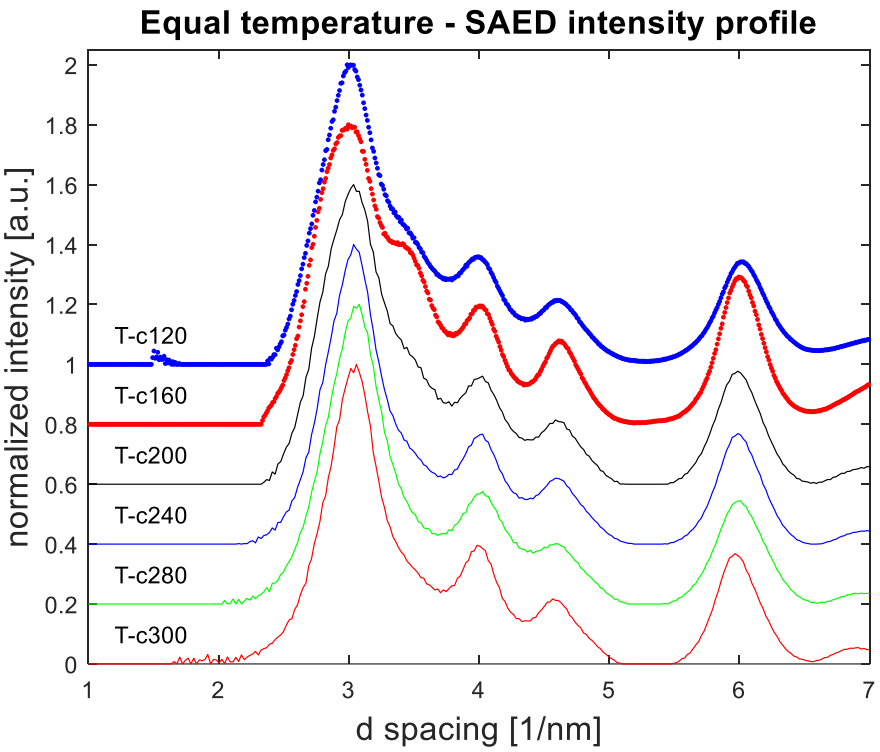

Figure 49 SAED intensity profile of the T-c series, showing mostly Rutile dominant phase.

However, the range of carbon-doped concentrations in the titania is not significantly higher compared to that for the 1:1 ratio for hydrogen to ethylene. Assuming the type of carbon doping that exists from 1:1 and 1:0.4 ratios of hydrogen/ethylene are of the same type, one can conclude that the carbon concentration might not be the primary factor that determines the srilankite formation. However, one cannot be sure if the ratio of the hydrogen/ethylene does not play a role in the srilankite nucleation. Although this aspect poses one additional parameter that needs to be analyzed, it also demonstrates the possibility to control the carbon concentration along an isotherm.

Note that Tb150 and Tc120 both have the dark blue appearance, but different phases. As such, color is not a good marker for phase in our samples, emphasizing the need for crystallinity measurement.

4.1.3 Te – series – change of temperature

The next set of experiments is the Te series. The maximum flow-field temperature is now raised to 2650K by complete elimination of nitrogen in the gas phase. This increase in temperature yields additional rutile phase. From here, temperature change is able to move the rutile-srilankite equilibrium, but not enough to move into the anatase-rutile regime.

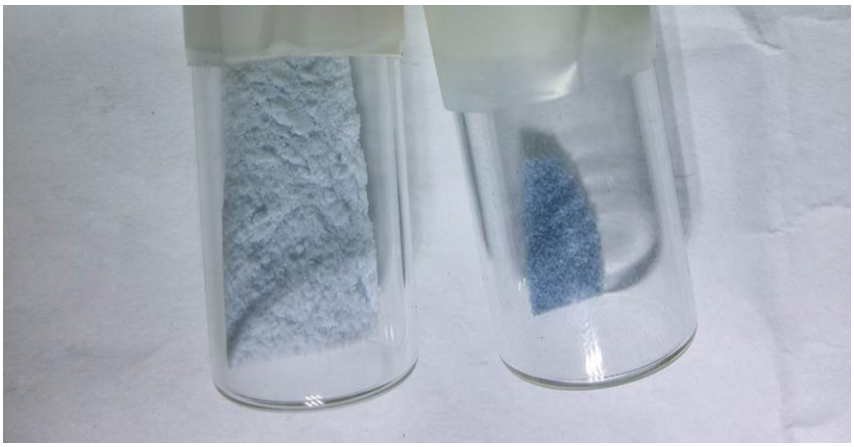

Figure 50 Te_N2_0 physical appearances, from left to right, center and edge collection area.

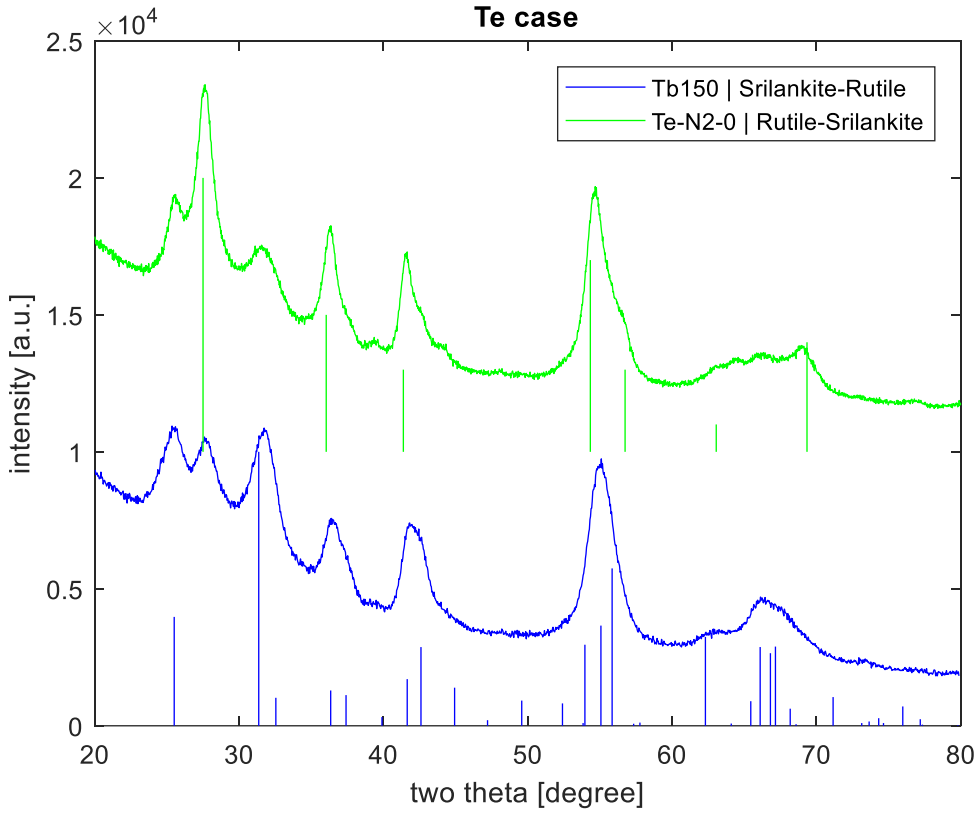

Figure 51 XRD of Te cases, compare to Tb150

4.1.3.1 Cold srilankite vs hot anatase comparison*

Another subset of this Te series is the cold srilankite case (Tb100_N11). The goal of this experiment is to reduce the temperature of the flame to be comparable to that of the Ta150 case, as shown in Figure 5. Consistent to the conclusion of the Te series, variation of temperature from 1560K to 2650K yields samples that are still srilankite – rutile mix.

* XRD of Tb100_N11 and Ta200_N0 are used in this thesis with permission from Ashley Pennington, Jonathan Shi, Rachel A. Yang and Prof. Celik.

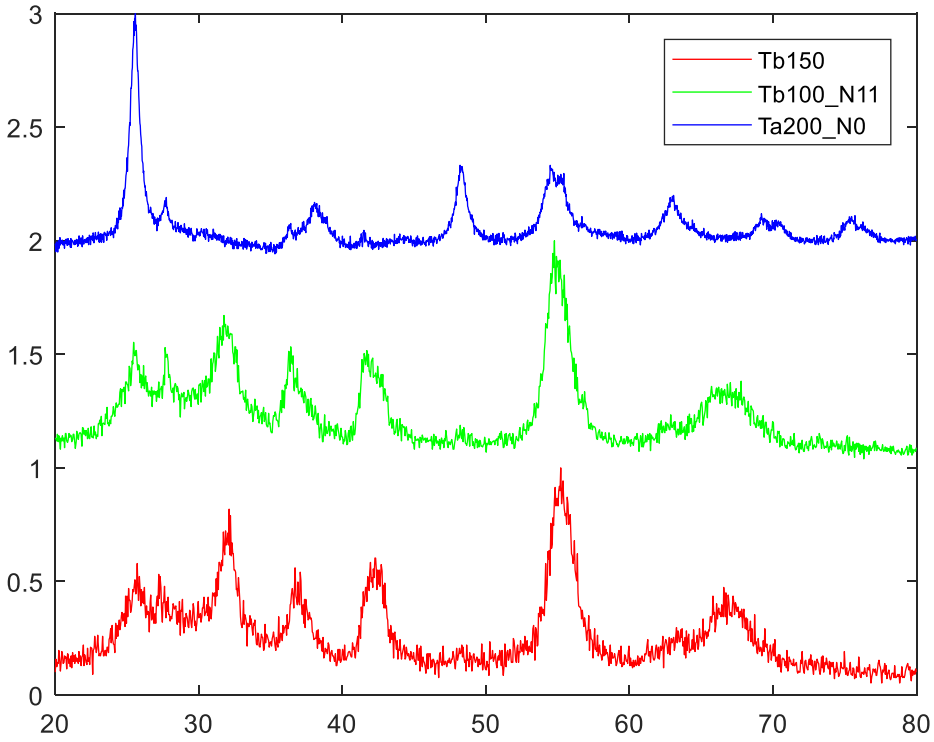

Figure 52 Normalized XRD spectra of Tb150, Tb100_N11, Ta200_N0

4.1.4 Tg – change of pressure from 20-40 torr

Another parameter that is modified is the ambient pressure. By changing the ambient pressure from 20torr to 40torr, XRD spectra reveals more amorphous product. The phase observed is still a mix of srilankite-rutile, thus the increase in ambient pressure is also able to modify the srilankite-rutile equilibrium, but not enough to move it into the anatase-rutile regime.

Figure 53 Tg 40 torr physical appearance, left to right indicate center and edge collection area.

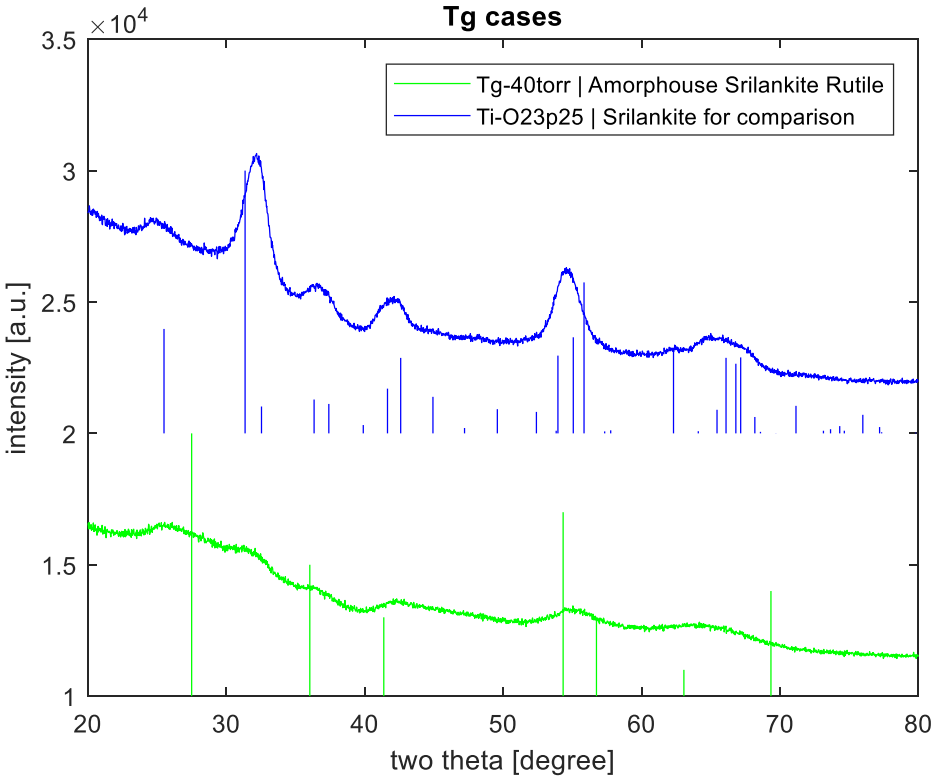

Figure 54 XRD of Tg cases, compared to Ti O2 3p25

4.2 Parametric study that influence Anatase-Rutile-Srilankite transition

So far, it has been observed that by modifying parameters such as velocity, temperature, and pressure, srilankite and rutile composition are observed. In the Th and Ti series, by modifying the oxygen concentration, the srilankite-rutile phase can transition to the anatase-rutile phase.

4.2.1 Ti – Fuel rich

Ti series are identified by fuel-rich condition. Keep in mind that as the flame condition approaches the flammability limits, so does flame stability. Ti_O2_3p25 is the lowest oxygen concentration that is possible with this setup; this corresponds to an equivalence ratio of 1.08. The powder quantity generated in this case are less than that compared to its Tb150 counterpart. Nevertheless, the repeatability of this case can be demonstrated by multiple runs of these experiments. From the TEM picture, this sample is found to be crystalline, as evident from the diffraction lines. SAED of this sample is compared to that in the next section in Figure 60.

Figure 55 Ti O2 3p25 physical appearance

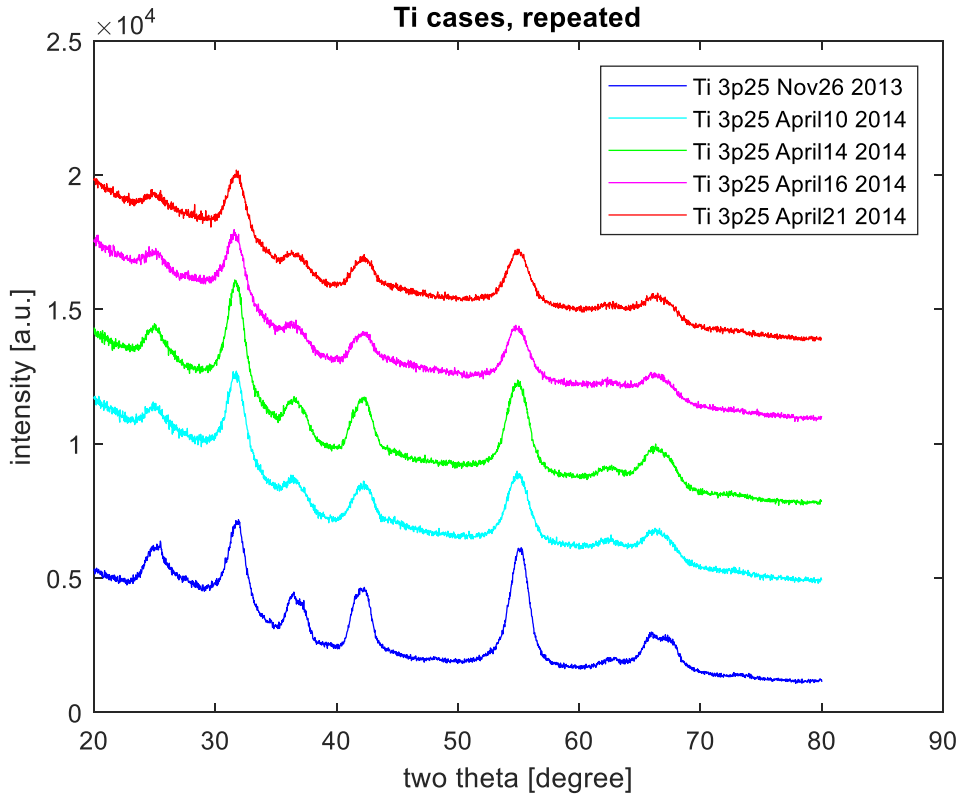

Figure 56 XRD Ti O2 3p25

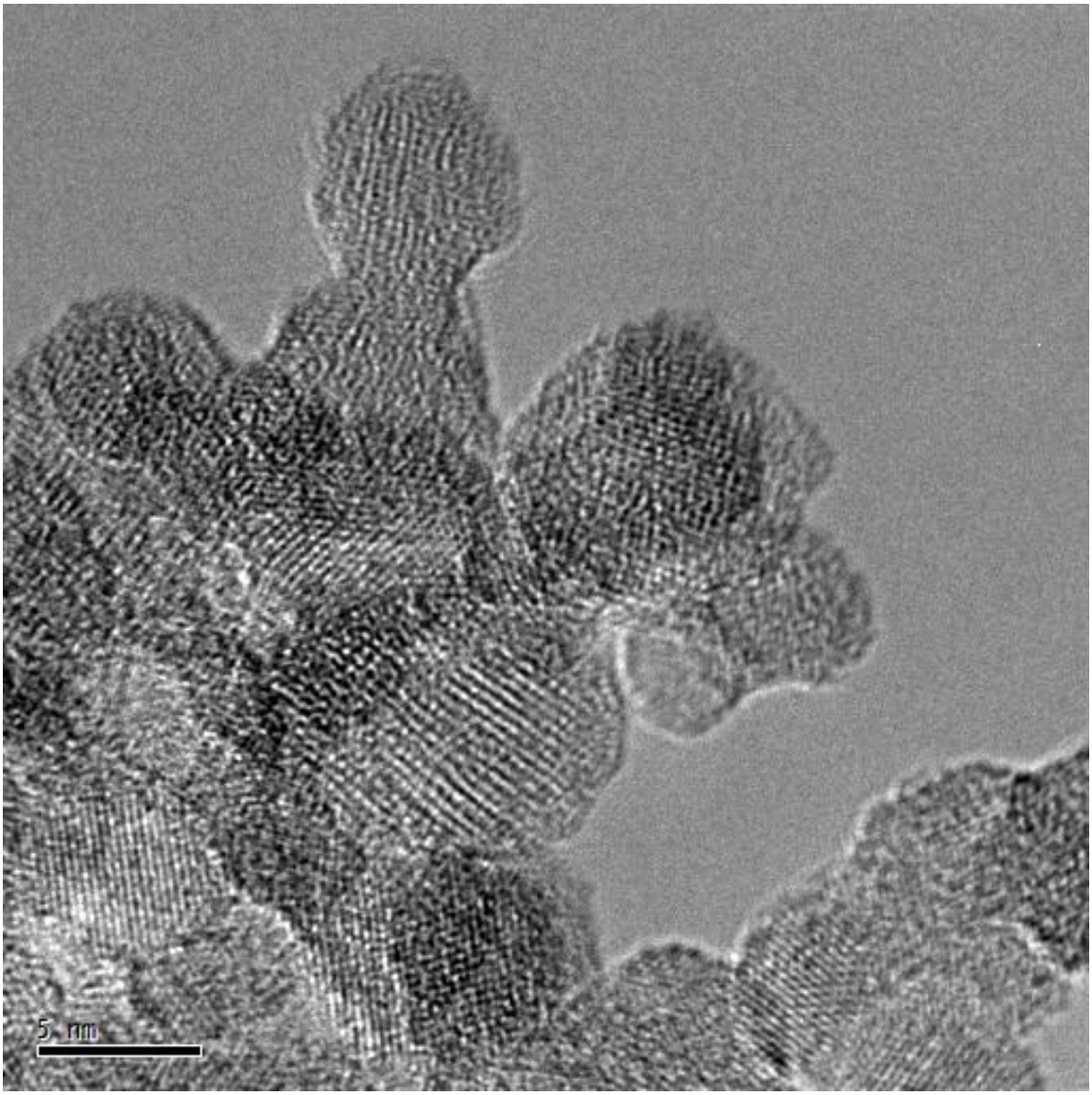

Figure 57 HRTEM Ti_O2_9p5 (500kx)

4.2.2 Th series – fuel lean

Th series are identified by fuel lean condition. In this condition, it is possible to increase the Oxygen ratio to as high as 9p5. By increasing the Oxygen concentration, the samples color slowly shift from light blue toward white. From the TEM, this sample is fully crystalline, as evident from the diffraction lines in both the TEM image and SAED.

Notice that by changing the oxygen concentration, the composition of the samples are modified with the following progression.

- Srilankite (Ti, O=3.25) ; equivalence ratio = 1.08
- Srilankite with trace of Rutile (Tb150, O=3.5) ; equivalence ratio = 1
- Rutile with trace of Srilankite (Th, O=4.5) ; equivalence ratio = 0.78
- Rutile with trace of Anatase (Th, O=5.5) ; equivalence ratio = 0.64
- Anatase (Th, O=9.5) ; equivalence ratio = 0.37

Figure 58 Ti series physical appearance. Th O2 4p5, 5p0, 5p5, 6p5, p5, 9p5 (from top left to right, bottom left to right)

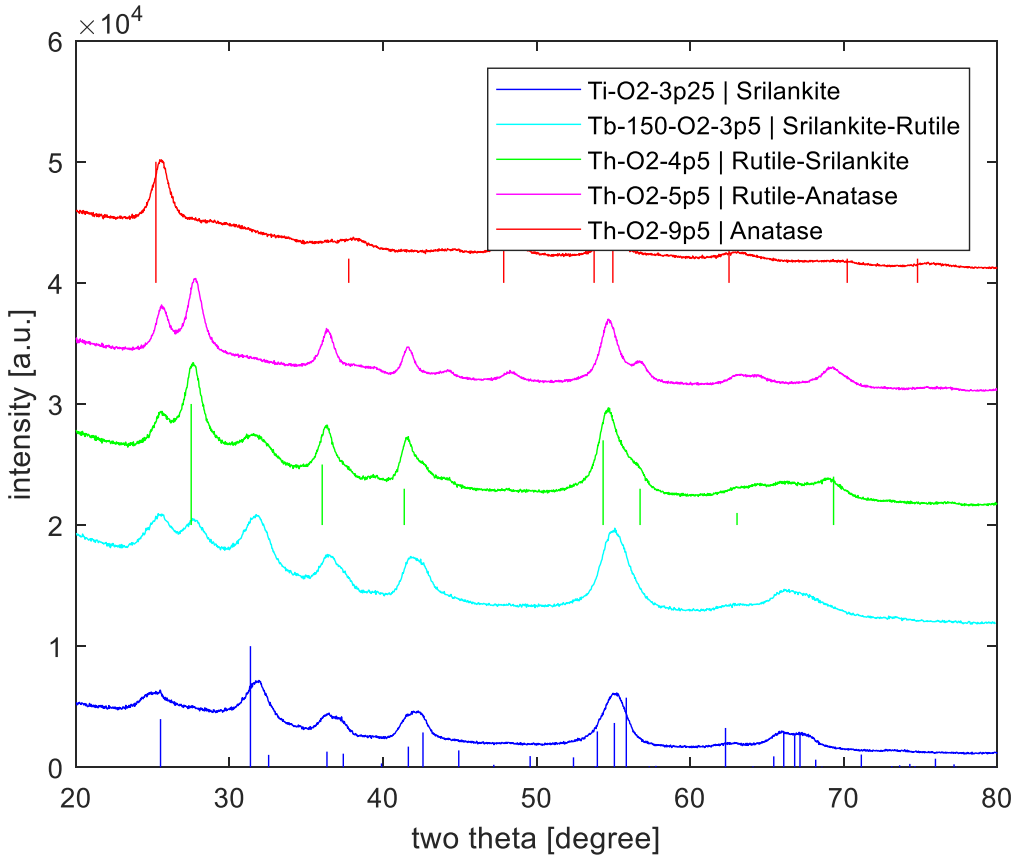

Figure 59 XRD of Ti O2 3p25, Tb150, Th O2 4p5, 5p5, 9p5. Indicating phase changes from Srilankite, Srilankite-Rutile, Rutile-Srilankite, Rutile-Anatase, Anatase

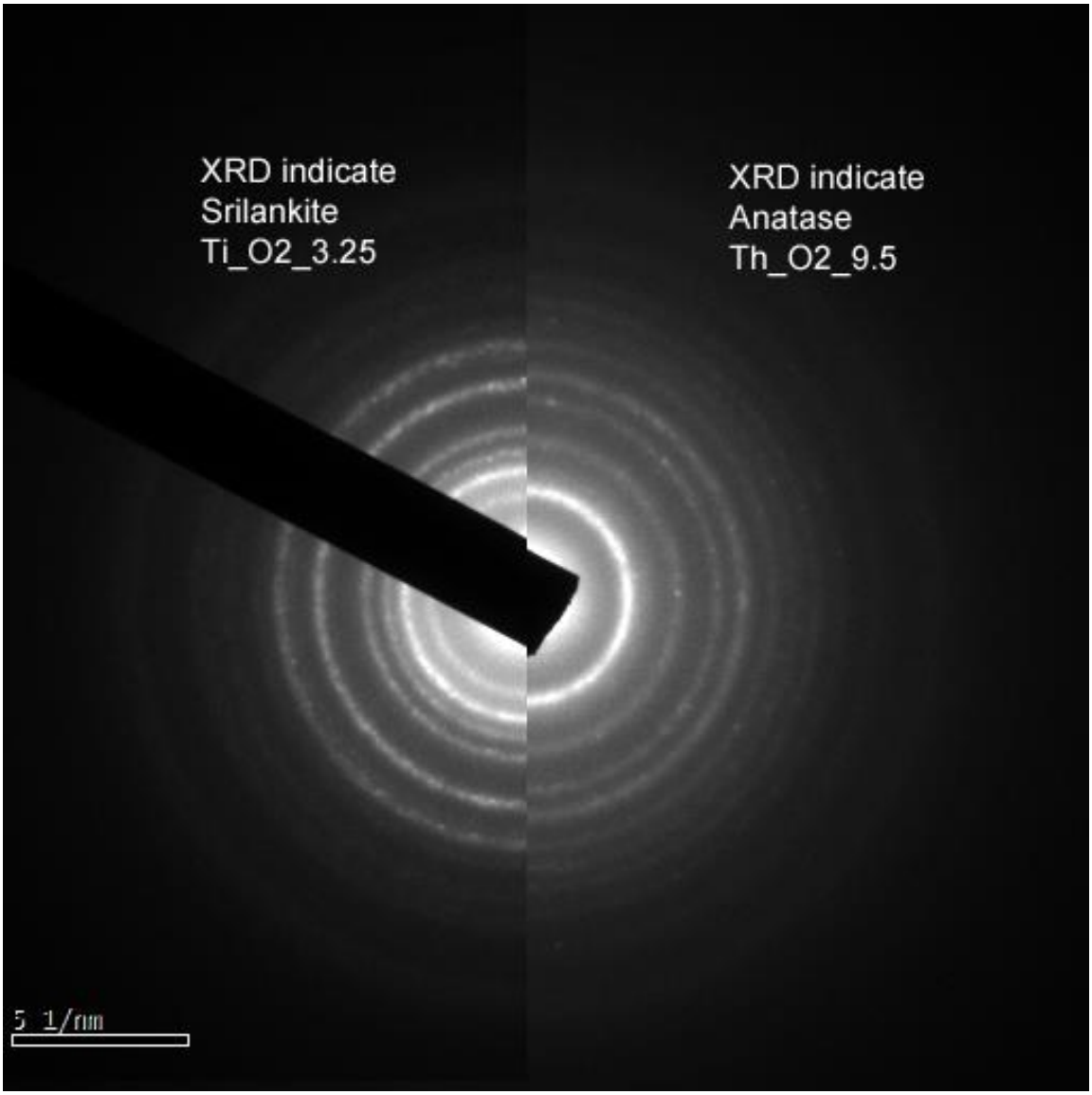

Figure 60 Ti_O2_9p5 and Ti_O2_3p25 TEM SAED

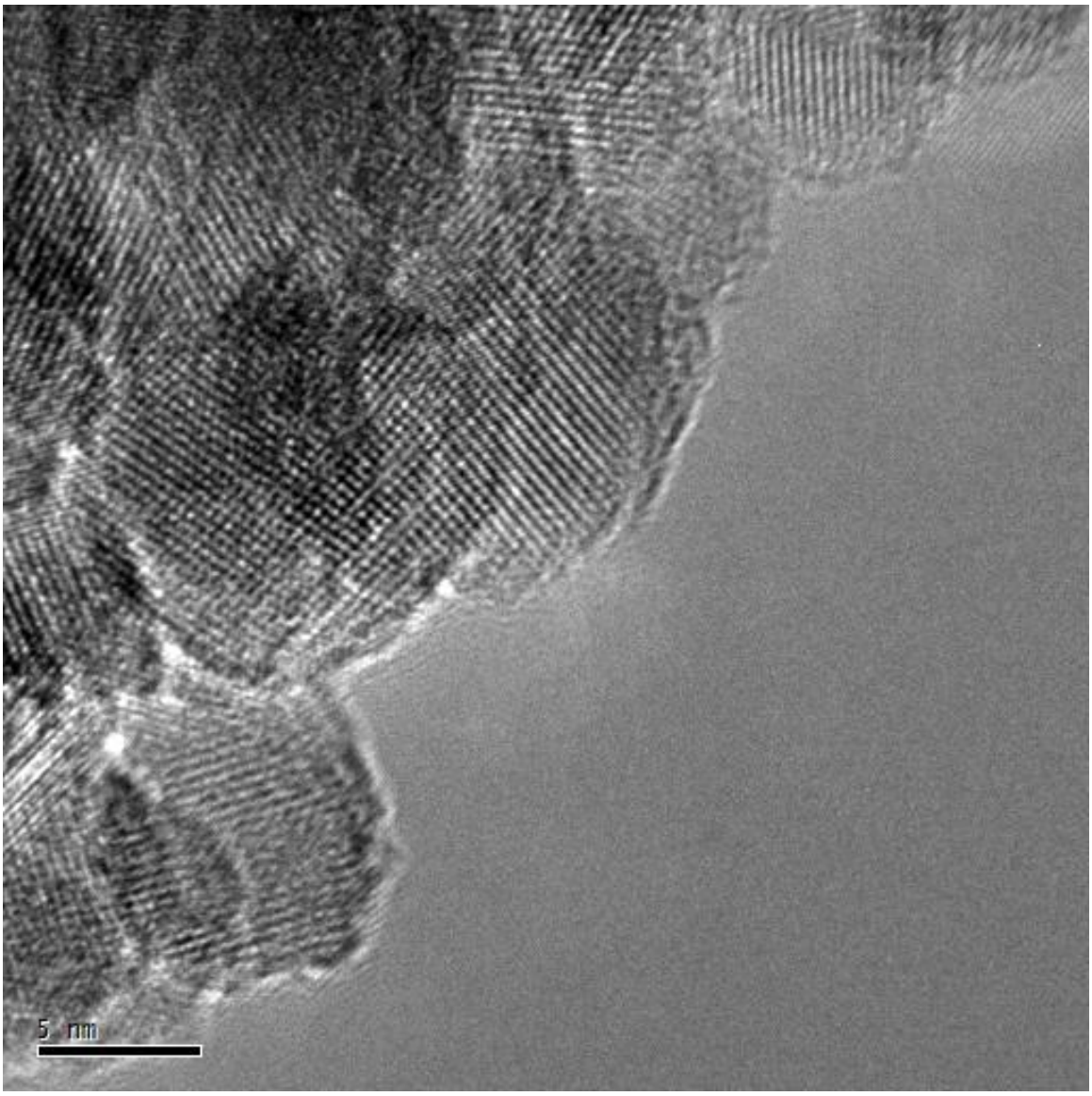

Figure 61 Th O2 9p5 HRTEM (500kx)

4.3 Conclusions

The investigation of ethylene gas to hydrogen-based flame is conducted. While the hydrogen-only flame generated an anatase-rutile mix, ethylene introduction resulted in the transition to the srilankite-rutile system. It is established that temperature variation from 1560K to 2650K, ambient pressure from 20 to 40 torr, and burner flow velocity

from 150 to 300 cm/s maintain the production of nanopowders with srilankite-rutile composition.

On the other hand, by modifying the oxygen concentration, the composition from anatase (fuel lean) shifts toward srilankite (fuel rich). Rutile exists as a phase found in-between the anatase and srilankite transition.

5 Concluding Remarks

Low-pressure premixed hydrogen/ethylene/oxygen flame with TTIP as precursor is used to produce titania nanoparticles. The Sandia SPIN code allows modeling of the flame structure and flow-field attributes, assisting in designing the parametric studies to isolate the effect of each variable on as-synthesized nanopowder characteristics.

As Ethylene is introduced to the hydrogen/oxygen flame, the resulting powders shift from an anatase-rutile mix to a srilankite-rutile mix. Several parametric studies are conducted that establishes that temperature variation from 1560K to 2650K, ambient pressure from 20 to 40 torr, and issuing flow velocity from 150 to 300 cm/s still produce srilankite-rutile composition. The trend observed is that the higher the temperature and the higher the velocity, the more rutile phase is produced. Higher pressure yields more amorphous rutile composition.

On the other hand, by modifying the oxygen concentration, the composition from anatase (Fuel lean) tilts toward srilankite (Fuel rich). Rutile exists in-between the Anatase and Srilankite transition.

This study demonstrates that by modifying the composition of the precursor (e.g. by adding ethylene), one can modify the phase of the product, e.g. producing the srilankite phase even at lower temperatures, showing that carbon doping indeed stabilizes the high-pressure phase.

5.1 Suggestion for future works

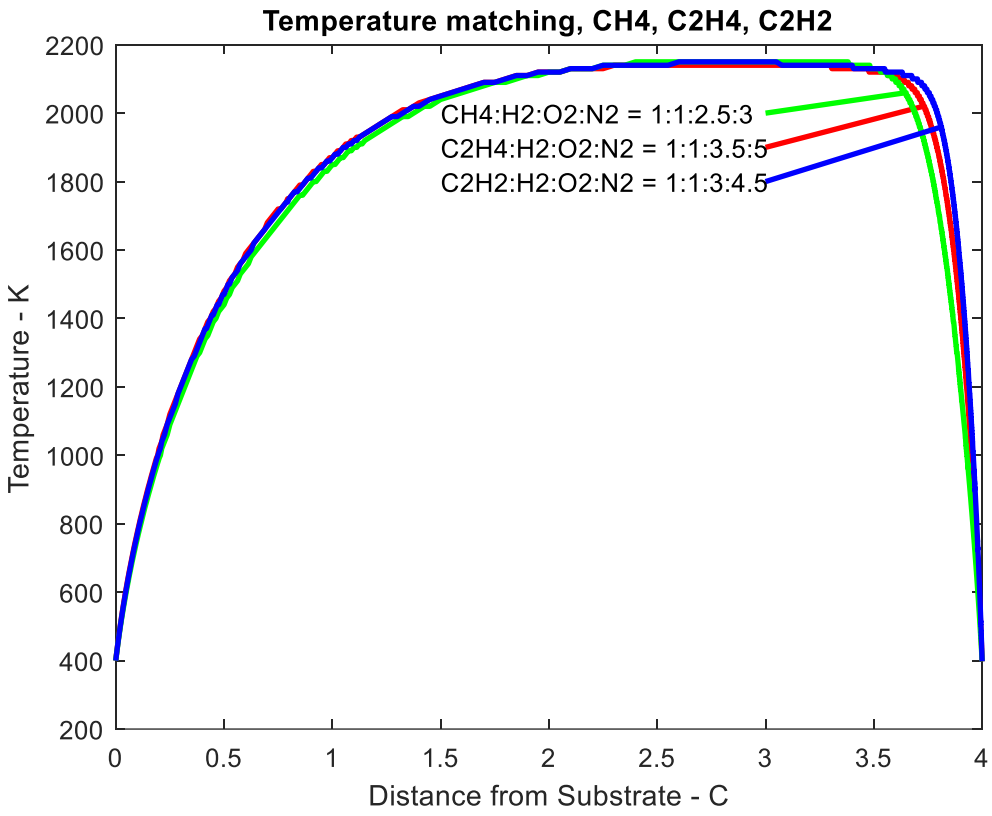

Figure 62 SPIN simulation result of Methane and Acetylene flame that match temperature profile of Tb150

Ethylene is but one gas that can be added into the flame to modify the composition of the as-synthesized powders. Carbon-based fuel such as methane and acetylene can be used as well. Potential direction may be to conduct parametric study using methane and acetylene to observe the effect of polycyclic-aromatic hydrocarbons (PAHs) on carbon doping of the nanopowders for the srilankite-rutile phase being produced.

6 References

1 Freestone, I., Meeks, N., Sax, M. & Higgitt, C. The Lycurgus Cup — A Roman Nanotechnology. *Gold Bull* **40**, 270-277, doi:https://doi.org/10.1007/BF03215599 (2007).

2 Reibold, M. *et al.* Materials: Carbon Nanotubes In An Ancient Damascus Sabre. *Nature* **444**, 286, doi:doi:10.1038/444286a (2006).

3 O'Regan, B. & Graetzel, M. A Low-Cost, High-Efficiency Solar Cell Based On Dye-Sensitized Colloidal Titanium Dioxide Films. *Nature* **353**, 737-740 (1991).

4 Chang, H. *et al.* Photodecomposition And Surface Adsorption Of Methylene Blue On TiO2 Nanofluid Prepared By ASNSS. *Materials Transactions* **45**, 3334-3337, doi:http://doi.org/10.2320/matertrans.45.3334 (2004).

5 Irie, H., Washizuka, S. & Hashimoto, K. Hydrophilicity On Carbon-Doped TiO2 Thin Films Under Visible Light. *Thin Solid Films* **510**, 21-25, doi:https://doi.org/10.1016/j.tsf.2005.08.374 (2006).

6 Inc., B. Birdair, Inc.'S TiO2 Coated Tensile Fabric Membrane Arrives In North American Custom Architectural Roofing Market. *www.birdair.com*, doi:http://www.birdair.com/sites/default/files/press-releases/2007-07-12_Birdair_TiO2.pdf (2007).

7 B.Ohtani, O.O.Prieto-Mahaney, D.Li & R.Abe. What Is Degussa (Evonik) P25? Crystalline Composition Analysis, Reconstruction From Isolated Pure Particles And Photocatalytic Activity Test. *Journal Of Photochemistry And Photobiology A: Chemistry* **216**, 179-182, doi:https://doi.org/10.1016/j.jphotochem.2010.07.024 (2010).

8 Hu, J., Qin, H., Sui, Z. & Lu, H. Characteristic Of Mechanically Milled TiO2 Powders. *Materials Letters* **53**, 421-424, doi:https://doi.org/10.1016/S0167-577X(01)00518-3 (2002).

9 Xie, J., Lü, X., Liu, J. & Shu, H. Brookite Titania Photocatalytic Nanomaterials: Synthesis, Properties, And Applications. *Pure Appl. Chem.* **81**, 2407–2415, doi:https://doi.org/10.1351/PAC-CON-08-11-12 (2009).

10 Zaleska, A. Doped-TiO2: A Review. *Recent Patents On Engineering* **2**, 157-164, doi:https://doi.org/10.2174/187221208786306289 (2008).

11 Valentin, C. D., Pacchioni, G. & Selloni, A. Theory Of Carbon Doping Of Titanium Dioxide. *Chem. Mater.* **17**, 6656–6665, doi:DOI: 10.1021/cm051921h (2005).

12 Robichaud, C. O., Uyar, A. E., Darby, M. R., Zucker , L. G. & Wiesner, M. R. Estimates Of Upper Bounds And Trends In Nano-TiO2 Production As A Basis For Exposure Assessment. *Environ. Sci. Technol.* **43** 4227–4233, doi:DOI: 10.1021/es8032549 (2009).

13 J. L. Murray & H. A. Wriedt. The O-Ti (Oxygen-Titanium) System. *Journal Of Phase Equilibria* **8**, 148–165, doi:https://doi.org/10.1007/BF02873201 (1987).

14 Dachille, F., Simons, P. & Roy, R. Pressure-Temperature Studies Of Anatase, Brookite, Rutile And TiO2-II. *The American Mineralogist* **53**, 1929-1939 (1968).

15 Hanaor, D. A. H. & Sorrell, C. C. Review Of The Anatase To Rutile Phase Transformation. *Journal Of Materials Science* **46**, 855–874, doi:https://doi.org/10.1007/s10853-010-5113-0 (2011).

16 Hawa, T. & Zachariah, M. R. Internal Pressure And Surface Tension Of Bare And Hydrogen Coated Silicon Nanoparticles. *The Journal Of Chemical Physics* **121**, 9043, doi:http://dx.doi.org/10.1063/1.1797073 (2004).

17 S.H.Ehrmana, S.K.Friedlander & M.R.Zachariah. Characteristics Of SiO2/TiO2 Nanocomposite Particles Formed In A Premixed Flat Flame. *Journal Of Aerosol Science* **29**, 687-706, doi:https://doi.org/10.1016/S0021-8502(97)00454-0 (1998).

18 M.Latroche, L.Brohan, R.Marchand & M.Tournoux. New Hollandite Oxides: TiO2(H) And K0.06TiO2. *Journal Of Solid State Chemistry* **81**, 78-82, doi:https://doi.org/10.1016/0022-4596(89)90204-1 (1989).

19 Sato, H. *et al.* Baddeleyite-Type High-Pressure Phase Of TiO2. *Science* **251**, 786-788, doi:DOI: 10.1126/science.251.4995.786 (1991).

20 Dubrovinsky, L. S. *et al.* The Hardest Known Oxide. *Nature* **410**, 653 (2001).

21 H.Dutta, P.Sahu, S.K.Pradhan & M.De. Microstructure characterization of polymorphic transformed ball-milled anatase TiO2 by Rietveld method. *Materials Chemistry and Physics* **77**, 153-164, doi:https://doi.org/10.1016/S0254-0584(01)00600-9 (2003).

22 Nie, X., Zhuo, S., Maeng, G. & Sohlberg, K. Doping of TiO2 Polymorphs for Altered Optical and Photocatalytic Properties. *International Journal of Photoenergy* **Article ID 294042**, 22, doi:doi:10.1155/2009/294042 (2009).

23 Lu, X. *et al.* Enhanced Electron Transport In Nb-Doped TiO2 Nanoparticles Via Pressure-Induced Phase Transitions. *J. Am. Chem. Soc.* **136** 419–426, doi:DOI: 10.1021/ja410810w (2014).

24 Zhu, T. & Gao, S.-P. The Stability, Electronic Structure, and Optical Property of TiO2 Polymorphs. *J. Phys. Chem. C* **118**, 11385-11396, doi:DOI: 10.1021/jp412462m (2014).

25 Gribb, A. & Banfield, J. Particle Size Effects On Transformation Kinetics And Phase Stability In Nanocrystalline TiO2. *American Mineralogist* **82**, 717-728, doi:https://doi.org/10.2138/am-1997-7-809 (1997).

26 Zhang, H. & Banfield, J. F. Understanding Polymorphic Phase Transformation Behavior During Growth Of Nanocrystalline Aggregates:? Insights From TiO2. *J. Phys. Chem. B* **104** 3481–3487, doi:DOI: 10.1021/jp000499j (2000).

27 Ushakov, A. V., Karpov, I. V. & Lepeshev, A. A. Influence of the oxygen concentration on the formation of crystalline phases of TiO2 during the low-pressure arc-discharge plasma synthesis. *Physics of Nanostructures* **61**, 260-264, doi:https://doi.org/10.1134/S1063784216020262 (2016).

28 A.V.Uschakov, I.V.Karpov, A.A.Lepeshev & S.M.Zharkovad. The Influence Of Oxygen Concentration On The Formation Of CuO And Cu2O Crystalline Phases During The Synthesis In The Plasma Of Low Pressure Arc Discharge. *Vacuum* **128**, 123-127, doi:https://doi.org/10.1016/j.vacuum.2016.03.025 (2016).

29 Cai, Y., Zhang, C. & Feng, Y. P. Dielectric properties and lattice dynamics of ?-PbO2-type TiO2: The role of soft phonon modes in pressure-induced phase transition to baddeleyite-type TiO2. *Phys. Rev. B* **84**, 94107, doi:https://doi.org/10.1103/PhysRevB.84.094107 (2011).

30 Sopicka-Lizer, M. High-Energy Ball Milling: Mechanochemical Processing of Nanopowders. *Elsevier* **Chapter 13**, 306, doi:ISBN: 9781845699444 (2010).

31 Saitow, K.-i. & Wakamiya, T. 130-fold enhancement of TiO2 photocatalytic activities by ball milling. *Appl. Phys. Lett.* **103**, 31916, doi:https://doi.org/10.1063/1.4816058 (2013).

32 Lee, J. H. & Yang, Y. S. Synthesis of TiO2 nanoparticles with pure brookite at low temperature by hydrolysis of TiCl4 using HNO3 solution. *Journal of Materials Science* **41**, 557-559, doi:https://doi.org/10.1007/s10853-005-2152-z (2006).

33 Paola, A. D. *et al.* Photocatalytic activity of nanocrystalline TiO2 (brookite, rutile and brookite-based) powders prepared by thermohydrolysis of TiCl4 in aqueous chloride solutions. *Colloids and Surfaces A: Physicochemical and Engineering Aspects* **317**, 366-376, doi:https://doi.org/10.1016/j.colsurfa.2007.11.005 (2007).

34 S.Mahshid, M.Askari & Ghamsari, M. S. Synthesis of TiO2 nanoparticles by hydrolysis and peptization of titanium isopropoxide solution. *Journal of Materials Processing Technology* **189**, 296-300, doi:https://doi.org/10.1016/j.jmatprotec.2007.01.040 (2007).

35 Qourzal, S., Assabbane, A. & Ait-Ichou, Y. Synthesis Of TiO2 Via Hydrolysis Of Titanium Tetraisopropoxide And Its Photocatalytic Activity On A Suspended Mixture With Activated Carbon In The Degradation Of 2-Naphthol. *Journal Of Photochemistry And Photobiology A: Chemistry* **163**, 317-321, doi:https://doi.org/10.1016/j.jphotochem.2003.12.013 (2004).

36 Xia, T. & Chen, X. Revealing the structural properties of hydrogenated black TiO2 nanocrystals. *J. Mater. Chem. A* **1**, 2983-29899, doi:10.1039/C3TA01589K (2013).

37 Liu, Y., Tian, L., Tan, X., Li, X. & Chen, X. Synthesis, properties, and applications of black titanium dioxide nanomaterials. *Science Bulletin* **62**, 431-441, doi:https://doi.org/10.1016/j.scib.2017.01.034 (2017).

38 Nakaso, K., Okuyama, K., Shimada, M. & E.Pratsinis, S. Effect of reaction temperature on CVD-made TiO2 primary particle diameter. *Chemical Engineering Science* **58**, 3327-3335, doi:https://doi.org/10.1016/S0009-2509(03)00213-6 (2003).

39 Wegner, K. & Pratsinis, S. E. Gas-Phase Synthesis Of Nanoparticles: Scale-Up And Design Of Flame Reactors. *Powder Technology* **150**, 117-122, doi:https://doi.org/10.1016/j.powtec.2004.11.022 (2005).

40 Zhang, Y., Li, S., Deng, S., Yao, Q. & D.Tse, S. Direct synthesis of nanostructured TiO2 films with controlled morphologies by stagnation swirl flames. *Journal of Aerosol Science* **44**, 71-82, doi:https://doi.org/10.1016/j.jaerosci.2011.10.001 (2012).

41 Zhao, H. Experimental And Computational Studies Of Flame Synthesis Of Nanoparticles: Effects Of Pressure, Precursor Loading, And Electric Field. *Rutgers University* (2007).

42 Smith, M. E. Residence-Time-Fixed Investigation Of Pressure And Temperature Effects On The Flame Synthesis Of Nanoparticles. *Rutgers University*, doi:https://dx.doi.org/doi:10.7282/T3M61KHW (2008).

43 Zhao, H., Liu, X. & D.Tse, S. Control of nanoparticle size and agglomeration through electric-field-enhanced flame synthesis. *Journal of Nanoparticle Research* **10**, 907-923, doi:https://doi.org/10.1007/s11051-007-9330-7 (2008).

44 Zhao, H., Liu, X. & D.Tse, S. Effects of pressure and precursor loading in the flame synthesis of titania nanoparticles. *Journal of Aerosol Science* **40**, 919-937, doi:https://doi.org/10.1016/j.jaerosci.2009.07.004 (2009).

45 Gabbott, P. Principles And Applications Of Thermal Analysis. *Blackwell Publishing Ltd*, 59, 484, doi:10.1002/9780470697702.fmatter (2008).

46 Hecht, E. Optics. *Addison-Wesley*, doi:ISBN: 9780805385663 (2002).

47 Goldstein, J. *et al.* Scanning Electron Microscopy And X-Ray Microanalysis. *Springer* doi:10.1007/978-1-4615-0215-9 (2003).

48 Williams, D. B. & Carter, C. B. Transmission Electron Microscopy. *Springer* doi:10.1007/978-0-387-76501-3 (2009).

49 Cullity, B. D. Elements Of X-Ray Diffraction. *Addison-Wesley Publishing Company*, doi:ISBN: 9780201011746 (1978).

50 Tipler, P. A. & Llewellyn, R. Modern Physics. *Macmillan*, doi:ISBN: 9780716743453 (2003).

51 Choi, H. C. *et al.* Characterization Of The Structures Of Size-Selected TiO2 Nanoparticles Using X-Ray Absorption Spectroscopy. *Applied Spectroscopy* **58**, 598-602, doi:https://doi.org/10.1366/000370204774103435 (2004).

52 Schlabach, S., Szabó, D. V. & Vollath, And D. Structure And Grain Growth Of TiO2 Nanoparticles Investigated By Electron And X-Ray Diffractions And Ta 181 Perturbed Angular Correlations. *Journal Of Applied Physics* **100**, 024305, doi:http://dx.doi.org/10.1063/1.2214182 (2006).

53 Chien-Iwu *et al.* Preparation Of TiO2 Nanoparticles By Supercritical Carbon Dioxide. *Materials Letters* **62**, 1923-1926, doi:https://doi.org/10.1016/j.matlet.2007.10.043 (2008).

54 Brown, S. C. *et al.* Nanoparticle Characterization For Cancer Nanotechnology And Other Biological Applications. *Humana Press* **624**, doi:https://doi.org/10.1007/978-1-60761-609-2_4 (2010).

55 Xue, X. *et al.* Raman Investigation of Nanosized TiO2: Effect of Crystallite Size and Quantum Confinement. *J. Phys. Chem. C* **116**, 8792–8797, doi:DOI: 10.1021/jp2122196 (2012).

56 Naumkin, A., Kraut-Vass, A., Gaarenstroom, S. & Powell, C. Nist X-Ray Photoelectron Spectroscopy Database, Version 4.1; National Institute Of Standards And Technology. *National Institute Of Standards And Technology* **7**, Version 4.1, doi:http://srdata.nist.gov/xps/ (2012).

57 E.L.Bullock, L.Patthey & S.G.Steinemann. Clean And Hydroxylated Rutile TiO2(110) Surfaces Studied By X-Ray Photoelectron Spectroscopy. *Surface Science* **352–354**, 504-510, doi:https://doi.org/10.1016/0039-6028(95)01188-9 (1996).

58 Chen, L.-C., Ho, Y.-C., Guo, W.-S., Huang, C.-M. & Pan, T.-C. Enhanced Visible Light-Induced Photoelectrocatalytic Degradation Of Phenol By Carbon Nanotube-Doped TiO2 Electrodes. *Electrochimica Acta* **54**, 3884-3891, doi:https://doi.org/10.1016/j.electacta.2009.02.001 (2009).

59 Sanderson, R. T. Chemical Bonds And Bond Energy. *Academic Press* (1971).

60 Sanderson, R. Polar Covalence. *Elsevier* (1983).

61 Sosa, R. M., Gardiol, P. & Beltrame, G. A Theoretical Study Of The Electronic Structure Of Transition-Element Carbides Mnc (M=Fe,?Ni,?Cu, N=1,?5; And M=Ti, N=1,?7) And Their Interactions With An O Atom By Dft Methods. *Int. J. Quantum Chem.* **65**, 919–928, doi:doi:10.1002/(SICI)1097-461X(1997)65:5<919::AID-QUA55>3.0.CO;2-Q (1997).